ALMA MATER STUDIORUM · UNIVERSITY OF BOLOGNA

School of Science
Department of Physics and Astronomy
Master Degree in Physics

DEVELOPMENT OF THE SHiP DOWNSTREAM MUON DETECTOR

Supervisor: Submitted by:

Prof. Tiziano Rovelli   Valentina Cicero

Co-supervisors:

Dr. Alessandro Montanari
Dr. Nicolò Tosi

Abstract

SHiP (Search for Hidden Particles) is a beam dump experiment proposed at CERN SPS, currently in the design stage. SHiP aims to observe long lived particles very weakly coupled with ordinary matter, as expected in a large number of Hidden Sector models, that are able do describe Dark matter, neutrino oscillation and the origins of the Barionic Asimmetry of universe.

In this thesis the development of the SHiP Downstream Muon Detector is described. This subdetector aims to identify with high efficiency muons produced by signal processes and to distinguish them from neutrino- and beam-induced background ones. In order to effectively distinguish background events mistakenly reconstructed as signal vertexes due to their spatial overlapping, a time resolution better than 200 ps is mandatory. Therefore, it is extremely important that the detector components are optimized with respect to time resolution.

The detector employs active layers made of plastic scintillator tiles, each coupled to silicon photomultipliers (SiPM). This thesis focuses on the development of tile prototypes that are able to meet the detector time resolution requirements, through the study of various aspects of the tile design. The improved design defined with the contribution of this thesis work has become the current baseline design and will be tested with a prototype in early 2020 at the Frascati INFN Laboratories.

Abstract (Italiano)

L'esperimento SHiP (Search for Hidden Particles) è un esperimento di beam dump proposto all'SPS del CERN, al momento in fase di progettazione. L'obiettivo di SHiP consiste nell'osservazione di particelle a lunga vita media accoppiate molto debolmente con la materia ordinaria, come previsto da un grande numero di modelli di Hidden Sector capaci di descrivere la materia oscura, le oscillazioni dei neutrini e le origini dell'asimmetria barionica nell'Universo.

In questa tesi è descritto il lavoro svolto sullo sviluppo del rivelatore di muoni di SHiP, il cui scopo è principalmente quello di identificare con alta efficienza i muoni provenienti da canali di decadimento di nuova fisica e di separarli da processi di background indotti da neutrini e dal fascio. Per discriminare efficacemente gli eventi di background ricostruiti erroneamente come vertici di segnale per via della loro sovrapposizione spaziale, è necessario che la risoluzione temporale del detector sia inferiore ai 200 ps. Risulta quindi di estrema importanza l'ottimizzazione delle componenti del rivelatore in funzione della risoluzione temporale.

Il rivelatore impiega stazioni attive composte da tiles di scintillatore plastico, ciascuna accoppiata a fotomoltiplicatori al silicio (SiPM). Questo lavoro di tesi si concentra sullo sviluppo di prototipi di tiles che soddisfino i requisiti di risoluzione temporale del rivelatore, per mezzo dello studio di diversi aspetti della tile.

Il design definito con il lavoro di questa tesi è diventato l'attuale soluzione di riferimento e sarà testato a inizio 2020 presso i Laboratori Nazionali di Frascati.

Contents

Introduction

SHiP is an experiment aimed at exploring the domain of very weakly interacting particles. It is designed to be installed downstream of a new high-intensity beam-dump facility at the Super Proton Synchrotron at CERN.

We have now observed all the particles of the Standard Model (except for the $\overline{\nu}_\tau$), however it is becoming clear that it cannot be the ultimate theory. Some yet unknown particles or interactions are required to explain a number of observed phenomena in particle physics, astrophysics and cosmology, such as dark matter, neutrino masses and oscillations, baryon asymmetry, and the expansion of the universe. While these phenomena are well-established observationally, they only give weak indications about the energy scale of the new physics. It is plausible that the shortcomings of the Standard Model may have their origin in new physics only involving very weakly interacting, relatively light particles. Experimentally, the opportunity presents itself as an exploration at the intensity frontier with the largest possible luminosity to overcome the very feeble interactions, and the largest possible acceptance to account for the typically long lifetimes. Beam-dump experiments are potentially superior to collider experiments in the sensitivity to GeV-scale hidden particles with their luminosities being several orders of magnitude larger than at colliders.

The SHiP experiment is composed of several subdetectors, of which the most downstream is dedicated to the identification of muons. The muon detector will cover an area of 72 m^2 and will be equipped with 4 planes of scintillator interposed with iron absorbers. One of the main contributions to background in the experiment is given by uncorrelated muon tracks forming a fake vertex in the fiducial volume. This "combinatorial" background can be reduced by requiring the particles that form a vertex to be on time within a very short time window, and this drives the requirement of the detector time resolution. In order to cover such a large area with a fast and robust detector, a system based on $\sim$200 cm^2 squared scintillator tiles, read out at the corners by silicon photomultipliers (SiPMs), has been developed. Through the optimization of the SiPM characteristics, placement and mounting technique on the tile, as well as coating type of the scintillator, we aim at achieving a time resolution lower than 400 ps on a tile of such size.

The work is organized as follows: the first chapter describes the theoretical background and the main physics goals of of the SHiP experiment. The second chapter is an overview of the experiment: the basic structure of the apparatus is explained, describing the target and the two main detectors, the first aimed at observing the interactions of neutrinos and dark matter, the other designed to detect the products of hidden particle decays. Chapter 3 is entirely dedicated to the description of the SHiP Downstream Muon Detector. In the fourth chapter I describe in detail the working principles of the Muon Detector basic elements: a tile made of plastic scintillator read out by silicon photomultipliers. Finally, Chapters 5 and 6 are dedicated to the testing of the prototype tiles built between 2018 and 2019 in order to develop a definitive design of the scintillator tile. In chapter 5, I examined the data collected in 2018 with the available prototypes, and used it investigate the most suitable algorithms to extract timing information from the tile output. The results obtained on the tiles timing performance led us to build an improved prototype. I characterized the silicon photomultipliers to be installed and analyzed the data of the beam test performed in 2019. The analysis for determining the time resolution of the prototypes is described in chapter 6, with the comparison with simulations as well. Moreover, I explored an alternative method to mount silicon photomultipliers to the scintillator that is mechanically more convenient by comparing the light collection of the two methods.

The analyses carried out in this thesis will define a new tile design that will be tested in early 2020.

Chapter 1

Physics background

1.1 Theories beyond the Standard Model

As of 2012, with the discovery of the Higgs Boson, all predicted constituents of the Standard Model (SM) have been observed. At the same time, no significant deviations from the SM were found in direct or in indirect searches for new physics. For a value of the Higgs mass of $\simeq 125$ GeV, the SM may remain mathematically consistent and valid as an effective field theory up to a very high energy scale, possibly to the scale of quantum gravity, the Planck scale. However, the Standard Model cannot be considered a complete description of Nature, since it does not explain some experimental evidences. The most relevant are the following:

1. **Neutrino oscillations** show that neutrinos have mass different from zero, but how they acquire mass is still unknown. If they behave like the other elementary fermions, they should acquire mass through the Yukawa coupling to the Higgs field, however, this is not possible as a right-handed neutrino is needed, not foreseen in the original version of the SM. The introduction of a right-handed field ν_R would allow to form a Dirac mass term generated by coupling to the Higgs field, as it occurs for quarks and charged leptons, through the so-called see-saw mechanism [1]. In the Neutrino Minimal Standard Model (νMSM), the right handed neutrinos can have masses also below the EW scale and extremely feeble couplings [1];

2. it was estimated that ordinary matter accounts for only 5% of the total composition of the Universe. The remaining consists of $\sim 68\%$ **Dark Energy** and $\sim 27\%$ of **Dark matter**. Dark matter does not interact with the electromagnetic force, but it has a gravitational effect that has brought to its discovery. Dark Energy seems to be related to the vacuum in space: it does not have any local gravitational effects,

but a global effect on the Universe as a whole, thus influencing the expansion rate of the Universe itself;

3. the **Baryon Asymmetry of the Universe** (BAU) consists in the excess of matter over anti-matter in the Universe. The existence of matter itself is the indirect proof that there must have been a slight matter-antimatter imbalance in the early Universe, of the order of one particle per billion. The SM cannot explain this imbalance, as the observed CP violation, which occurs through the CKM mass matrix, is too small ($\varepsilon_{CP} \sim 10^{-20}$) to account for the observed value of the baryon asymmetry ($\eta_B = \frac{n_B - n_{\overline{B}}}{n_\gamma} \equiv 10^{-10}$, n_B, $n_{\overline{B}}$ being respectively the baryon and anti-barion density and n_γ the photon density).

There is also no consensus on a mechanism to account for cosmic inflation. There is a list of aspects that need to be investigated to produce an extension of the SM that includes them, but no clear guidance on the scale of any new physics, or the coupling strength of any new particles to the SM ones. This lack of theoretical guidance needs experimental searches at both the *"energy"* and *"intensity frontiers"*. One possibility is that the hypothetical particles are heavy and require even higher collision energy to be observed. Major particle physics experiments of the last few decades, including LEP and LHC at CERN, and Tevatron in the US have pursued this path. Another possibility is that our inability to observe new particles lies not in their heavy mass, but rather in their extremely feeble interactions with the SM particles, which make them *dark* or *hidden*. If true, this would imply that to detect them we should maximise the number of interactions, instead of the center-of-mass energy. This latter choice is the main motivation for beam dump experiments, which belong to the intensity frontier category. A scheme of a typical beam dump experiment is shown in Fig. 1.1: a beam of high energy protons impinges onto a dense target (beam dump), which absorbs it giving rise to a lot of interactions and final state particles. The high number of interactions allows the production of light new particles, even considering their feeble couplings to Standard Model particles. The new particles are let to decay in a long vacuum volume, called the decay volume, at its end the charged particles produced are identified in a detector and their characteristics are measured. As well as the hidden particles, SM particles are also produced in the dump; rejection of those particles is essential to suppress backgrounds. In particular, a significant amount of muons are produced. Thus, it is necessary to install shields and veto counters between the dump and the decay volume. Additional veto counters surrounding the detector serve to reject background events coming from outside the detector.

Some of the new particles can be heavy or do not interact directly with the SM sector. These "hidden sectors" may be accessible nevertheless to the intensity fron-
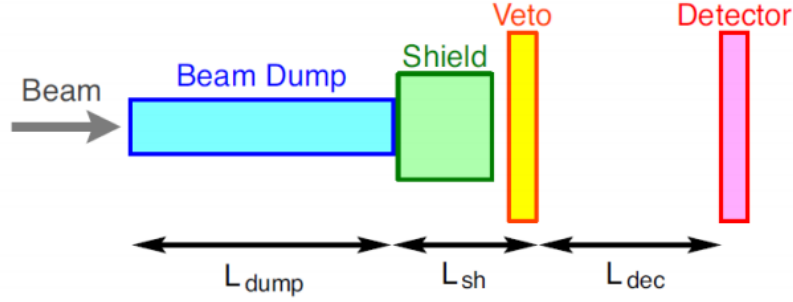
Figure 1.1: Schematic design of a typical beam dump experiment.

tier experiments via sufficiently light particles, which are coupled to the SM sectors either via renormalizable interactions with small dimensionless coupling constant (called "portals") or by higher-dimensional operators suppressed by the dimensionful couplings, corresponding to a new energy scale of the hidden sector. For the Standard Model, renormalizable portals can be classified into the following three types, depending on the mass dimension of the SM singlet operator.

1. *Vector portal*: the singlet operator has the dimension of a mass squared (GeV^2). The new particles are Abelian fields which couple to the hypercharge field $F_Y^{\mu\nu}$ via a dimensionless coupling, characterizing the mixing between the new vector field with the Z-boson and the photon;

2. *Scalar portal*: the new particles are neutral singlet scalars that couple to the square of the Higgs field;

3. *Neutrino portal*: new neutral singlet fermions N_i are introduced, which couple with singlet operators with dimension $GeV^{\frac{5}{2}}$

The phenomenology of these portals and other possible models will be discussed in more detail in the following sections.

1.1.1 Vector portal

The gauge structure of the Standard Model, the $SU(3) \times SU(2) \times U(1)$ combination, can be derived from a larger gauge group, as is the case in Grand Unified Theories (GUTs). In that case, one expects that at least several of the new vector states are very heavy, well beyond the direct reach of accelerators. However, if additional gauge structures accompany the SM, as is the case of multiple U(1)s, $SU(3) \times SU(2) \times [U(1)]^n$, sub-TeV

gauge bosons are also allowed.

The LHC set robust bounds on these new vector states [2]. An alternative possibility, relatively light vector states (e.g., in the GeV mass range) with small couplings to the SM, is instead poorly constrained by the LHC experiments and represents an attractive physics target for many experiments at the intensity frontier.

The simplest way to couple a new vector particle to the SM is to use the kinetically-mixed portal. In this case, none of the SM fields needs to be charged under the new gauge groups. Minimalistic models consider a U(1) gauge symmetry in the hidden sector with an associated gauge boson A', called *dark photon*.

If a new Higgs field is present in the dark sector (dark Higgs), then the U(1) gauge symmetry might be broken by a Higgs-like mechanism and the dark photon acquires a non-zero mass.

The vector portals are of great interest because they might help to solve known problems of the SM. Light mass vector particles might provide a solution to the muon g-2 discrepancy [3] through a slightly extended model of the dark photon [4]. Light mass vector particles can also be thought of as mediators of the interaction with DM and provide an explanation to the astrophysical positron excess [5].

In a beam dump experiment, dark photons can be originated via:

1. *Meson decays*: mesons are copiously produced in proton on target collisions. The most important process is $\pi^0 \longrightarrow \gamma A$, which is suppressed by ε^2, the $\ll 1$ mixing parameter between the dark photon and the SM one, but not by α, since the π^0 decay is an electromagnetic process;

2. *Proton bremsstrahlung*: the (quasi)elastic scattering of incident protons on nucleons in the target can lead to the production of vector states via bremsstrahlung process $pp \longrightarrow ppA$;

3. *Direct perturbative QCD production*: processes like $q + \bar{q} \longrightarrow A$ and $q + g \longrightarrow q + A$ become dominant for larger masses of the vector particles.

The decay modes and branching ratios of dark photons are shown in Fig. 1.2 in relation to the potential dark photon mass.

1.1.2   Scalar portal

Many extensions of the SM Higgs sector foresee additional light scalar or pseudoscalar particles that are singlets under the SM gauge group and have highly suppressed couplings to SM particles. Alternatively, such particles can arise as pseudo-Nambu-Goldstone bosons (PNGB) of a spontaneously broken symmetry [7].
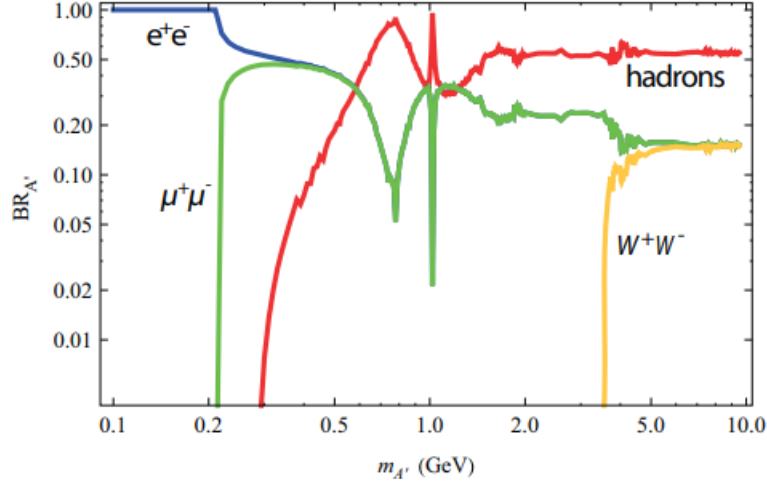
Figure 1.2: Predicted dark photons decay modes and their branching fractions for different dark photon mass values. [6]

There are already stringent experimental constraints on the mass of hidden scalars and their coupling g^* to SM particles. Nevertheless, the SHiP experiment will give new insights especially for the mass region below 10 GeV, that is as of today still unexplored. This model is build from the SM Lagrangian with the addition of a (CP-even) singlet scalar field:

$$\mathcal{L} = \mathcal{L}_{SM} + \frac{1}{2}\partial_\mu S \partial^\mu S + (\alpha_1 S + \alpha S^2)(H^\dagger H) + \lambda_2 S^3 + \lambda_3 S^3 + \lambda_4 S^4 \qquad (1.1)$$

where $\lambda_{1,2,3}$ are the scalar self couplings while α_1 and α represent the portal couplings to the SM Higgs doublet H.

For a hidden sector made of scalar fields, the portal operators appearing in Eq. (1.1) are renormalizable, meaning that if the interactions between the extra scalar and the Higgs boson are generated at very high scales such as the GUT, or even Planck scale, then they may remain as a relevant interaction down to the energy scales probed by experiments today. Moreover, since dark matter is believed to be neutral under all SM gauge interactions, and the Higgs portal can provide a bridge between the SM and neutral sectors, it is possible that scalars coupled through the Higgs portal may play a role in dark sector physics, or perhaps themselves be DM candidates.

For a light scalar with a mass well below the Higgs mass ($m_S \ll m_h$) and in the limit of

a small α_1 coupling, the mixing angle is given by [2]:

$$g_* = \sin\theta \equiv \theta \equiv \frac{\alpha_1 v^2}{m_h^2} \tag{1.2}$$

where $v = 246$ GeV denotes the electroweak vacuum expectation value (VEV). In this case, both the production mechanisms and decay modes coincide with those of a SM Higgs boson having the same mass of the considered light scalar. However, with respect to the Higgs boson, the production cross sections and the decay rates are suppressed by a factor g_*^2. Figure 1.3 shows the decay branching ratios as a function of the scalar mass m_S, the gap around 2 GeV is due to the appearance of a large number of hadronic resonances.
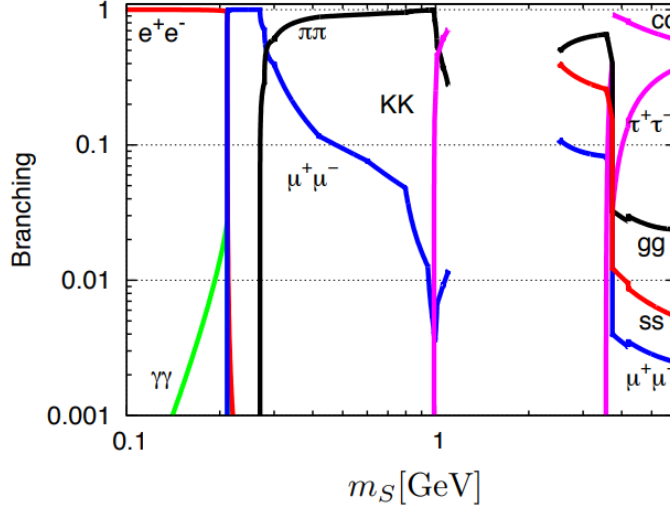

Figure 1.3: Decay branching ratios function of the scalar mass m_s

1.1.3   Neutrino portal

The Neutrino Minimal Standard model (νMSM) [8, 9] is a minimalistic model that solves the SM puzzles by inserting three heavy right-handed neutrinos that couple to the left-handed SM neutrinos (see Fig. 1.4). These heavy neutrinos are sterile, i.e. they do not couple, apart from gravity, to any of the fundamental SM interactions, and are also referred to as Heavy Neutral Leptons (HNLs).

HNLs are singlets with respect to the $SU(2) \times U(1)$ group and they couple to the Higgs boson.
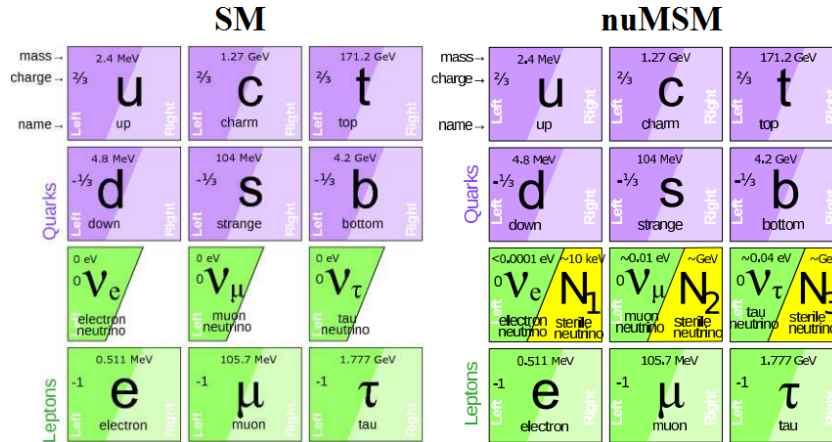
Figure 1.4: In the Standard Model neutrinos are massless and always left-chiral. The right-chiral counterparts N_1, N_2, N_3 are added. They do not feel the electric, weak or strong forces (thus sterile neutrinos).

The lightest of the HNLs, N_1, is extimated to have a mass of a few keV [8], and it is a DM candidate with a lifetime bigger than the lifetime of the Universe. It can decay either in three neutrinos (invisible) or in a photon and a neutrino ($N_1 \longrightarrow \nu\gamma$). On the other hand, N_2 and N_3 are degenerate in mass, in the MeV-GeV range. They can explain the baryon asymmetry through a process of leptogenesis made possible by their lepton number violating Majorana mass term. Furthermore, they can explain the observed pattern of neutrino masses through the type I see-saw mechanism [9].
HNLs can be produced in association with a charged lepton in 2-body meson decays, and in 3-body meson decays into HNL, light (pseudoscalar or vector) meson and a charged lepton [2]. A possible HNL production mechanisms is shown in the left panel of Fig. 1.5.

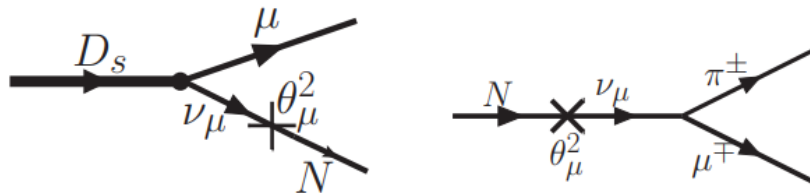

Figure 1.5: Production (left) and subsequent decay (right) of the particle N_I

It is exactly their mixing with active neutrinos through the Higgs boson that makes them unstable. They decay emitting a charged lepton and a vector boson (W or Z)

giving rise to final states containing either another charged lepton or hadrons:

$$N_i \longrightarrow e^+e^-\nu, \mu^+\mu^-\nu, \mu^{\pm}e^{\mp}\nu, \tau^+\tau^-\nu, \text{etc.} \tag{1.3}$$

$$N_i \longrightarrow \pi^{\pm}e^{\mp}, \pi^{\mp}\mu^{\mp}, K^{\pm}e^{\mp}, K^{\pm}\pi^{\mp}, \text{etc.} \tag{1.4}$$

A potential two-body decay mode of $N_{2,3}$ is shown in the right panel of fig. 1.5.

1.1.4 Axion-Like particles

While the new particles hypothesized by the models described in the previous sections are coupled to the SM via renormalizable interactions with small dimensionless coupling constants, Axion Like Particles (ALPs) would couple via a higher-dimensional operator [2].
ALPs are Pseudo-Nambu-Goldstone bosons (PNGBs) that come from spontaneously broken global symmetries. They exhibit two fundamental properties: they have small couplings, as their interactions are suppressed by the scale of spontaneous symmetry breaking f_A, and have a small mass, since a small explicit breaking of the symmetry at a scale Λ leads their mass to be suppressed by the scale of spontaneous symmetry breaking, i.e. $m_A \simeq \Lambda^2/f_A$.
An example of a very light PNGB is the axion, that was introduced to solve the strong CP problem in QCD. The axion mass is strongly constrained by theory. However, there are other possible particles that, even if they undergo very similar interactions with respect to the axion, they can have different masses. These particles are usually denoted as Axion-Like Particles. According to the models, each process that produces pions has a non-null probability of producing an axion. Particularly interesting channels to look for an axion decay are $A \longrightarrow \gamma\gamma$, to investigate for couplings with gauge bosons, and $A \longrightarrow \mu^+\mu$, to explore couplings with SM fermions.

1.1.5 SUSY

Supersymmetry (SUSY) is one of the most motivated extensions of the SM where bosons and fermions are connected. The minimal supersymmetric model considering only the minimum number of new particle states and new interactions consistent with phenomenology is the Minimal Supersymmetric Standard Model (MSSM) [10].
A supersymmetric transformation changes a bosonic state in a fermionic one and vice-versa: each fermion has a bosonic partner with the same quantum numbers but with a spin which differs by half a unit. Therefore, in the MSSM there are both vector superfields associated with the Standard Model gauge groups which contain the vector bosons

and associated gaugino and chiral superfields for the SM fermions and Higgs bosons with their respective superpartners.

If the supersymmetry were an exact symmetry, all the particles belonging to the same supermultiplet should have the same mass. Hence, we should have been able to observe an s-electron with the same mass of an electron, a squark u with the same mass of the quark u and so on. Since any of these observations have not been done yet, the supersymmetry must be a broken symmetry.

The most general supersymmetric Lagrangian contains terms violating both the barion and the lepton number, thus being in contrast with the nonobservation of proton decays. To explain the stability of the proton, the MSSM imposes a new discrete symmetry named R-parity, which associates to a particle or its supersymmetric partner with spin s the quantic number $R = (1)^{3(BL)+2s}$ [10]. R-parity is a multiplicative quantic number which is also assumed to be conserved in the physical processes.

Searches for Supersymmetry are now spanning the mass region of 100 GeV - 10 TeV and are currently ongoing at LHC. However, the possibility that SUSY particles have a mass which is a couple of orders of magnitude lighter than the mass of the W and Z bosons has not yet been excluded neither from LHC searches nor from precision fits of the SM. There are indeed many supersymmetric models that still allow for new light neutral particles to be in the MeV to a few GeV range that can be looked for at a beam dump experiment. For example, even though a stable neutralino in the mass range between 0.7 eV and 24 GeV is excluded because it gives too much DM, if the possibility of the R-parity to be violated is introduced then it becomes allowed. Not having a convincing theory of supersymmetry breaking leaves a lot of space for experiments to investigate.

1.2 τ Neutrino Physics

In a fixed target facility, with a high intensity and high energy proton beam impinging on a target, a high flux of neutrinos of all flavours can be expected. Therefore, it is ideally suited to perform studies on neutrino and antineutrino physics [7].

First direct measurements of tau neutrino charged current interactions are very recent, and no $\overline{\nu}_\tau$ interaction has been directly observed yet.

Search for ν_τ and $\overline{\nu}_\tau$ interactions shall lead to new measurements of the neutrino and antineutrino charged current cross sections. In a deep inelastic events' analysis, the tau neutrino and antineutrino cross sections, in terms of the structure functions(F1 F5), can be written as:

$$\frac{d^2\sigma^{\nu(\overline{\nu})}}{dxdy} = \frac{G_F^2 M E_\nu}{\pi(Q^2/M_W^2)^2}\left((y^2x + \frac{m_\tau^2 y}{2E_\nu M})F_1 + \left[(1 - \frac{m_\tau^2}{4E_\nu^2} - (1 + \frac{M_X}{2E_\nu})yF_2]\right.\right.$$
$$\left.\left.\pm [xy(1 - \frac{y}{2}) - \frac{m_\tau^2 y}{4E_\nu M}]F_3 + \frac{m_\tau^2(m_\tau^2 + Q^2)}{4E_\nu^2 M_X^2}F_4 - \frac{m_\tau^2}{E_\nu M}F_5\right) \quad (1.5)$$

where the plus sign applies to neutrino scattering and the minus one to antineutrino scattering. M and m_τ are the nucleon and τ lepton masses, respectively, M_W is the W boson mass, E_ν is the initial neutrino energy and G_F is the Fermi constant. The structure functions F_4 and F_5, negligible in electron and muon neutrino interactions due to the factor $m_l^2/(E_\nu M)$, are relevant in ν_τ scattering and therefore can be measured only with ν_τ interactions. In figure 1.6, the expected cross sections for CC neutrino and antineutrino interactions are shown, assuming for F4 and F5 the values given by the SM, compared with the hypothesis $F_4 = F_5 = 0$ [11]. Neglecting both structure functions leads to an increase of the cross sections and, consequently, to a larger number of expected ν_τ and $\overline{\nu}_\tau$ interactions. The difference between the two hypotheses is greater at low energies and tends to zero beyond hundreds of GeVs, where the contribution of F_4 and F_5 becomes negligible.
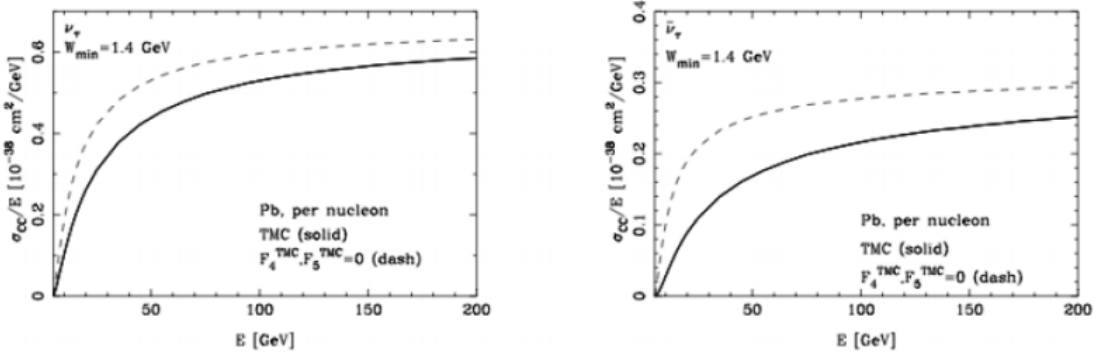

Figure 1.6: Prediction of the Standard Model (shown as a solid curve) and in the $F_4 = F_5 = 0$ hypotheses (shown as a dashed curve) for ν_τ (on the left) and $\overline{\nu}_\tau$ (on the right) CC deep inelastic scattering cross section.

Chapter 2

The SHiP Experiment

2.1 Overview

SHiP (Search for Hidden Particles) is a proposed beam dump experiment, whose primary goal is to explore hidden sector and tau neutrino physics [11]. 400 GeV protons, extracted from the Super Proton Synchrotron (SPS) accelerator, will impinge on a target made of molybdenum and tungsten. The SHiP detector, immediately downstream of the target, (Fig. 2.1) incorporates two complementary apparatuses, the Scattering and Neutrino Detector (SND), and the Decay Spectrometer: the first designed for the detection of neutrino interactions and light dark matter scattering off electrons and the second is optimized to detect the decay products of new particles.
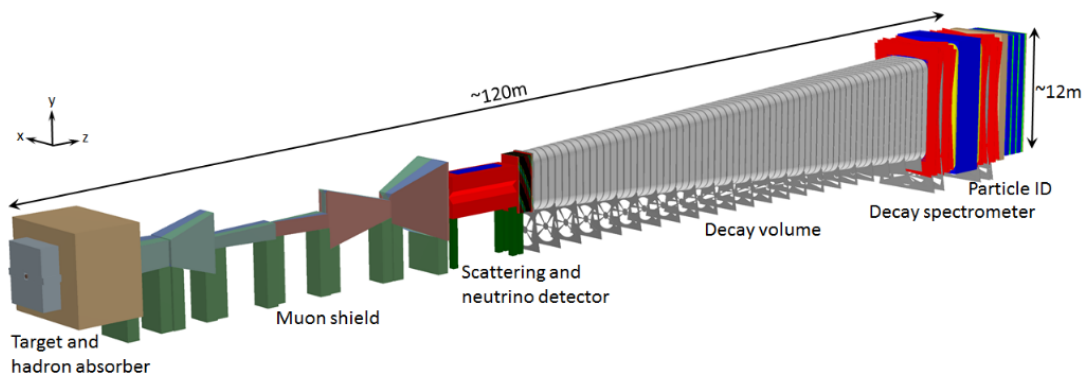

Figure 2.1: Overview of the SHiP experiment. [12]

Proton interactions in the target give rise to a copious direct production of Standard Model particles, which form the background that must be suppressed. A hadron stopper

13

of approximately five meters of iron is enough to absorb the hadronic and electromagnetic showers emerging from the target, but it cannot stop a large flux of muons and neutrinos, produced by the decays of pions and kaons. The reduction of the muon background is the task of a dedicated 35 m long muon shield, based on the magnetic deflection of these charged particles in the horizontal plane.

The SND detector is inspired by the concept of the OPERA apparatus, which employs the Emulsion Cloud Chamber technology [11]. It will be able to detect the interactions with micrometric accuracy, measure the neutrino flavor and discriminate between neutrinos and antineutrinos.

The Decay Spectrometer is placed downstream of a 50 m long decay volume, whose length has been chosen in order to maximize the acceptance to the hidden particle decays products. This volume must be under vacuum, in order to minimize the background from the residual neutrino flux. The most downstream section of the apparatus is devoted to the detection of the hidden particle decay products, through a magnetic spectrometer to measure the particles momentum and charge and a calorimeter and muon detector for energy measurement and particle identification.

In this chapter, we shall give an overview of the main components of the SHiP apparatus, describing their basic structure and functionality. Chapter 4 is entirely dedicated to the design of the Downstream Muon Detector, whose development is the subject of this thesis.

2.2   CERN Beam Dump Facility

The SPS is a particle accelerator at CERN. With a 7 km circumference, it is the second-largest machine in the CERN accelerator complex. Today, it is used as the final injector for high-intensity proton beams for the Large Hadron Collider (LHC), but it also provides proton beams for different fixed-target experiments, such as COMPASS, NA61/SHINE and NA62. SHiP is designed to use protons of the SPS impinging on a thick target (beam dump). The project foresees the construction of the SHiP facility at the CERN Prevessin Site, on the North Area of the SPS accelerator complex, in a geographical location that allows a full integration on the CERN land with minor impact on the existing facilities. The proton beam is acted via the TT20 transfer line, shared with the other North area facilities. In Fig. 2.2, the proposed location of the SHiP facility at the CERN Prevessin site is shown in a schematic drawing.
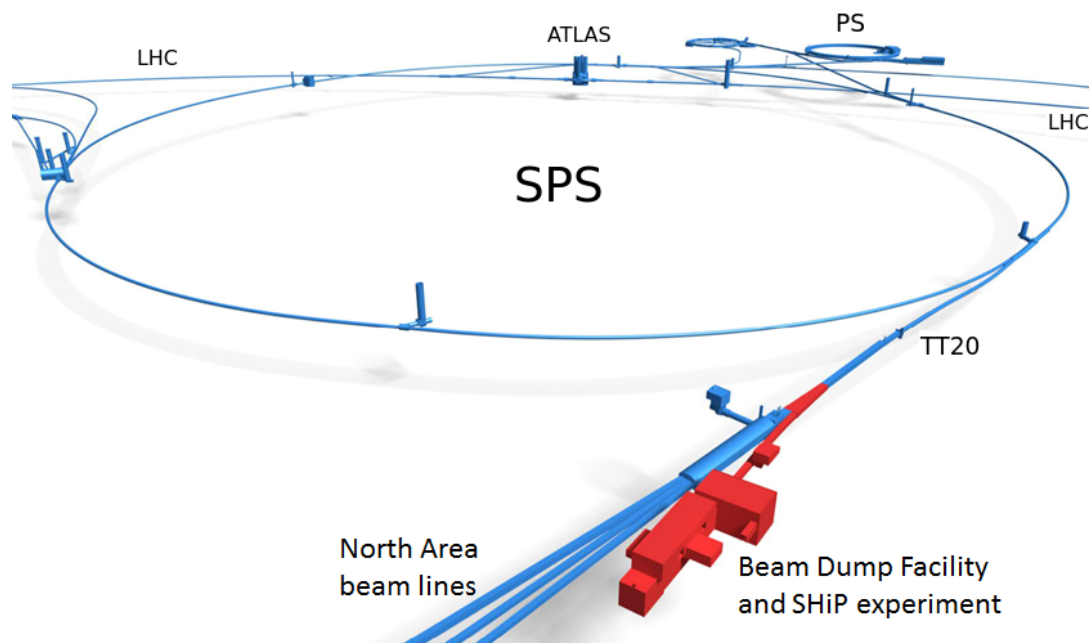
Figure 2.2: SHiP facility location in the North Area at the SPS accelerator complex.

2.2.1 Proton beam

For the SHiP physics program, a 400 GeV/c proton beam is required to be delivered on the SHiP target [2]. Being the weakly coupled particles, foreseen in different models beyond the Standard Model, mainly produced in the decay of charmed hadrons, the choice of 400 GeV energy protons fits the requirement of a high charm production cross-section. The physics sensitivity of the experiment is based on acquiring a total of $2 \cdot 10^{20}$ protons on target. The operational mode consists of continuous 24-hour data taking throughout the operational year with the exception of maintenance during technical stops.

The procedure used to transfer high energy particles from the SPS circular accelerator to the TT20 linear beamline is done first with a set of extraction sextupoles that cause the particles in the beam to move from the stable area in the phase space to an unstable, but controlled, one, away from the beam core. An electrostatic septum then catches the most unstable protons and deflects them toward the extraction line. Once the majority of the protons have been consumed, a new beam is injected and accelerated. The particle beam extracted is usually referred to as a spill. Each spill is assumed to have a beam intensity of 4×10^{13} protons on target, spread out over 1 s.

A new dedicated SHiP beam line branches off at the top of the TT20 transfer line, to the TDC2 cavern, with the help of a set of newly proposed magnet splitters which will replace the current one. The SHiP beam line is 120 m long and entirely in the horizontal plane. Bending magnets and a set of quadrupoles are used to minimize dispersion and to suppress motion induced by momentum variations during extraction.

2.2.2 Target

The SHiP production target is one of the most challenging aspects of the facility due to the very high average beam power (up to 350 kW) deposited on the target [11]. Integrating only over the spill duration, the expected beam power is 2.56 MW.
The choice of materials must take into account not only the high energy deposited and the high temperatures reached, but also the physics that is performed at SHiP. To search for Hidden Particles mainly coming from heavy mesons, their production must be maximized, while the fraction of neutrinos and muons coming from pion/kaon decays must be reduced as much as possible. These requirements lead to the choice of a high A material and with the shortest possible nuclear interaction length for pion and kaon reabsorption from spallation [13]. While a Tungsten target would be an optimal candidate that satisfies these material requirements, it cannot sustain the high temperatures reached during the steady state of operations.
The required performance is achieved with a longitudinally segmented hybrid target consisting of blocks of five interaction lengths of titanium-zirconium doped molybdenum (TZM) alloy in the core of the shower followed by seven interaction lengths of pure tungsten. The blocks are interleaved with slits of 5 mm thickness for water cooling. In order to respect the material limits on the thermomechanical stresses, the thickness of each slab together with the location of each cooling slit has been optimized to provide a uniform energy deposition and to guarantee sufficient energy extraction. Figure 2.3 shows the target design. The target shape is cylindrical, with a diameter of 25 cm and a length of 1.5 m, to maximize the shower containment.

The target is embedded in a massive cast iron bunker (440 m^3), with an inner core consisting of water-cooled cast iron blocks with embedded stainless steel water cooling pipes. The downstream proximity shielding which has a thickness of 5 m also acts as a hadron stopper. The hadron stopper has the double objective of absorbing the secondary hadrons and the residual non-interacting protons emerging from the target, and to significantly reduce the exposure of the downstream experiment muon shield to radiation. Moreover, the iron of the hadron stopper has been magnetised over a length of 4 m with the help of a magnetic coil integrated into the shielding [14]. The applied
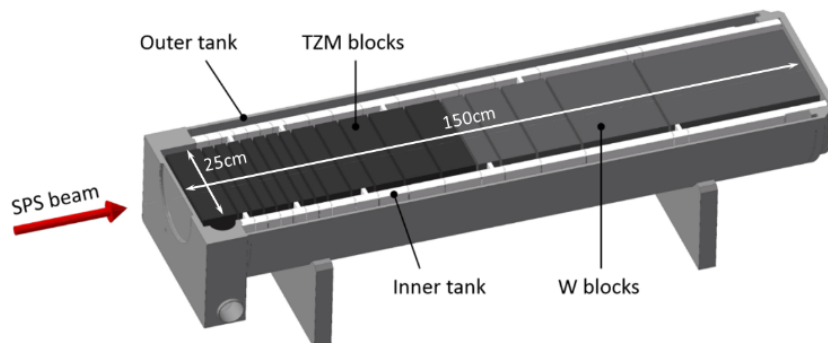
Figure 2.3: Target configuration.

dipole field makes up the first section of the muon shield, which is illustrated in the next section.

2.2.3   Muon shield

The protons that impinge on the target produce about $5 \cdot 10^9$ muons/spill [14]. These muons represent the main source of background to the detection of rare events, hence their flux has to be reduced by several orders of magnitude over the shortest possible distance, so that the transverse size of detector can be smaller to cover a given solid angle. To clear a 5 m horizontally wide region, a 35 m long active muon shield based on magnetic deflection of the muons in the horizontal plane is introduced right after the hadron stopper [12]. The design of the muon shield is shown in 2.4.

The first section, that is the 4 m long dipole field inside the hadron stopper, is used to separate μ^+ and μ^- on opposite sides, regardless of their initial direction. A two-dimensional scheme with the magnets behaviour is shown in Fig. 2.5. The field orientations are shown by the two colours: the regular field is depicted in light blue, while the return field is green. In the second section of the muon shield, the field polarization is reversed, with the return field closer to the z axis and the regular field at larger x. Muons bent out by the first part of the shield are then bent further outward, rather than back towards detector, as it would happen if a single long sequence of magnets were used. The peculiar shape of the final part of the shield allows to bend out also those particles which have not been deflected in the first part of the shield.
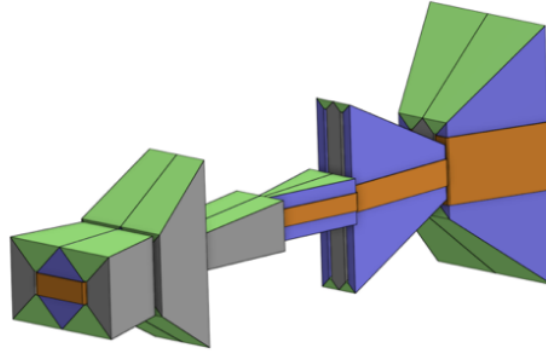
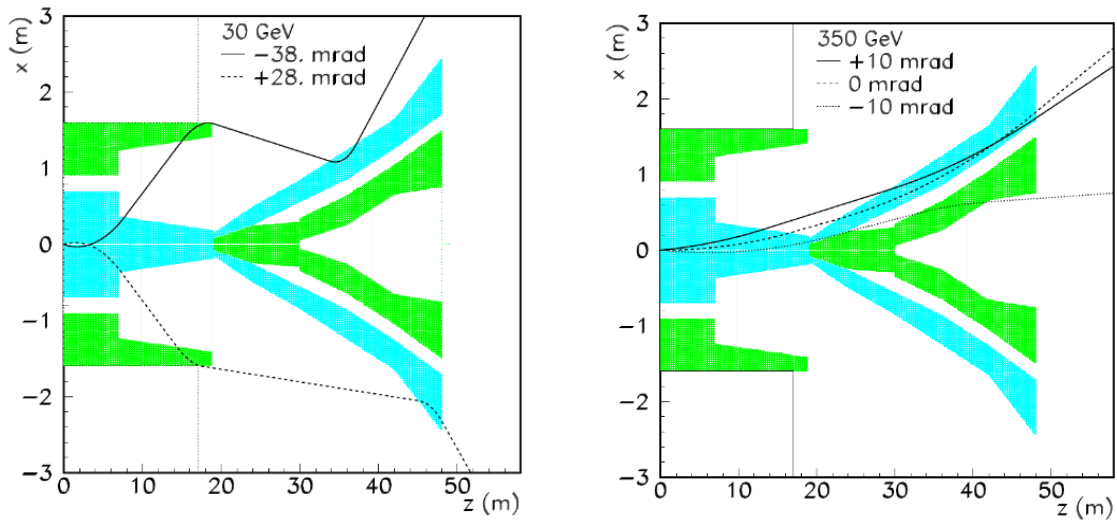Figure 2.4: Three dimensional view of the active shield.

Figure 2.5: Horizontal view of the proposed active muon shield showing the trajectory of three 30 Gev (left) and 350 GeV (right) muons with a range of initial angles. The light blue and green show the regions of regular and return field respectively [11]

2.3   Scattering and Neutrino Detector

The detector of neutrino and dark matter interactions, whose layout is shown in Figure 2.6, is placed downstream of the muon shield. A 7 m long magnet, providing a 1.2 T horizontal magnetic field, hosts the Emulsion Target interleaved with Target Tracker planes, and a Downstream Tracker [14].
The Emulsion Target has a modular structure: the unit cell consists of an Emulsion Cloud

Chamber (ECC) made of lead plates interleaved with nuclear emulsion films, followed by a Compact Emulsion Spectrometer (CES) for the momentum and charge measurement of particles produced in neutrino interactions. The ECC bricks are arranged in walls alternated with Target Tracker planes, based on scintillating fibers technology, which provide the time stamp of the interactions occurring in the target.

The Downstream Tracker is made of three Target Tracker planes separated by 50 cm air gaps. It is used to measure the charge and momentum of muons exiting the target region, thus extending significantly the detectable momentum range of the CES. The Downstream Tracker planes also help to connect the tracks in the emulsion films with the downstream muon identification system.

The muon identification system is made of a sequence of iron filters and RPC planes, totalling about two metres in length. The system also has the role of tagging neutrino interactions in its material which could lead to long-lived neutral particles entering the downstream HS decay volume and mimicking signal events.
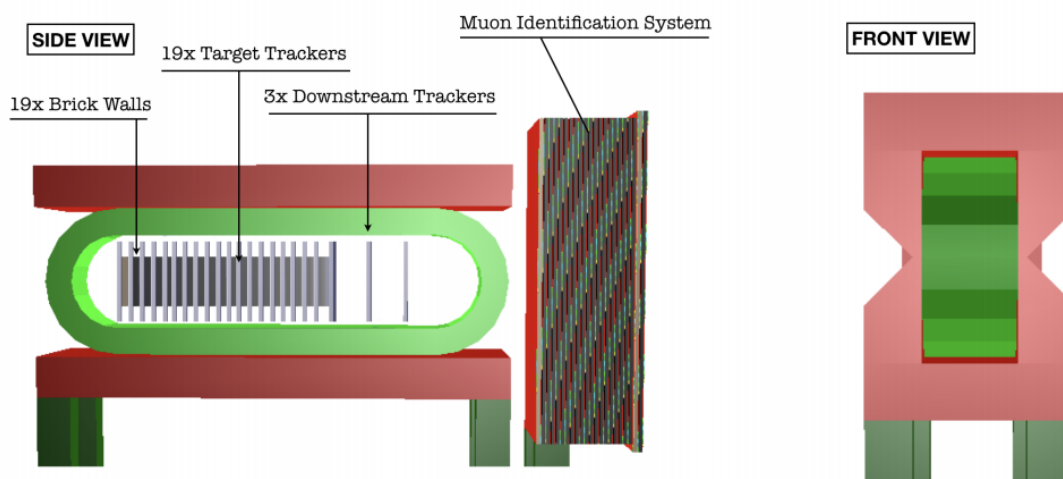

Figure 2.6: Layout of the scattering and neutrino detector. [14]

The main aim of this detector is to study neutrino tau interactions: as discussed in Section 2.2, only a few ν_τ interactions have been detected by previous experiments and no $\overline{\nu}_\tau$ has been observed yet. The SHiP experiment plans to achieve the first observation of a $\overline{\nu}_\tau$ interaction and to analyse tau neutrino interactions with a statistics three orders of magnitude larger than past experiments. In addition, observing the production of charmed hadrons in antineutrino interactions will provide precise knowledge of the strangeness component in the nucleon, because this production mode selects

anti-strange quark in the nucleon, whereas the presence of valence quarks in neutrino scattering makes the contribution of the d-quark compelling [2]. On the other hand the same detector may observe scattering of light dark matter, thus providing signals of new physics beyond the Standard Model.

2.4 Decay Spectrometer

The SHiP Decay Spectrometer (right part of Fig. 2.1) consists of the decay volume, the Surrounding Background Tagger (SBT), the Spectrometer Straw Tracker (SST), together with the large spectrometer magnet with a total field integral of about 0.5 Tm, the Timing Detector (TD), the Electromagnetic Calorimeter and the Downstream Muon Detector [11].
The Decay Spectrometer has to perform precise measurements of charged particles and photons originating from decay vertices of hidden particles in the decay volume, measure their momenta and energies, and provide PID information. Moreover, the Decay Spectrometer has to ensure a redundant background suppression using timing and track information from the TD and the SST, vetoing criteria from the upstream muon system of the SND and the SBT, and PID by the calorimeter and the muon systems.

2.4.1 Decay volume

Deep inelastic neutrino-nucleon scattering in the detector volume leads to background events through the production of V_0 particles (K_L, K_S, Λ) whose decays mimic the topology and modes of the hidden particle decays. With 2×10^{20} protons on target, a flux of $\sim 4.5 \times 10^{18}$ neutrinos and $\sim 3 \times 10^{18}$ anti-neutrinos is expected within the angular acceptance of the SHiP detector [11].
In order to suppress neutrino-induced background events in the fiducial decay volume, the experiment vacuum vessel is kept at a pressure of 1 mbar. In this configuration, neutrino interactions mainly occur in the vessel walls, where they can be easily rejected by using criteria based on the reconstructed impact parameter at the proton target. Residual neutrino interactions, as well as muon deep inelastic interactions with the vessel structure, are further suppressed by the Surrounding Background Tagger system, which is covering the entire decay volume and is capable of detecting the associated activity.
The SHIP vacuum vessel consists of two parts, the volume in which a decay vertex is accepted, and the spectrometer section. The spectrometer section runs through the spectrometer magnet and includes four tracker stations, which are symmetrically located with two stations upstream and two downstream of the magnet. An upstream and a downstream end-cap close off the ends of the vacuum vessel. As shown in Fig. 2.7,

the shape of the decay volume is a pyramidal frustum, with upstream dimensions of 2.2×5.0 m^2, downstream dimensions of 5.9×11.9 m^2 and length of 50 m [12]. The length of the decay volume is mainly defined by maximizing the acceptance to the different HS decay products given the transverse aperture of the spectrometer.
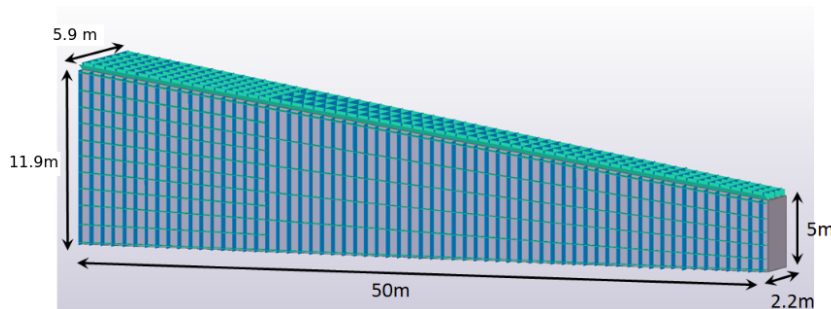

Figure 2.7: Overview of the structure of the decay volume showing the compartmentalization for the Surrounding Background Tagger.

2.4.2   Surround Background Tagger

The SBT detects charged particles either entering the vacuum vessel from outside or produced in the inelastic interactions of muons and neutrinos in the vacuum vessel walls. The SBT is sub-divided into individual cells integrated into the support structure of the vacuum vessel, each filled with a liquid scintillator consisting of linear alkylbenzene (LAB) together with 2.0 g/l diphenyl-oxazole (PPO) as the primary fluor (see Ch. 4). The cell size is 80 cm in the longitudinal direction and typically 120 cm in the transverse direction, depending on the location along the vacuum vessel. The compartmentalization of the SBT is shown in Fig. 2.7. The thickness of the liquid scintillator layer, surrounding the walls of the complete decay volume is about 30 cm, again varying along the length of the vacuum vessel. Each cell of the SBT is read out by two wavelength-shifting optical modules (WOM) that detect scintillation light in the range of 340 nm - 400 nm and transport the light to a ring of Silicon Photomultipliers directly coupled to the WOM tube.

2.4.3   Spectrometer Straw Tracker

The purpose of the Spectrometer Straw Tracker (SST) is to measure track parameters and momentum of charged particles with high efficiency and enough accuracy to reconstruct decays of hidden particles, and to reject background events. The precision of the

extrapolated position of the tracks must be well matched with the segmentation of the timing detectors such that the high accuracy of the associated track time can be used to remove combinatorial background. The invariant mass, the vertex quality, the timing, the matching to background veto taggers, and the pointing to the production target are crucial tools for rejecting background from spurious V^0 meson decays or from random combinations.

The spectrometer consists of a large aperture dipole magnet and two tracking telescopes on each side of the magnet. Four tracking stations are symmetrically arranged around the dipole magnet, as depicted in Fig. 2.8. The four stations are identical with a nominal acceptance of 5×10 m, and are based on ultra-thin straw drift tubes oriented horizontally. Each station contains four views, in a Y-U-V-Y arrangement, where U and V are stereo views with straws rotated by a small angle $\pm\theta_{stereo}$ around the z-axis with respect to the y-measuring straws. The straw tubes are made of thin polyethylene terephthalate (PET), as the tracking stations must minimise the contribution from multiple scattering, and are 5 m long, with a diameter of 20 mm [12].

The B field is about 0.14 T at its maximum and about 0.08 T at the location of the closest tracker stations, just outside the magnet. On the longitudinal axis the field integral between the second and third station is approximately 0.65 Tm.

2.4.4   Timing Detector

Background muons entering the vessel can potentially cross within the vertex reconstruction resolution and produce fake signals. One efficient way to distinguish random crossings from genuine physics events is to require the measured particle signals in the SHiP spectrometer to be coincident in time. In order to reduce combinatorial di-muon background to an acceptable level, a timing resolution of 100 ps is necessary. This requires the use of a dedicated timing detector placed in front of the calorimeter.

There are currently two options under investigation for this timing detector: plastic scintillators and multigap resistive plate chambers (MRPCs).

The design of the spectrometer timing using plastic scintillators consists of three columns of 182 horizontal bars with dimensions 168 cm ×6 cm ×1 cm, with 0.5 cm overlap between bars, for a total area of 5 m × 10 m. Each bar is read out on both sides by an array of eight 6 mm × 6 mm SiPMs. [12]

The alternative design is based on the timing Resistive Plate Chamber (tRPC) technology. The sensitive module is confined inside a completely sealed plastic box to ease the construction and allow operation with a low flux of gas. The chambers are made of stacks of glass plates, separated by 0.3 mm nylon mono-filaments. The outer glass plates are coated with resistive paint, and act as high voltage electrodes, while the inner ones
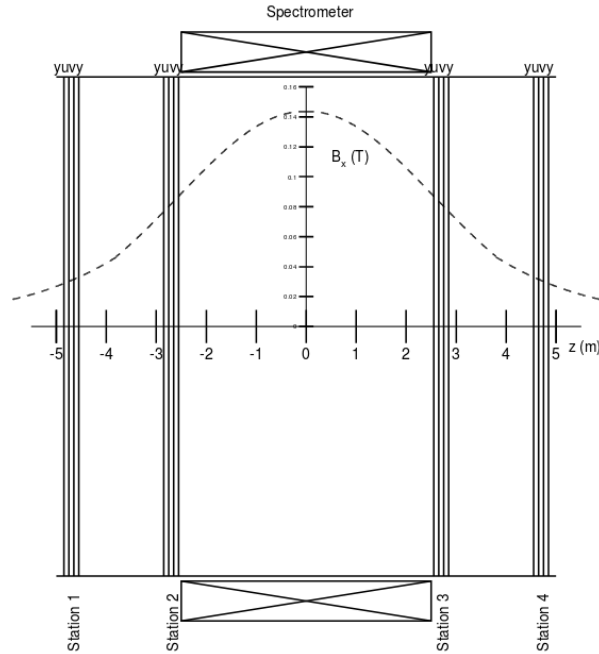
Figure 2.8: Position of the tracking stations and dipole magnet, overlaid with magnetic field component B_x as a function of z.

are left electrically floating. Signals induced by charged particles traversing the chamber are collected on segmented readout strips which lie along the x axis: the y coordinate of the incoming particle is therefore obtained directly from the fired strip while the x coordinate is derived from the average of the times registered on each end of the strips [11].

2.4.5   Electromagnetic calorimeter

The SHiP calorimeter handles a number of tasks. It must identify photons, electrons and π^0 mesons and provide measurements of their energies and positions. Furthermore, the calorimeter must contribute to the identification of charged pions and muons and to provide precise time information for event reconstruction. Electron/pion identification is necessary for the separation of $HNL \longrightarrow e \pm \pi^{\mp}$ decays from the main background channels such as $K_S^0 \longrightarrow \pi^+\pi$ and $K_L^0 \longrightarrow \pi^+\pi^-\pi^0$. Good photon identification and energy measurements are necessary for the correct reconstruction of the π^0s for several channels. For example, the reconstruction of the $HNL \longrightarrow l^{\pm}\rho^{\mp} \longrightarrow l^{\pm}\pi^{\mp}\pi^0$ channels,

where $l^{\pm}$ denotes electron or muon, and for channels involving decays of light mesons with photons in the final state. For the $HNL \longrightarrow l^{\pm}\pi^{\mp}\pi^0$ channel, the main background is $K_L^0 \longrightarrow \pi^+\pi^-\pi^0$, which has a branching ratio of 12.5%, that can also be rejected with a precise invariant mass measurement [2]. It is therefore necessary to have an optimal calorimeter energy resolution giving an invariant mass resolution similar to that given by tracking. The calorimeter system also aids in pion/muon discrimination and in the identification of muons, especially in the low momentum region ($p < 5$ GeV/c) where a sizeable fraction ($\sim 14\%$) of muons from a 1 GeV/c^2 HNL can be produced but they may not reach all the sensor planes of the muon detector.

The calorimeter is placed at the end of the vacuum vessel right after the timing detector. Its design consists of a 25 X_0 long sampling calorimeter, with lead absorber plates orthogonal to the proton beam direction, and with two kinds of active layers [15]. Most sampling layers are equipped with scintillator bars read out by WLS fibres with a relatively coarse spatial segmentation. The lead absorber plates are 0.5 X_0 thick, i.e. 0.28 cm, while the scintillator is 0.56 cm thick. Three high resolution gas detector layers, 1.12 cm thick, one located after 3 X_0 and the other two around the shower maximum at 10 X_0 and 13 X_0 , to cover the range for both low and high energy showers, will determine the transverse position of the shower at the three depths and allow for reconstruction of the photon angle. To obtain a desired performance of few mrad angular resolution, the three high resolution active layers need to have a high spatial segmentation of about 200 μm, that can be achieved with micro-pattern gas detectors or alternatively scintillating fibre detectors.

The Muon Detector is placed downstream the electromagnetic calorimeter. Its design is described in detail in the next chapter.

Chapter 3

SHiP Muon Detector

3.1 Technical specifications and required performance

The muon system is placed downstream of the calorimeter system. The detector is mainly responsible for identifying muons with high efficiency and for discriminating them from pions escaping the calorimeter.
These particles are originated in signal processes [2], such as:

- $HNL \longrightarrow \pi^+\mu^-$ and $HNL \longrightarrow \mu^+\mu^-\nu_\mu$ in the neutrino portal;

- $V \longrightarrow \mu^+\mu^-$ in the vector portal;

- $S \longrightarrow \mu^+\mu^-$ in the scalar portal;

that need to be distinguished from $\nu-$ and $\mu-$induced backgrounds, consisting mostly of $K_L \longrightarrow \pi^\pm\mu^\mp\nu_\mu$ and $K_S \longrightarrow \pi^+\pi^-$ decays originating in the material surrounding the decay volume.
Random combinations of beam-induced muons that escape the hadron absorber and the active filter can form a fake vertex inside the decay volume and mimic $HNL \longrightarrow \pi^+\mu$ decays if one of the two muons is misidentified as pion. These are typically high momentum tracks, so the particle identification system has to minimize the $\mu \longrightarrow \pi$ misidentification probability in the entire interesting momentum range.
This background can be reduced by applying a timing cut [11]. In fact, beam-induced muons are uniformly distributed over the spill duration (~ 1 s) while the decay products of long-lived particles arrive almost simultaneously at the spectrometer. The probability that two combinatorial muons mimic a decay of a long lived particle depends linearly on the time window in which the arrival times of the two muons are recorded. By requiring a tight ($< 1ns$) time coincidence of candidate muon tracks, the muon system can

contribute to the rejection of the combinatorial background, and its effectiveness scales with the time resolution of the detector.

The momentum interval covered by the muon system ranges from ∼2.6 GeV/c up to ∼100 GeV/c, the lower threshold being defined by the minimum momentum needed for a muon to cross the calorimeter system. Muons and pions with momentum lower than ∼3 GeV/c can be identified using the calorimeter system alone.

The rate seen by the muon detector is mostly due to the beam-induced muon background. Preliminary simulation studies (Fig. 3.1) show that the flux of muons is ∼ 50 kHz over the entire muon detector area, corresponding to a rate of < 0.1 Hz/cm² [11]. For this reason, a modest rate and radiation tolerance of the detector are sufficient.
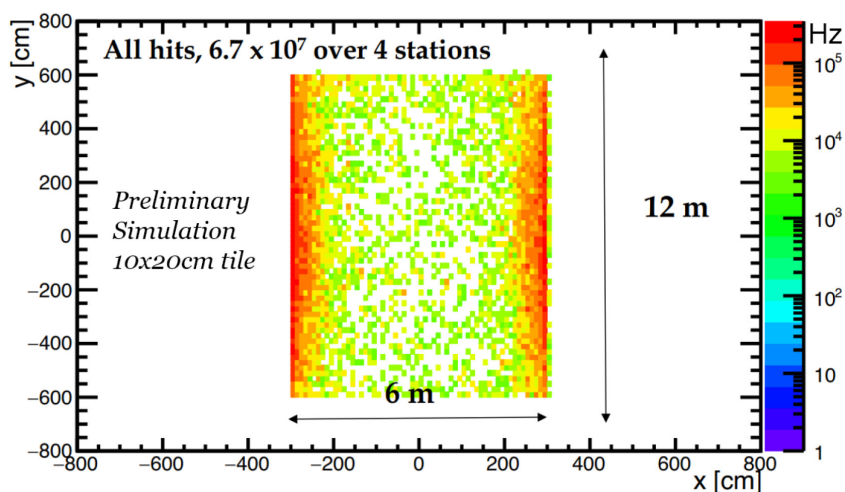

Figure 3.1: Preliminary simulation of hit rate in the muon detector, here segmented in 10 × 20 cm tiles.[16]

Finally, a moderate position resolution completes the requirements for the muon detector, as the position error is dominated by the multiple scattering of muons in the material of the calorimeter. Preliminary simulation studies show that a granularity of ∼ 5-10 cm in the transverse direction is adequate for the interesting momentum range.

To summarize, the required specifications of the detector are:

- very high (> 99%) efficiency for muon identification with $p > 3$ GeV/c;

- pion misendintification < 0.1%;

- spatial resolution of ∼ 10 cm,

- high time resolution (≪ 1 ns).

3.2 Detector layout

The muon detector consists of a system of four stations of active layers interleaved by three muon filters [11]. The detector layout is shown in Figure 3.2. The stations are 6 m wide, 12 m high, for a total active surface of 288 m^2.
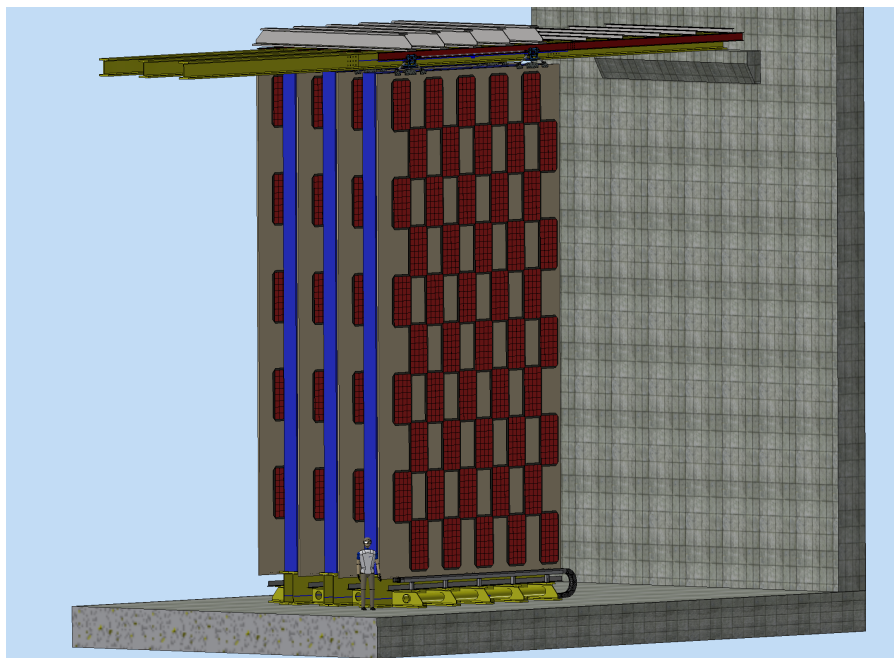

Figure 3.2: Muon detector layout. The active layer is segmented in detector modules, depicted in red, placed on a supporting structure. The passive filters are drawn in blue.

Concerning the passive filter technology, two options are currently being considered. The first one, that was presented in the Detector Technical Proposal [11], consists of 50 cm thick iron walls, corresponding to 3 λ_I each. The possibility of repurposing the iron slabs of the OPERA experiment is currently under evaluation. As an alternative, concrete walls can be used, but with a thickness of 120 cm in order to have the same number of interaction lengths. This option reduces costs significantly and is of easier construction. However, the increased thickness of the filters leads to more scattering of the muons. Therefore, it is necessary to conduct further studies to determine whether this affects the sensitivity and efficiency of the detector.

A muon with normal incidence must have an energy of at least of 2.6 GeV/c to reach the first muon station and at least 5.3 GeV/c to reach the last muon station. Other particles escaping the calorimeter produce a shower in the iron filters.

Given the detector requirements, the technology chosen for the active layers is plastic scintillators read out by silicon photomultipliers (SiPMs). The reason behind this choice is the fact that this technology is straightforward to operate, as no high voltage or flammable gases are employed, it does not have substantial aging problems, has high detection efficiency and can achieve a very good time resolution. Other reasons for such a choice are: simple segmentation, robust and straightforward construction, long-term stability, low maintenance, high reliability and cost-effectiveness, all crucial aspects for building a large area detector.

3.3 Active layer design

The first design of the active layer, as reported in the SHiP Technical Proposal [11], was based on extruded plastic scintillator bars with wavelength-shifter fibers and silicon photomultiplier (SiPMs) readout. The scintillating bars were 5 cm wide, 3 m long and 1 cm thick. The crossing of horizontal and vertical bars could provide the x,y view in each muon station with a readout granularity of 5 cm. A thorough R&D has been carried out on this technology, and the results are summarized here [17]: a time resolution of $\sim$800 ps has been measured on 3 m long bars, dominated by the variance of the fiber scintillation time.

Considering the highly non uniform hit rate (Fig. 3.1 shows that hits are concentrated on the sides of the detector) and the need for a sub-ns time resolution in order to reduce effectively the combinatorial background, a different technology was consequently considered: scintillating tiles with direct SiPM readout [12]. This option is more robust against hit rate variations and has several advantages, including an intrinsically better time resolution and easier mechanical construction.

Taking into account an area of ~ 200 cm^2 per tile, the full detector will require approximately 3400 tiles per active layer. It is then clear that a careful design and development of these tiles is necessary in order to reduce the number of readout channels and overall detector costs, while complying with the detector requirements.

The active layers are composed of individual modules for easier construction and maintenance, placed on a mechanical support structure. Each module will be enclosed in a case for electromagnetic and light insulation. The modules placement is shown in Fig. 3.3, they are disposed in a checkered pattern on both sides of the supporting structure, staggered to cover the whole layer area. This pattern allows both to reduce the dead area between modules and an even weight distribution on the support structure.

The active layers are installed on sliding tracks to allow for an easier access to modules in case of maintenance. Fig. 3.4 shows muon detector with its layers pulled out on the side.
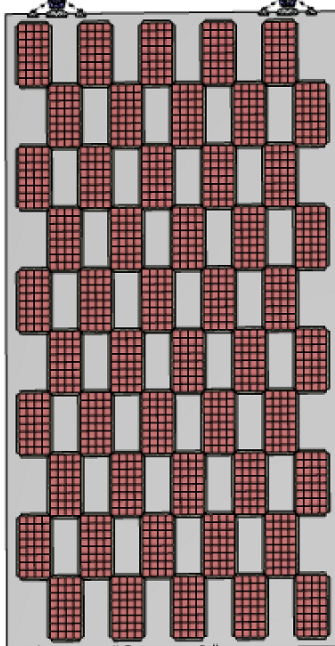
Figure 3.3: Modules placement on the active layer support structure. On the backside their pattern is identical but staggered.

3.3.1   Tiles

Tiles are the basic building block of the active layer. They are made of plastic scintillator directly coupled with silicon photomultipliers. Blue sensitive SiPMs are employed in order to match the scintillating light spectrum of the chosen scintillator. Tiles will be made light-tight by either a aluminized mylar wrapping or a titanium dioxide paint coating, that will enhance scintillation light collection as well.

The intrinsic time resolution of scintillators, SiPMs and electronics can reach well below 100 ps, and in our case the limit is given by the uncertainty in the hit position and subsequent light propagation delay spread. The feasibility of a detector based on tiles has been demonstrated with preliminary tests on 6×6 cm^2 tiles [16], that showed that a time resolution of ~ 260 ps can easily be achieved for that size. Through the optimization of the SiPM type and placement along the tile, as well as coating type, we aim at achieving < 400 ps on a tile with an area of about 200 cm^2. In this way the detector, with a high-quality global timing distribution, can reach a < 200 ps time resolution combining four layers.
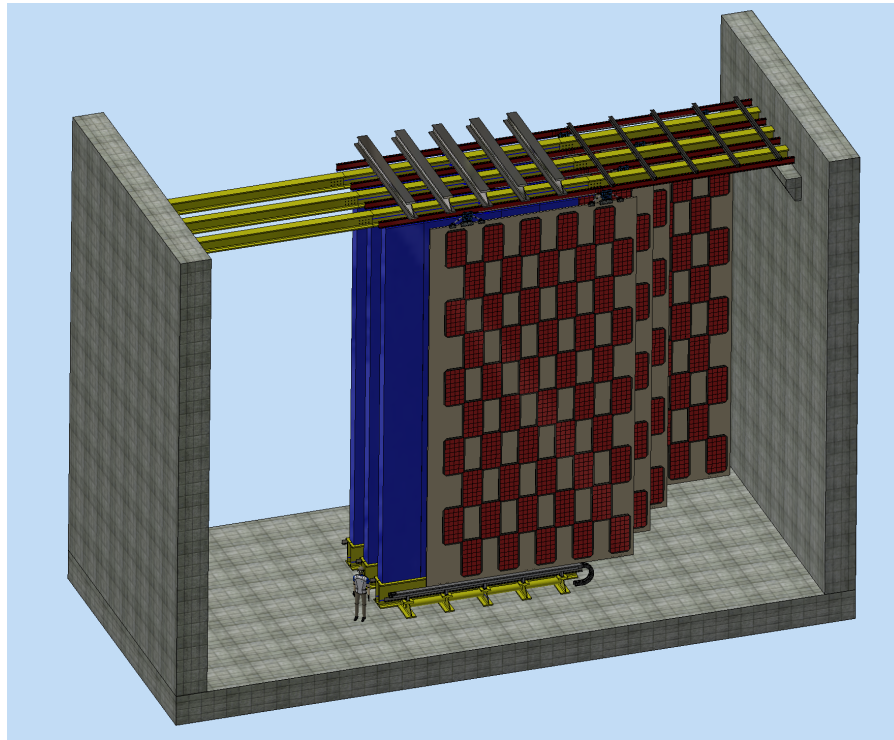
Figure 3.4: Displaced active layers for easier access during maintenance.

Various configurations have been proposed, with optimizations of both time resolution and cost effectiveness, considering the production size for the detector. At the moment, two main configurations are under investigation.

Rectangular Tile

The first design has been developed by the INFN Laboratories of Frascati. It consists of a rectangular tile with dimensions of 10×20 cm. The tile is read out by six SiPMs, symmetrically placed on the longer sides, three per side. These SiPMs have a sensitive area of 4×4 mm^2 and are produced by Hamamatsu. The MUSIC [18], an 8-channel integrated circuit specifically developed for SiPM readout, provides amplification the SiPM signals and their analog sum.

This tile can reach a time resolution of about ~ 320 ps, meeting the intended objective. However, some characteristics of this tile configuration can be improved: for
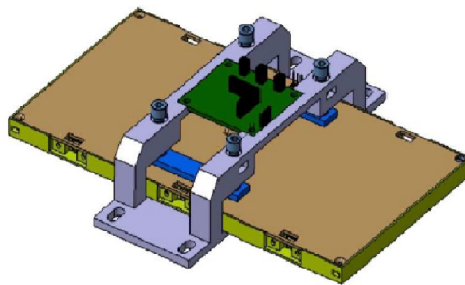
Figure 3.5: Rectangular tile, with six SiPMs read-out and ASIC digitizer board.

example, the electronic readout, while having shown a good overall perfomance during tests, may be too expensive for employment in a large area detector. Moreover, this tile has some "blind" spots: in the corners the light signal cannot be seen very well by the closest SiPM due to refraction effects, and thus the signal is slower as photons have to reach a SiPM on the opposite side. A narrow spread in propagation delay is crucial to obtain a good time resolution, and these effect can be attenuated with a different placement of the SiPMS, like the one illustrated in the next paragraph.

Square Tile

A square tile was proposed to improve on the rectangular tile design. The tile area is 15 × 15 cm^2, slightly larger than the rectangular one, and is read out by four SiPMs instead of six [16]. This allows to reduce the number of required components, further reducing costs. In this case blue-sensitive SiPMs are employed as well, and several models are currently under evaluation. The SiPMs are placed on the tile corners, which are beveled at 45 degrees, as shown in Fig. 3.6. This configuration allows to mitigate the blind areas that the rectangular tile had, and have a more homogeneous time response.

The readout circuit for amplification and analog sum of the SiPMs output is based on discrete components and has been designed specifically for this tile configuration. A detailed description of the latter, and of the tile components working principles as well, can be found in next chapter. This read out solution is convenient because it allows to mount the amplifier very close to the SiPM, minimizing the electronic noise and cabling costs.
This thesis focuses on the development and optimization of this tile configuration, carried out by the INFN section of Bologna. In the next chapters, the details of the tested prototypes with different configurations will be shown, as well as the measurements carried out to evaluate their performance.
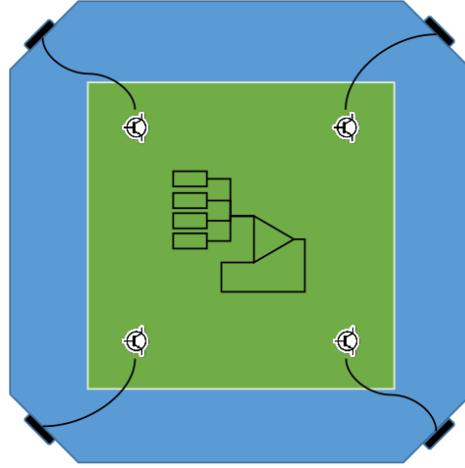
Figure 3.6: Square tile with simplified diagram of readout electronics.

3.3.2   Detector Module

For an easier assembly of the full detector, 32 tiles will be preassembled in a module to-
gether with a digitizer board. This configuration minimizes the length of analog cabling
as well.

The actual tiles arrangement is currently under evaluation, with two possible configura-
tions. These designs employ the square tiles as baseline technology: the first one exhibits
tiles placed next to each other, as shown on the left side of Fig.3.7, leaving a small per-
centage ($< 0.5\%$) of dead area due to the tile beveled corners. This configuration allows
an easy mechanical assembly.

In other one instead, on the right side of Fig.3.7, the tiles are overlapped for 1 cm in
the y direction. This configuration requires a more complicated design for a supporting
structure, but reduces effectively the dead area. Digitization of the signal is foreseen to
be done by the SAMPIC WaveformTDC [19] (Fig. 3.8), a 16 channel switched capacitor
digitizer. This device records pulses in a fast analog memory with a 64 cell depth, at
11 bit vertical resolution. Each channel also integrates a discriminator that can trigger
itself independently or participate to a more complex trigger. After triggering, analog
data is digitized by a on-chip Analog to Digital Converter (ADC) and is sent serially
to the DAQ. Offline interpolation allows for better than 10 ps resolution on threshold
crossing time.

The SAMPIC has a relatively large dead time (1 μs), but this does not represent a
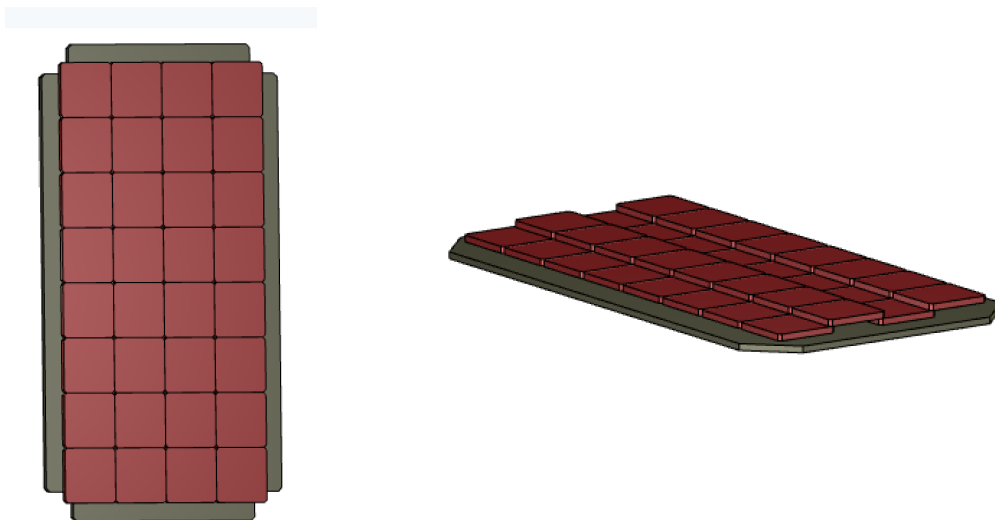limitation, given the low expected occupancy per channel in the muon detector. Two

Figure 3.7: Module mechanical designs. On the left, tiles are placed next to each other, on the right, tiles are slightly overlapped in the y direction in order to reduce dead areas.

Figure 3.8: SAMPIC WaveformTDC.

SAMPICs can be mounted in one digitizer board, together with a small FPGA, to instrument one module of the detector. Fig. 3.9 show a conceptual scheme of the digitizer board, in a simplified case with eight tiles. Groups of four or eight tiles share the low voltage and bias channels to reduce the number of components. Moreover, the board is equipped with sensors for monitoring environmental and component temperature.
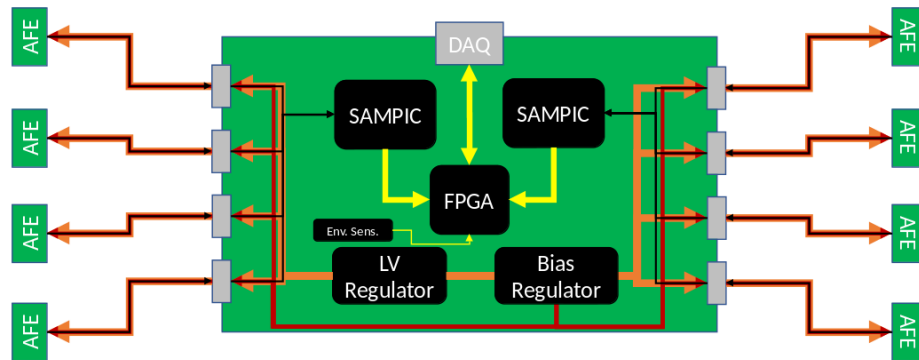
Figure 3.9: Conceptual scheme of the digitizer board.

Chapter 4

Scintillation detectors

In this chapter the working principles of a scintillator detector equipped with Silicon Photomultipliers are presented.

4.1 Scintillators

When a charged particle traverses matter, it excites molecules along its path. When they return to the ground states, certain types of molecules release a small fraction of this energy as photons of the visible or near to visible light spectrum. This process is known as scintillation, and a material in which the conversion of excitation energy into light is highly efficient is called scintillator.

While many scintillating materials exist, not all are suitable as detectors. In general, a good detector scintillator should satisfy the following requirements [20]:

- high efficiency of light production;

- short decay constant (fast signal);

- transparency to its own scintillation light;

- emission spectrum overlapping with the spectral response of photon detectors.

No material simultaneously meets all criteria, and the choice of scintillator is often a compromise among these factors. Scintillators are broadly divided into organic and inorganic scintillators. Their characteristics will be explained in detail in the next sections, focusing in particular on organic scintillators.
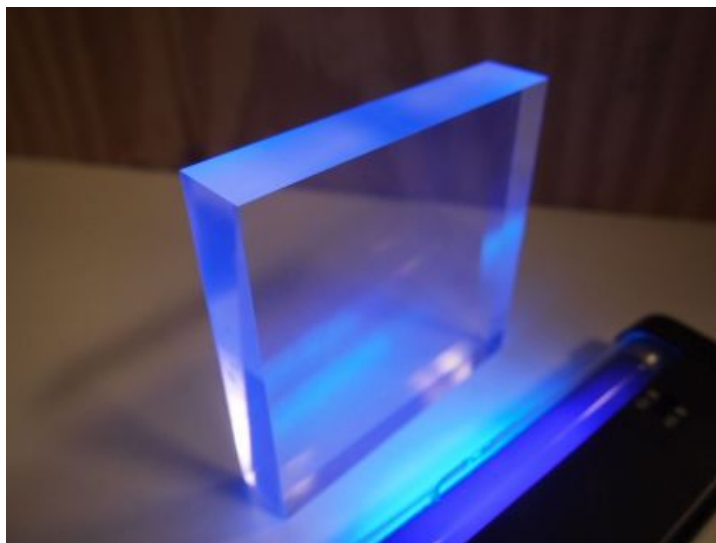
Figure 4.1: A plastic scintillator illuminated by UV light.

4.1.1   Inorganic Scintillators

Most of the inorganic scintillator materials, known as phosphors, are salt crystals, often activated with dopants. The most common types are alkali halides, activated by heavy metals such as thallium, and zinc sulphide, activated by copper, silver or manganese. Inorganic scintillators depend primarily on the crystalline energy band structure of the material for the scintillation mechanism [21]. Figure 4.2 shows an energy band diagram for a typical inorganic scintillator. If a charged particle interacts in the scintillation material, it can excite numerous electrons from the valence and lower-bound bands up into the conduction bands.

These electrons rapidly lose energy and fall to the conduction band edge E_C. As they de-excite and drop back into the valence band, they can lose energy through light emissions. If the radiated energy is equivalent to E_g, the radiated photons can be re-absorbed, and the scintillator is essentially opaque to its own emissions. An impurity added to the crystal can introduce allowed states in the band gap (depicted in Fig. 4.2b), called activated scintillator. The excitation process remains similar to that of the intrinsic case. However, a significant fraction of electrons can fall into the activator excited state. Transitions to the activator ground state release sub-band-gap photon energies and avoid reabsorption. There are exceptions in which intrinsic scintillators work well without activators; examples are bismuth germanate ($Bi_4Ge_3O_{12}$ or BGO) and barium fluoride (BaF_2).
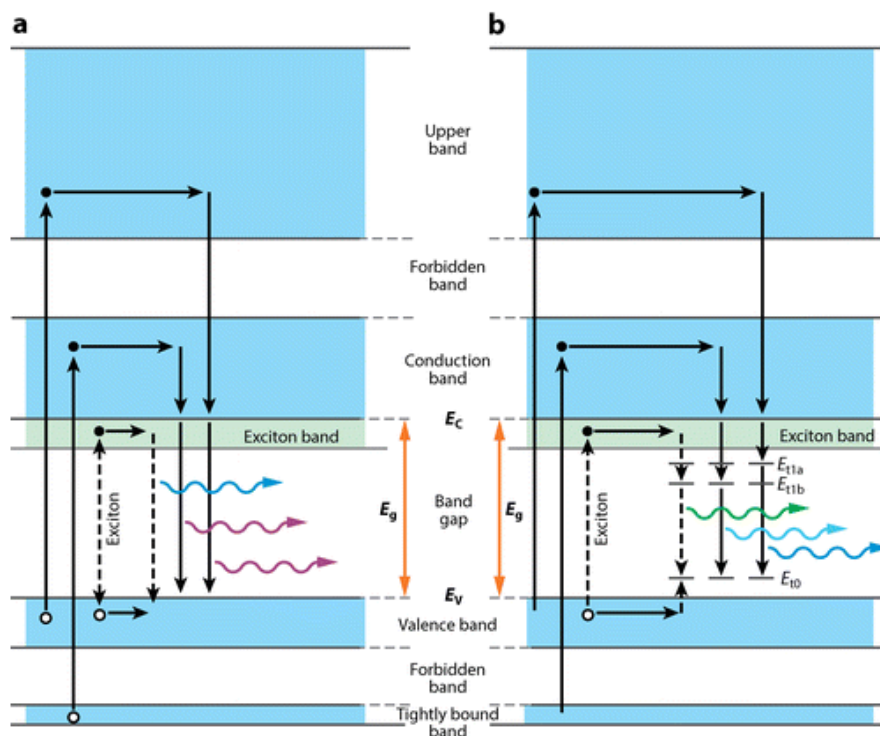
Figure 4.2: Two basic methods by which an inorganic scintillator produces light: (a) the intrinsic case and (b) the extrinsic case, in which an activation material is added to the scintillator. [21]

4.1.2 Organic Scintillators

The organic scintillators are aromatic hydrocarbon compounds containing linked or condensed benzene-ring structures. Organic scintillators use the ionization produced by charged particles to generate optical photons, usually in the blue to green wavelength region. Their most distinguishing feature is a very rapid decay time of the order of a few nanoseconds or less.

Scintillation Mechanisms

Scintillation light in organic compounds arises from transitions made by the free valance electrons of the molecules [22]. These delocalized electrons are not associated with any

particular atom in the molecule, and occupy the π-molecular orbitals. Energy deposition from a charged particle passing through the material excites the electrons from the ground state to higher-energy excited states.

The excess energy can be dissipated in various ways. The energy of incident radiation is transferred to particular atoms, causing an electron transition from the basic S^0 state to the excited state S^1 or higher, depending on the energy. Non-radiative transitions occur quickly between vibrational sub-states of S^1 (dashed arrows in Fig. 4.3) to the S^1 basic state.

Then, there is an electron transition from S^1 to S^0 state. The excess of the energy is radiated as fluorescence photons within UV or visible wavelengths.

For scintillation detectors, the transition from S^1 vibrational states to S^1 base level is favorable. In such decay electrons lose a part of their energy and, as a consequence, the absorption and emission spectra of scintillating materials are shifted as a function of light wavelength. In this way, the absorption and emission spectra of such materials do not match, hence disfavoring the re-absorption of the scintillation light in the material.

The above mentioned S-band transitions are not the only transitions possible in organic scintillators. Another mode of electron relaxation is through the vibrational levels in the triplet T^0 band. The process is graphically depicted in on the right side of Fig. 4.3.
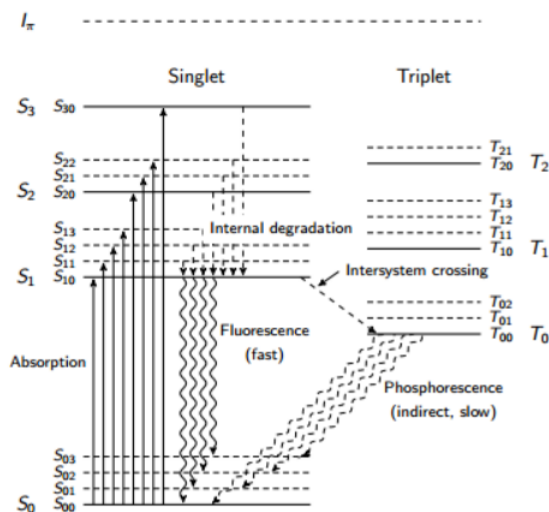

Figure 4.3: Scheme of the singlet and triplet energy level diagram of organic scintillators.

As before, the incident radiation transfers the electrons from the S^0 ground level to the S^1 vibrational levels. These electrons first decay into the S^1 ground level through radiationless transitions. Now, instead of falling into the S^0 level directly, the electrons

can also first go to the available T^0 levels. These triplet levels are much more stable than the singlet levels, and consequently the electrons can be thought of being trapped there for an extended time. From the T^0 ground level, into which all electrons eventually decay, they fall into the S^0 levels. This also results in the emission of light, but in this case it is called phosphorescence or delayed fluorescence since it is emitted after a substantial delay, which is more than 100 ns for typical organic scintillators.

4.1.3   Plastic scintillators

If an organic scintillator is dissolved in a solvent that can be then be subsequently polymerized, the equivalent of a solid solution can be produced. A common example is a solvent consisting of styrene monomer in which an appropriate organic scintillator is dissolved. The styrene is then polymerized to form a solid plastic. Other plastic matrices can consist of polyvinyltoluene or polymethylmethacrylate. Because of the ease with which they can be shaped and fabricated, plastics have become an extremely useful form of organic scintillator.

Typical plastic scintillators are ternary systems, consisting of three components: polymeric base, primary fluor and secondary fluor, so-called *wavelength shifter* (WLS). A scheme of energy transfer in plastic scintillator is shown in Fig. 4.4.
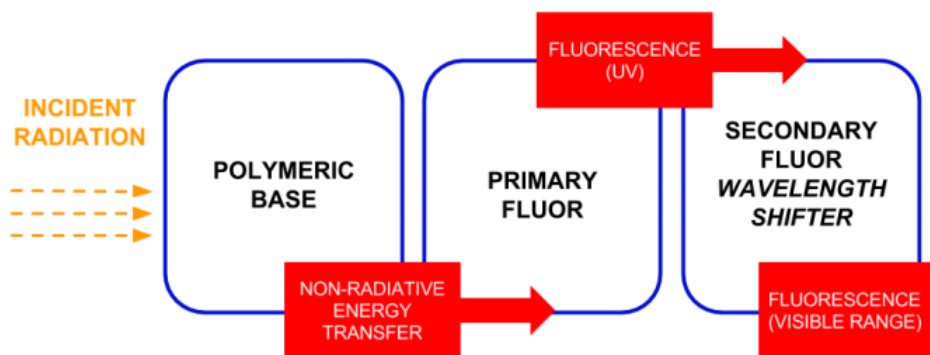

Figure 4.4: Block scheme of energy transfer in plastic scintillators.

Three components of the plastic scintillators are shown in Fig. 4.4 in particular a sequence, however the scintillator is a homogeneous mixture of these chemical compounds. The incident radiation interacts with polymer molecules exciting them. The energy is transferred in a non-radiative way to the primary fluor through the Förster mechanism

[23]. The primary fluor absorbs the energy and emits it in the UV range via fluorescence. This wavelength is not adjusted to the quantum efficiency of the light detectors and suffers from high re-absorption. To shift the maximum wavelength of emission towards larger wavelengths, a wavelength shifter is used. This substance absorbs the light emitted by the primary fluor, and as a result, photons in the visible range are produced. Such light can be efficiently detected by a photodetector.

Chemical compounds

Plastic scintillators are obtained by polymerization of the liquid monomer in which scintillating additives are dissolved. In effect, a block of homogeneous scintillator can be obtained. Nowadays, polyvinyltoluene (PVT), $[CH_2CH(C_6H_4CH_3)]_n$, is the most widely used matrix for plastic scintillators base because of the best scintillating properties among polymers. Polystyrene (PS), $(C_8H_8)_n$, its homologous compound, is very popular as scintillator matrix as well. There is a large number of chemical compounds, that can be used as primary fluors in plastic scintillators. Some of them are presented in Tab. 4.1 [23].

There are also large number of substances that can be used as wavelength shifters in plastic scintillators. Some of them are presented in Tab. 4.2[23].

4.1.4 Plastic scintillators response

Light output

A small fraction of the kinetic energy lost by a charged particle in a scintillator is converted into fluorescent energy. The remainder is dissipated non radiatively, primarily in the form of lattice vibrations or heat. The fraction of the particle energy that is converted (the scintillation efficiency) depends on both the particle type and its energy. In some cases, the scintillation efficiency may be independent of energy, leading to a linear dependence of light yield on initial energy.
For organic scintillators such as anthracene, stilbene, and many of the commercially available liquid and plastic scintillators, the response to electrons is linear from particle energies above about 125 keV [24]. The response to heavy charged particles such as protons or alpha particles is always less for equivalent energies and is non linear to much higher initial energies.

The response of organic scintillators to charged particles can best be described by a relation between dL/dx, the fluorescent energy emitted per unit path length, and dE/dx, the specific energy loss for the charged particle. A widely used relation first suggested
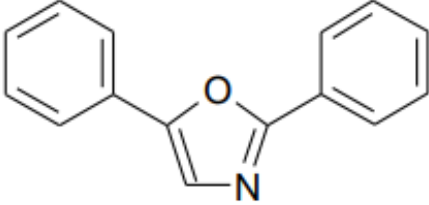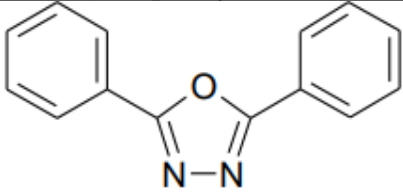
Chemical structure, name	Abbreviation	$\lambda_{em}(nm)$	τ (ns)
p-terphenyl	PTP	335	1.2
2,5-diphenyloxazolel	PPO	365	1.6
2,5-diphenyl-1,3,4-oxadiazole	PPD	355	1.5

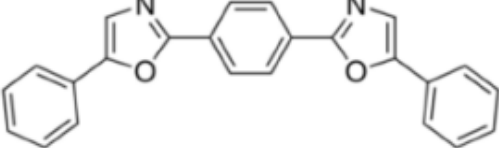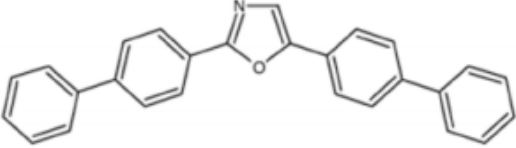Table 4.1: Substances that can be used as primary fluors in plastic scintillators.

Chemical structure, name	Abbreviation	$\lambda_{em}(nm)$	τ (ns)
1,4-bis(5-phenyl-2-oxazolyl)benzene	POPOP	417	1.5
2,5-di(4-biphenylo)oxazole	BBO	410	1.4

Table 4.2: Substances that can be used as secondary fluors (wavelength shifters) in plastic scintillators.
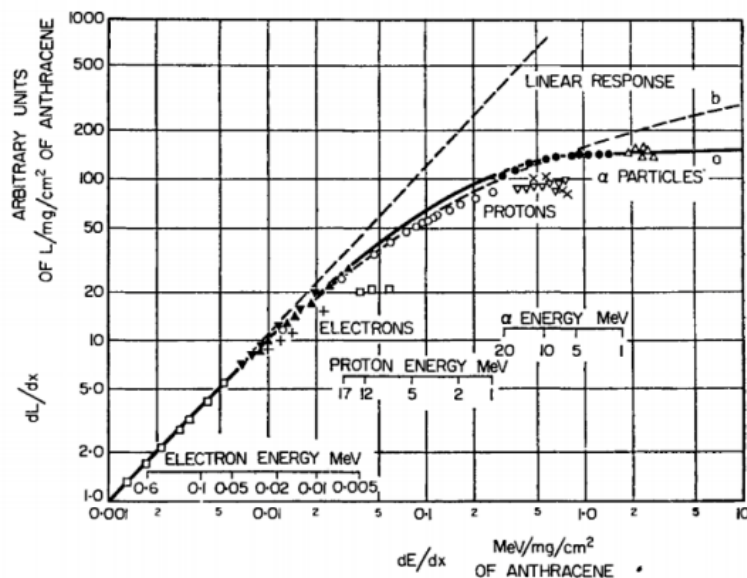
Figure 4.5: Variation of specific fluorescence with specific energy loss for anthracene.

by Birks is based on the assumption that a high ionization density along the track of the particle leads to quenching from damaged molecules and a lowering of the scintillation efficiency. The light output per unit length, dL/dx, is related to the specific ionization by:

$$\frac{dL}{dx} = \frac{A\frac{dE}{dx}}{1 + kB\frac{dE}{dx}} \tag{4.1}$$

with A: absolute scintillation efficiency; kB: parameter relating the density of ionization centers to dE/dx (kB is obtained by fitting Birk's forumla to experimental data) [20].

Timing response

If it can be assumed that the luminescent states in an organic molecule are formed instantaneously and only prompt fluorescence is observed, then the time profile of the light pulse should be a very fast leading edge followed by a simple exponential decay. More accurately, two other effects must be taken into account: the finite time required to populate the luminescent states, and the slower components of the scintillation corresponding to delayed fluorescence and phosphorescence [24].

Times of approximately half a nanosecond are required to populate the level from which the prompt fluorescence light arises. For the very fast scintillators, the decay time

from these levels is only three or four times greater, and a full description of the expected pulse shape must take into account the finite rise time as well. One approach assumes that the population of the optical levels is also exponential and that the overall shape of the light pulse is given by:

$$I = I_0(e^{-t/\tau} - e^{-t/\tau_1}) \tag{4.2}$$

where τ_1 is the time constant describing the population of the optical levels and τ is the time constant describing their decay. Other observations have concluded that the population step is better represented by a Gaussian function $f(t)$ characterized by a standard deviation σ_{ET}. The overall light versus time profile is then described by:

$$\frac{I}{I_0} = f(t)e^{-t/\tau} \tag{4.3}$$

Pulse shape discrimination

For the vast majority of organic scintillators, the prompt fluorescence represents most of the observed scintillation light. A longer-lived component is also observed in many cases, however, corresponding to delayed fluorescence. The composite yield curve can often be represented by the sum of two exponential decays - called the fast and slow components of the scintillation (Fig. 4.6) [20] .
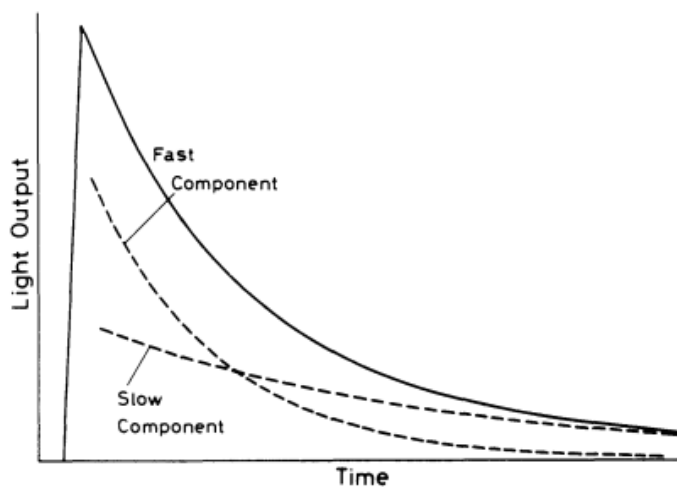

Figure 4.6: Resolving scintillation light into fast (prompt) and slow (delayed) components. The solid line represents the total light decay curve.

Compared with the prompt decay time of a few nanoseconds, the slow component will typically have a characteristic decay time of several hundred nanoseconds. Because the majority of the light yield occurs in the prompt component, the longer-lived tail would not be of great consequence except for one very useful property: the fraction of light that appears in the slow component often depends on the nature of the exciting particle. One can therefore make use of this dependence to differentiate between particles of different kinds that deposit the same energy in the detector.

4.2 Silicon Photomultipliers

Semiconductor materials, especially silicon, are widely researched and adopted in building photodetectors. Although the vacuum photomultiplier tubes are still the most commonly used photodetectors in many fields, it is a common trend that silicon photodetectors of different kinds start replacing PMTs or being considered as the first choice when building new detectors.

Silicon has several unique properties that makes it a suitable material for photodetectors. Compared with vacuum photomultiplier tubes, silicon photodetectors have a higher quantum efficiency over a wide range of wavelengths. Photons induce a signal in silicon by lifting an electron from the valence band to the conduction band. It generally requires less energy than kicking a free electron into the vacuum from a photocathode of a PMT. Silicon photodetectors are insensitive to strong magnetic fields while PMTs require magnetic shielding to be properly operated. This feature makes the application of silicon photodetectors possible where conventional PMTs cannot be employed. The compactness of silicon photodetectors also allows high channel density or miniaturized detectors to be built. Furthermore, silicon is the fundamental material for most electrical components and circuits. The development of the silicon fabrication technique in the electrical engineering industry is also beneficial in reducing the cost and adopting mass production of the silicon photodetectors. Moreover, it would be possible to integrate functionality and readout circuits directly in the photodetector, further extending its capability.

4.2.1 Working principle

Silicon Photomultipliers consist of a matrix of independent micro-cells (pixels) that are connected in parallel. Each pixel is formed out of a photodiode and quench resistor in series [25]. Fig. 4.7 shows a simplified electric scheme of a SiPM.

The photodiodes are Single-Photon Avalanche Diodes (SPADs), which are based on a silicon p-n junction that creates a depletion region that is free of mobile charge carriers.
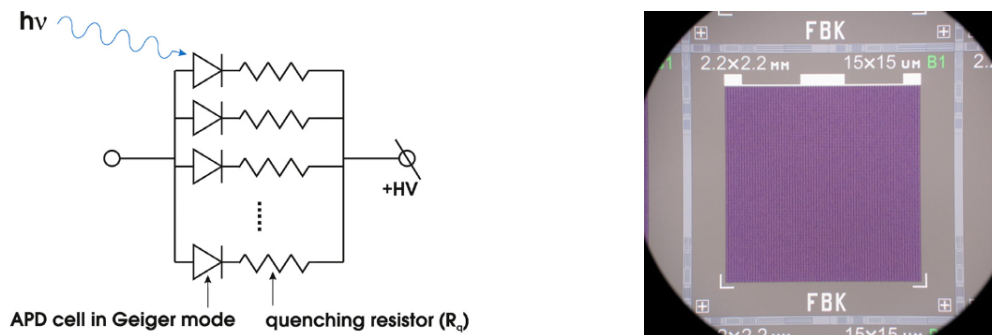
Figure 4.7: On the left, a simplified electric structure of an SiPM composed of several APD cells in parallel but with each one with a quenching resistor in series. On the right, magnified view of a SiPM. [26]

When a photon is absorbed in silicon it will create an electron-hole pair. Applying a reverse bias to a photodiode sets up an electric field across the depletion region that will cause the charge carriers to be accelerated toward the anode (holes) or cathode (electrons) (Fig. 4.8). When a sufficiently high electric field ($> 5 \cdot 10^5$ V/cm) is generated within
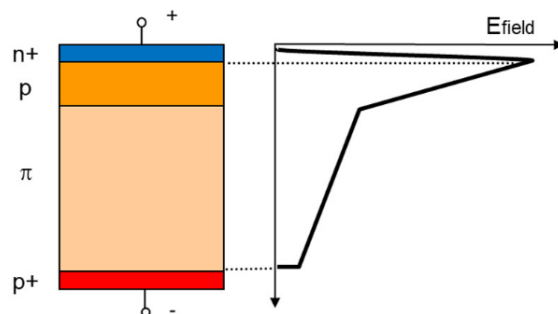

Figure 4.8: Sketch of a possible doping structure of a p on n SPAD and electric field strength in operation mode

the depletion region of the silicon, a charge carrier created there will be accelerated to a point where it carries sufficient kinetic energy to create secondary charge pairs through a process called impact ionization. In this way, a single absorbed photon can trigger a self-perpetuating ionization cascade that will spread throughout the silicon volume. This process is called Geiger discharge, in analogy to the ionization discharge observed in a Geiger-Müller tube. In order to be sensitive to successive photons, every avalanche breakdown is interrupted by a built-in quench resistor which limits the current drawn by

the diode during the breakdown. This lowers the reverse voltage seen by the diode to a value below its breakdown voltage, thus halting the avalanche. The diode then recharges back to the bias voltage and is available to detect subsequent photons.

A typical SiPM anode-cathode output pulse is shown in Fig. 4.9. The rise time of the SiPM is determined by the rise time of the avalanche formation and the variation in the transit times of signals arriving from different points on the sensors active area. Minimizing this transit time spread can improve the rise time. In addition, the rise time is affected by the output impedance of the sensor and the package.
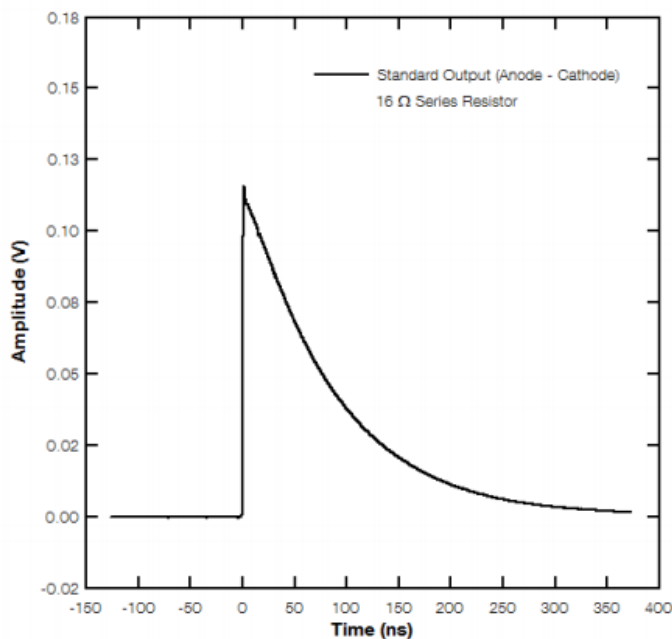

Figure 4.9: Output pulse read out from the anode-cathode of a SiPM.

The recovery time of the sensor, or decay time of the pulse, is determined by the microcell recharge time constant, which is given by [27]:

$$\tau_{RC} = C_d(R_q + R_s \cdot N) \tag{4.4}$$

where C_d is the effective capacitance of the microcell, R_q the value of its quench resistor, N is the total number of microcells in the sensor and R_s is any resistance in series with the sensor.

4.2.2 Performance parameters

Breakdown Voltage and Overvoltage

The breakdown voltage (V_{br}) is the minimum voltage that should be applied to a SiPM to create a Geiger discharge after a photon absorption [28]. The V_{br} point is clearly visible with a sudden increase in current in a dark current versus voltage plot, as shown in the example on the left in Fig. 4.10. The precise value of the V_{br} is determined as the value of the voltage intercept of a straight line fit to a plot of $\sqrt{I}$ vs V, as shown in Fig. 4.10, on the right [27].
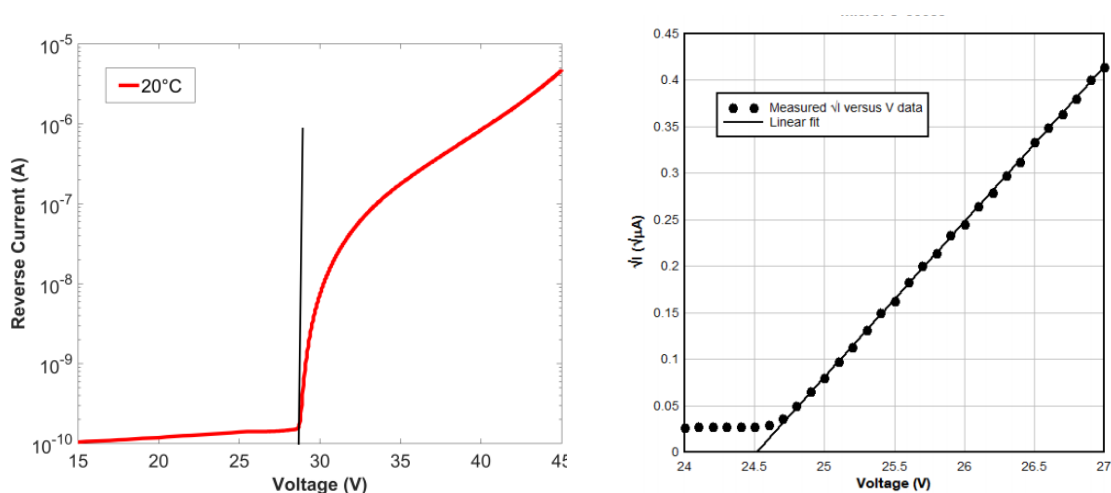

Figure 4.10: On the left, reverse output current vs supply voltage of a SiPM. On the right, determination of the exact value of breakdown voltage.

The breakdown voltage value depends on the electric field inside the SiPM, which in turns, depends on the doping profiles of the SiPM. SiPM sensors are operated at a bias point that is typically a few Volts higher than the V_{br}. The difference between the V_{br} and the bias point is referred to as the overvoltage (ΔV).

There is a positive shift of the breakdown voltage with the temperature increase due to variations in carrier mobility and ionization rates. Fig. 4.11 shows this phenomenon for temperatures between -40 °C and 40 °C. This variation of the breakdown as a function of temperature is linear, as a first approximation.
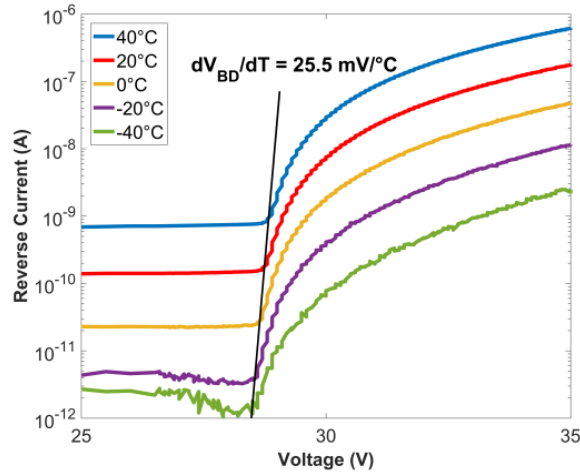
Figure 4.11: Reverse I-V curves at different temperatures. The breakdown voltage has a positive shift by increasing the temperature.

Gain

The gain of a SiPM is defined as the amount of charge created for each detected photon, and is a function of overvoltage and microcell size, as is shown in Fig. 4.12.

Each microcell in the SiPM generates a highly uniform and quantized amount of charge every time an avalanche is generated by an absorbed photon in the active volume. The gain of a microcell (and hence the sensor) is then defined as the ratio of the charge from an activated microcell to the charge on an electron. The gain can be calculated from the overvoltage ΔV, the microcell capacitance C, and the electron charge q.

$$G = \frac{C \cdot \Delta V}{q} \tag{4.5}$$

The gain of a single APD cell in a SiPM increases linearly with the overvoltage, as opposed to standard APDs, in which the gain is exponentially related to the voltage. The gain is independent of the temperature if the overvoltage, ΔV, is constant, although the breakdown voltage, V_{br}, is dependent on temperature. This means that when the bias voltage is constant and the temperature changes, the gain will also change due to a shift in the breakdown voltage.
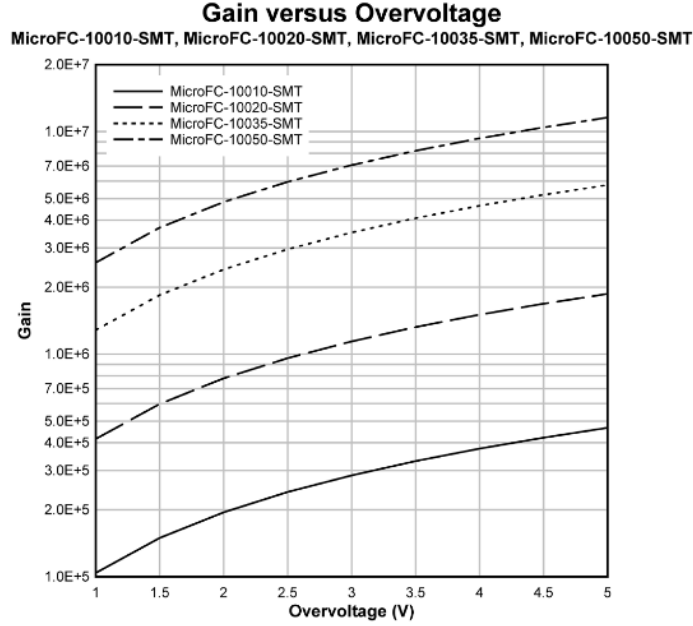
Gain versus Overvoltage

MicroFC-10010-SMT, MicroFC-10020-SMT, MicroFC-10035-SMT, MicroFC-10050-SMT

Figure 4.12: Gain as a function of overvoltage for different microcell size SiPMs (10 μm, 20 μm, 35 μm and 50 μm) [29]

Photon detection efficiency

An important parameter of a photodetector is the efficiency at which photons of a given wavelength can be detected. For a SiPM the Photon Detection efficiency (PDE) can be factorised in three quantities [28]:

$$PDE(\lambda, V) = \eta(\lambda) \cdot \varepsilon(V) \cdot FF \tag{4.6}$$

where $\eta(\lambda)$ is the quantum efficiency of silicon, i.e., the probability that an electron-hole pair is generated, $\varepsilon(V)$ is the avalanche initiation probability and FF is the geometrical fill factor, i.e. the ratio of the active to the total area of the device, as a result of the dead space between the microcells.

Because the FF is constant for a given SiPM, and the quantum efficiency of the device is constant for a given scintillator or a given light sources wavelength, the PDE of a single device depends only on $\varepsilon(V)$ and, in consequence, is a function of the SiPM bias voltage.
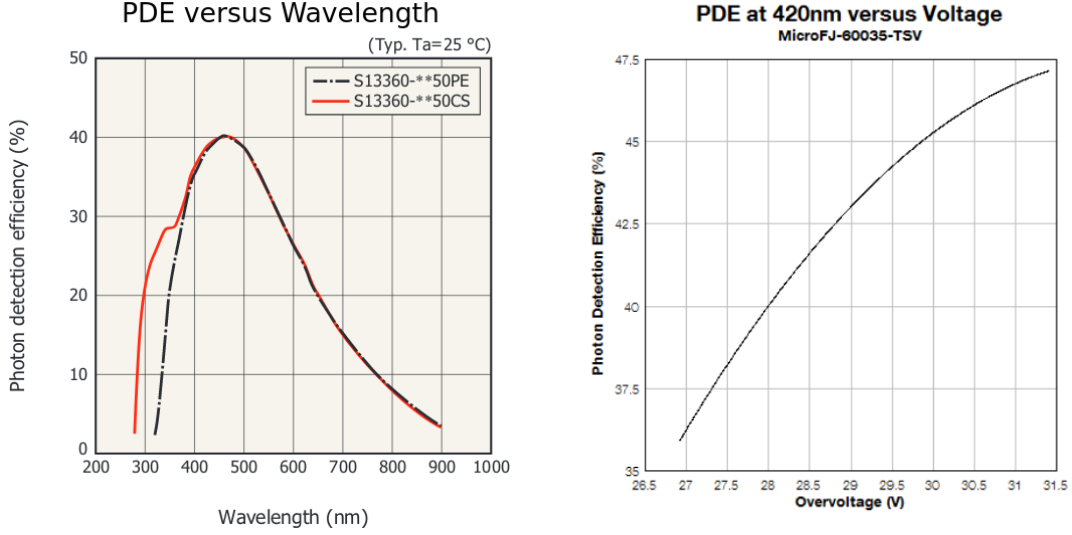
Figure 4.13: On the left, PDE as a function of wavelength for a 6×6mm 50 μm microcell SiPM [30]. On the right, PDE as a function of overvoltage for a 6×6mm, 35 μm microcell SiPM [27]

Dark count Rate

The primary source of dark noise in SiPM are the charge carriers that are generated, either thermally or by quantum tunneling, within the depletion region, and which subsequently enter the Geiger multiplication area and trigger avalanches.

Different physical phenomena are responsible for primary dark counts generation in SiPMs. Thermal generation of carriers by states in the bandgap can be modeled using Shockley-Read-Hall (SRH) statistics [31]. In depleted silicon, the generation rate can be approximated by:

$$G = \frac{n_i}{2 \cdot \cosh(\frac{E_0 - E_t}{kt})} N_t \sigma v_{th} = \frac{n_i}{\tau_{g0}} \tag{4.7}$$

in which n_i is the intrinsic carrier concentration in silicon, E_0 is the Fermi level of intrinsic material, E_t is the energy level of the trap, N_t is the trapping center concentration, σ is the capture cross section of the trap for electron or holes and v_{th} is the thermal velocity of electrons or holes [31]. As a simplifying assumption, in Eq. 4.7 σ and v_{th} are assumed equal for electrons and holes. τ_{g0} is called the generation lifetime. The reciprocal of τ_{g0} is the rate at which eh pairs are generated in the depleted silicon. It is proportional to the concentration of the trap and depends on its energy difference

from E_0.

The generation of electron-hole pairs depends on the bias applied to the SiPM. When the overvoltage is increased, the magnitude of the electric field in the high-field region gets higher, increasing the tunneling to and from the trap and, thus, the generation rate. Fig. 4.14 shows that the measured DCR of a SiPM increases linearly with increasing overvoltage.
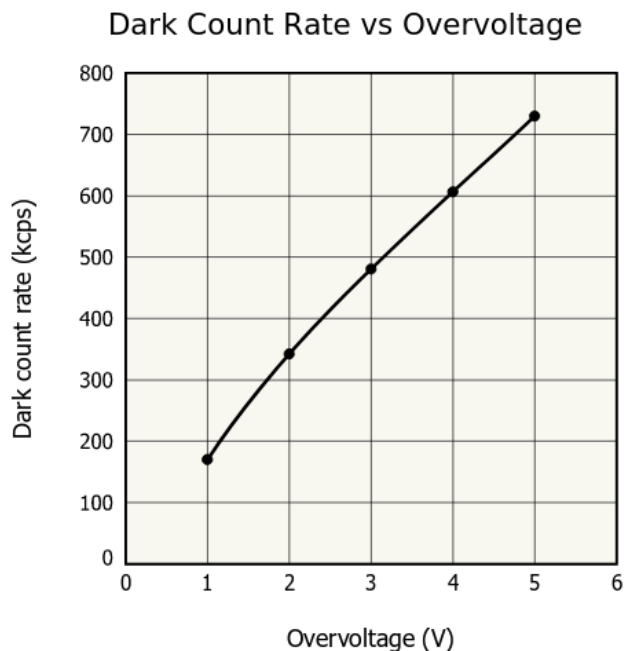

Figure 4.14: Dark count rate as a function of overvoltage for a 3×3 mm, 50 μm microcell SiPM [30]

Different noise sources feature different dependence on temperature. Fig. 4.15 shows, on a qualitative level, a plot of the SiPM DCR as a function of temperature, distinguishing between the three main contributions: diffusion, SRH generation and direct tunneling. It should be noted that the generation processes show an exponential dependence on T^{-1} such that DCR dependence on temperature shows the following trend:

$$DCR(T) \sim \exp(-\frac{E_a}{kT}) \tag{4.8}$$

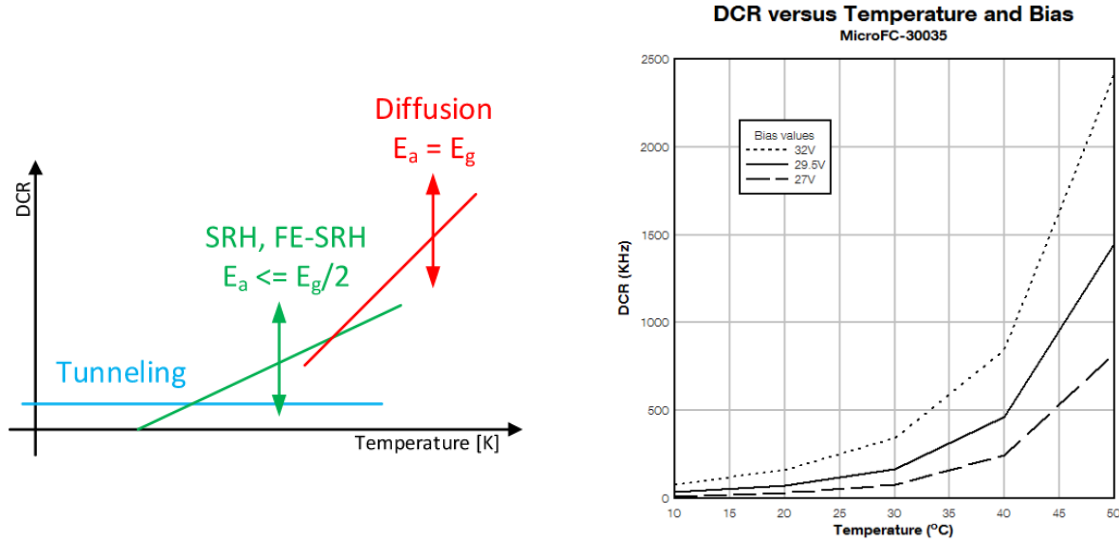in which E_a is the activation energy of the specific generation process.

Figure 4.15: On the left, qualitative plot of the SiPM DCR as a function of temperature, distinguishing on the tree main contribution. On the right, DCR of a SiPM for different bias values as a function of temperature [29].

Optical Crosstalk

The optical cross-talk in SiPMs are false pulses that are produced by optical photons emitted during an avalanche discharge within a single APD cell. These photons can trigger another Geiger discharge in the same or a neighboring APD cell. The corresponding signal cannot be separated from a signal induced by an initial photon. This cross-talk limits the photon-counting resolution of SiPM devices as it is impossible to determine the exact number of photon-induced pixel-breakdowns. The cross-talk probability is thus an important characteristic of a SiPM and should be as small as possible.

Optical cross-talk can manifest itself in three different ways [28]:

- *direct* − when the emitted photon generates a carrier in the active region of a neighboring APD cell, thus producing a second avalanche in coincidence with the first one;

- *delayed* − when the emitted photon is absorbed by the non-depleted region beneath the same or a neighboring APD cell, thus generating a carrier capable of reaching the active region by diffusion. The diffusion process is relatively slow, so the second avalanche can be delayed in time with respect to the first one;

- *external* − when the emitted photon tries to escape from the device but is reflected by structures placed on top of the device, for example, a scintillator.

The number of optical cross-talk events mainly depends on the APDs cell size, the distance between the high-field regions, and the gain.

The cross-talk probability as a function of gain for three SiPMs with different APD cell sizes is presented in Fig. 4.16. Cross-talk probability is measured as a ratio between the dark rate above the 1.5 photoelectron threshold, and the 0.5 photoelectron threshold [32]. It is worth noting that devices with smaller APD cell sizes have larger cross-talk probabilities when compared to devices with larger APD cells. This is because, in the case of the larger cells, photons have to travel a longer average distance before reaching a neighboring APD cell where they can cause a second avalanche.In modern SiPMs, trenches between the cells are inserted to provide electrical and partial optical isolation.
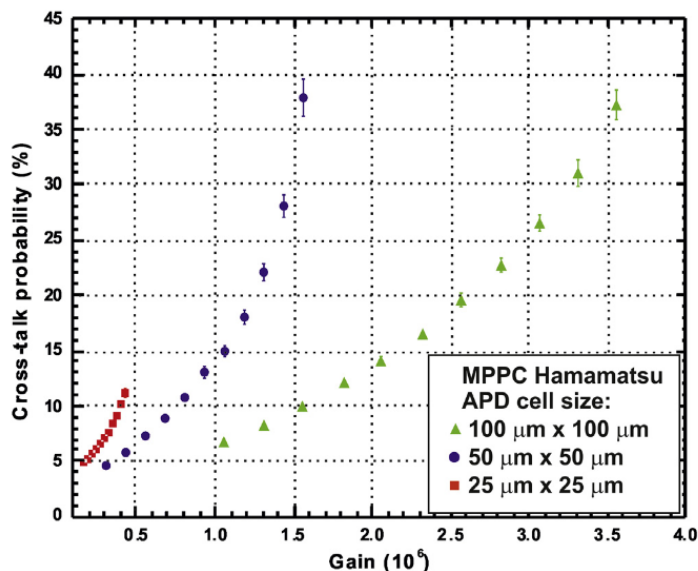

Figure 4.16: Cross-talk probability as a funciton of SiPM gain for three different sensor types. [32]

Afterpulse

During breakdown, carriers can become trapped in defects in the silicon. After a delay of up to several ns, the trapped carriers are released, potentially initiating an avalanche and creating an afterpulse in the same microcell. Afterpulses with short delay that occur

during the recovery time of the microcell tend to have negligible impact as the microcell is not fully charged. However, longer delay afterpulses can impact measurements with the SiPM if the rate is high. Fig. 4.17 shows the behaviour of a SiPM with impurities presenting different trap times. Note that if the APD cells voltage has not reached its nominal value when carriers are released, the charge produced in the avalanche will be lower than for the nominal avalanches. Only if the delay is longer than the APD cells effective recovery time a standard (full gain) avalanche signal will be triggered.
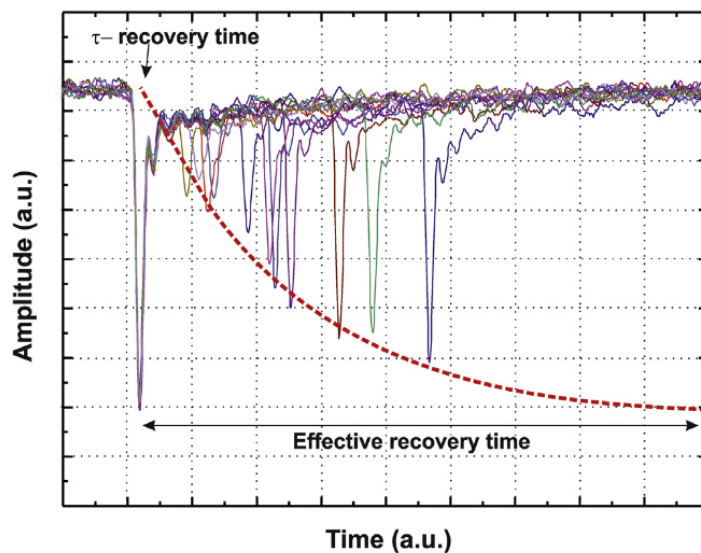

Figure 4.17: Example of afterpulses with different delays.

Dynamic range and linearity

The dynamic range of SiPMs is limited by the finite number of their cells. SiPMs provide a good linearity as long as the number of impinging photons is lower than the number of cells, $N_{photons} \ll N_{cells}$. When this condition is not met, the SiPM response is non-linear. This behaviour can be described using Poisson distribution [25]. The probability to have n-interactions in a cell i, $P_i(n)$, can be expressed assuming that the photons are evenly distributed across all the microcells, as:

$$P_i(n) = \frac{e^{-\frac{N_{ph} \cdot PDE}{N_{cells}}} \left(\frac{N_{ph} \cdot PDE}{N_{cells}}\right)^n}{n!} \tag{4.9}$$

where N_{ph} is the number of impinging photons, PDE is the SiPM photon detection efficiency, N_{cells} is the number of the SiPm cells, and n is the number of interactions. The number of fired cells, N_{fired} is given by:

$$N_{fired} = N_{cells} \cdot (1 - P_i(0)) = N_{cells} \cdot (1 - e^{-\frac{N_{ph}PDE}{N_{cells}}}) \qquad (4.10)$$

where $P_i(0)$ is the probability to have zero interaction. Fig. 4.18 shows the number of fired cells as a function of the number of photoelectrons that have the potential to be detected by the SiPM. It is clearly visible that the sensor has a linear response at lower photon fluxes, but as the number of incident photons increases the sensor begins saturating.
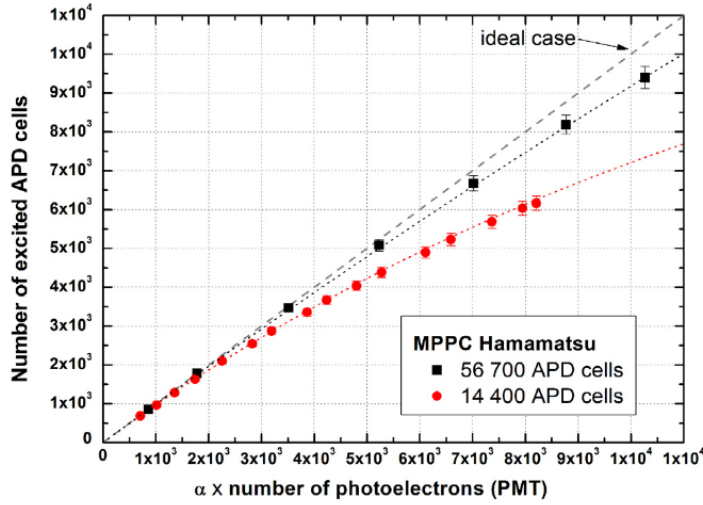

Figure 4.18: Number of APD cells fired vs the number of photoelectrons detected by a PMT, which is proportional to the number of total events that have the potential to be detected by the SiPM. [25]

4.3   SiPM readout electronics

When a high timing performance is important in a detector employing SiPM, conventional amplifier techniques for photomultiplier tubes, photodiodes, or avalanche photodiodes are not always applicable, due to the electronic characteristics of these types of light sensors [33].

In particular, SiPMs have a high terminal capacitance (> 300 pF for a 3×3 mm^2 device),

consisting of the sum of all cells capacitance and the internal interconnect capacitance. Since this is much larger than the 3-10 pF anode capacitance of a typical PMT, a dedicated preamplifier is needed in order to not deteriorate the rise time and signal-to-noise ratio of the SiPM signal.

Another characteristic of SiPMs is the dependence of the output impedance on the number of microcells being fired, in contrast with the almost ideal current source behavior of PMTs.

The equivalent circuit of a SiPM is shown in Fig. 4.19, resulting from a large number of parallel-connected Geiger-mode photodiodes. The figure highlights the case in which only one microcell at a time fires. When several photons hit a SiPM at the same time, some of the microcells will discharge, while other cells remain inactive. Each cell has its own quench resistor, diode resistance, and inherent parasitic capacitances. The total impedance of a cell is very different depending on its state (inactive or discharging). Since all cells are connected in parallel, it follows that the SiPM output impedance varies with the amount of light incident on the sensor[33].
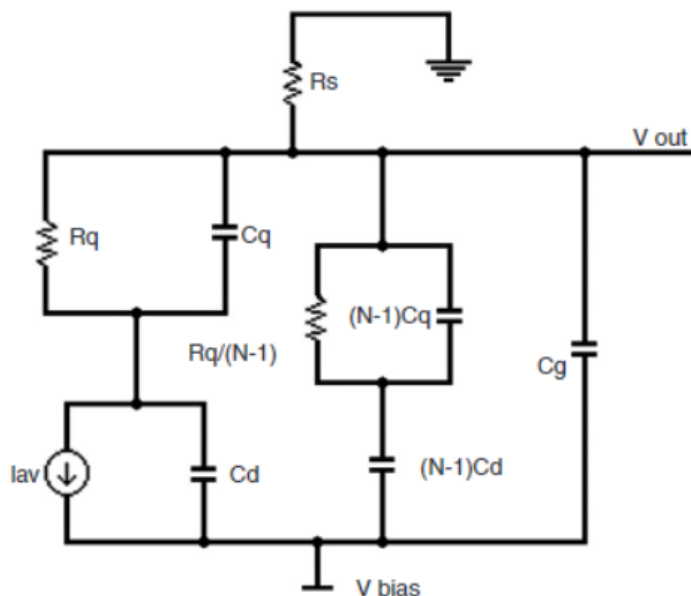

Figure 4.19: Equivalent electric model of a SiPM with a single cell firing[34].

The model of a single microcell, which is biased a few Volts above the breakdown voltage V_{br}, includes the diode capacitance C_d, the quenching resistor R_q, a small parasitic capacitance C_q (in parallel to R_q), and a current source, which models the total charge

delivered by the microcell during the Geiger discharge caused by an event. A further small capacitance C_p must be also considered in parallel to each microcell, to account for the parasitics between the substrate of the device and the contact of the quenching resistor [34]. R_s represents the input resistance of the front-end electronics, usually very small (few tens of Ohms), whereas C_g models the lumped contributions of the parasitics C_p.

If a SiPM is connected to an amplifier with finite input impedance, its varying output impedance may give rise to non-linear behavior. Studies have shown that the linearity of the overall response improved with decreasing input impedance of the amplifier. Together with the already mentioned effect of the high SiPM capacitance on the time response, one can conclude that the lower the preamplifier input impedance, the faster the timing response and the better the linearity of the signal will be.

4.3.1   Basic readout methods

A basic read-out can be arranged by adding a shunt resistor R_s to ground, see Fig. 4.20. R_s is a low ohmic resistor (typically 50 Ω, to match coaxial cables) which converts the current into a proportional voltage. To provide gain, an operational amplifier is commonly employed. However, if R_s is kept to a value of, for example, 10 Ω or smaller to address the concerns mentioned above, the signal voltage generated across R will be very small, necessitating a high-gain amplifier. This degrades the signal to noise ratio of the first amplifier stage. Due to gain-bandwidth limitations, high-speed amplifiers typically have a relatively low gain of about 20 dB or less, requiring several of these amplifiers to be placed in cascade, increasing power consumption as well. This also leads to a decrease of the signal slope at the onset, which may result in worsening of the timing resolution.
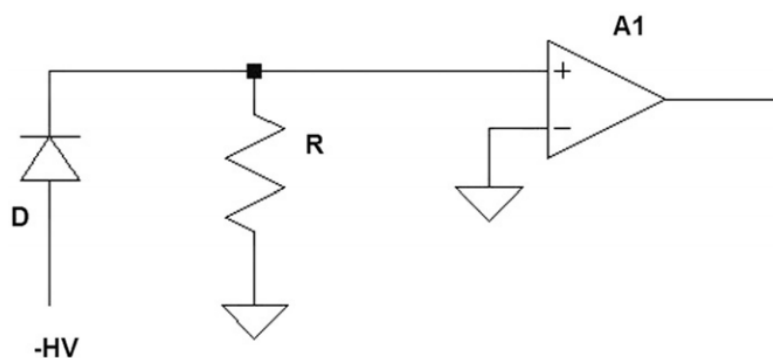

Figure 4.20: Voltage amplifier with shunt resistor.

Another option is using a transimpedance amplifier, that is an active current-to-voltage converter. It consists of an op-amp with a resistor R_f in the negative feedback path. The non-inverting input is connected to ground, see fig. 4.21.
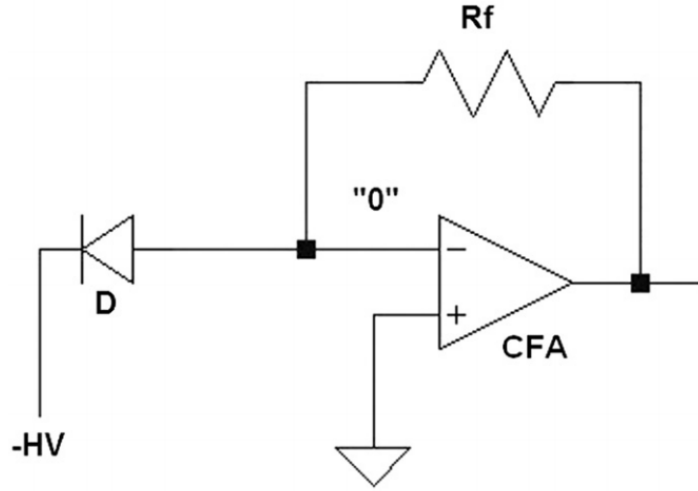

Figure 4.21: Transimpedance amplifier.

Using feedback, the effective input impedance $R_e f f$ of the entire circuit is reduced to much lower values following the equation:

$$R_{eff} = \frac{R_{int}}{Z_0 \beta + 1} \tag{4.11}$$

where Z_0 is the open-loop transimpedance gain and β the ratio of R_{int} and feedback resistor R_f. Initial tests using an AD8000 Current Feedback Amplifier from Analog Devices and an R_f of 470 Ω have shown that the rise times obtained with such a circuit in combination with 3 mm $\times$ 3 mm SiPMs illuminated with a picosecond laser are longer than with a voltage amplifier with a small 50 Ω shunt resistor.

4.3.2   Common base amplifier

A common-base amplifier without feedback is a good candidate to overcome the problems described in the previous sections. 4.22 shows the basic scheme of a common-base amplifier. In this circuit the emitter terminal of the npn transistor serves as the input, the collector as the output, and the base has a DC biasing voltage but is decoupled to ground by means of a capacitor, in order to decrease the input impedance for high signal
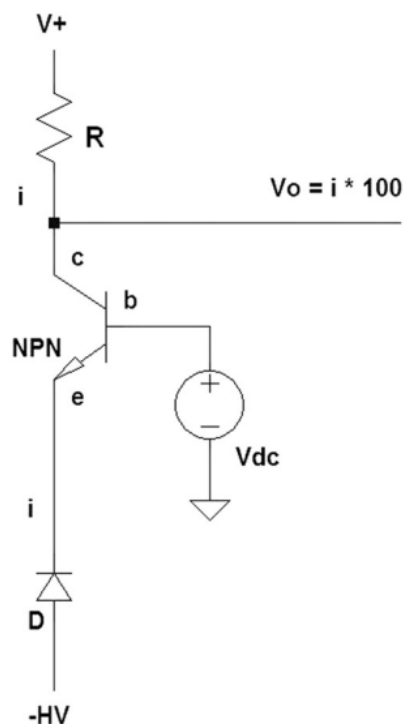
Figure 4.22: Basic circuit of a common-base amplifier. The intrinsically low input impedance of the emitter isolates the detector capacitance from the remainder of the circuit, so that it does not affect the amplifier transfer function.

frequencies. By design, the input impedance is very small without using any feedback, ensuring a negligible effect of the detector capacitance on the overall time response. The input signal current i flows from the emitter to the collector of the transistor and generates a voltage difference over the collector resistor R. Since the collector capacitance is very small, this resistor can be relatively large, enabling high transimpedance gain without compromising speed.

Compared to the shunt resistor method, the common base amplifier can convert the signal current to a signal voltage that is at least an order of magnitude higher (using R~100 Ω). Furthermore in the case of the shunt resistor method, the required fast time response dictates the choice of the shunt resistor since the response is a function of the detector capacitance and the shunt resistor value. In the case of the common-base amplifier the resistor value can be chosen more freely since the detector capacitance is isolated from this resistor. The high gain results in less stringent noise demands on

consecutive amplifiers and eliminates the need for multiple consecutive amplifying stages, thereby avoiding the increased curvature of the output pulse.

Chapter 5

Tile prototypes

In this chapter we present the prototypes assembled and the tests taken in order demonstrate the feasibility of reaching the required time resolution with a square tile of 225 cm^2, and the steps taken in order to develop a definitive tile design for the detector.

There have been two opportunities to put the prototypes under test. A first test beam was held at the T10 beamline on the Super Proton Synchrotron (SPS) at CERN in October 2018. The data collected during this test is used in this thesis to compare and optimize various algorithms for obtaining the arrival time measurement of events from the tile signal, with the purpose of obtaining the best time resolution possible. A second test beam was held at the DESY electron synchrotron in May 2019 facility in order to obtain a time resolution estimation on an improved design of the tile assembled in the INFN laboratories of Bologna.

5.1   Tile prototypes

Seven prototypes were assembled between 2018 and the first half of 2019. The scintillator tiles were made of EJ-200 plastic scintillator, produced by Eljen Technology. The key properties of this material are listed in Table 5.1: its short rise and decay time, as well as its high light output, are of great importance for the application in an high time resolution detector.

The first four prototypes, from now on referred as *Tiles A, B, C* and *D*, were assembled with the objective of testing different coatings and scintillator thickness. Their area is 10×10 cm^2, with a thickness of 8 mm for tiles A, B and C, and 10 mm for tile D. All tiles are equipped with 2 SiPM of the same model, Hamamatsu S14160, placed on the corners symmetrically with respect to the diagonal. In Tab. 5.2 the key features of the SiPM models employed are listed.

Properties	Eljen EJ-200
Light Output (% Anthracene)	64
Scintillation Efficiency (photons/1 MeV e-)	10000
Wavelength of Maximum Emission (nm)	425
Light Attenuation Length (cm)	380
Rise Time (ns)	0.9
Decay Time (ns)	2.1
Polymer Base	Polyvinyltoluene
Refractive Index	1.58

Table 5.1: Eljen Tehcnology EJ-200 scintillator properties [35]

SiPM model		Size (mm^2)	Cell Pitch (μm)	n of pixels	Fill Factor (%)	Peak Sensitivity Wavelength (nm)	PDE (%)	Refractive Index	Breakdown Voltage (V)
S13360	3050 PE	3×3	50	3600	74	450	40	1.55	53 ± 5
	3075 PE	3×3	75	1600	80		50		
S14160	4050 HS	4×4	50	6331	74	450	50	1.57	38
	6050 HS	6×6	50	14331					

Table 5.2: Hamamatsu SiPM models characteristics and operating parameters [30, 36].

Tile A was coated with black paint, and it served as a reference for the other tiles and to tune the simulation in the case where no photons are reflected inside the scintillator. Tile B was painted with titanium oxide paint, while Tile C and D were wrapped in aluminized mylar to enhance light collection. The performance of these coating types is well documented [37, 38], and aluminized mylar is often preferred, as it accomplishes a better light collection in organic scintillators. However, titanium dioxide paint may be of easier application to a large production number of tiles with an industrial process.
Tile F and *Tile G* were assembled with the objective of testing various models of SiPMs produced by Hamamatsu, with varying area and cell pitch size. The scintillator size is 15×15 cm ^{2}, with 1 cm thickness. On Tile F are placed two pairs of SiPM models with an equal cell pitch of 50 μm, but a varying window size, 4×4 and 6×6 mm^2, while on Tile G two pairs of SiPM have the same window size of 3×3 mm^2 but a cell pitch of 50 μm and 75 μm. The main performance parameters of these SiPM models are summarized in Tab. 5.2 again. Moreover, the tiles were wrapped in teflon tape (Fig. 5.1). The SiPM are placed on the beveled tile corner, pressed onto the scintillator surface by tape as well.
Tiles A - G underwent a test beam at the T10 beamline on the Super Proton Syn-
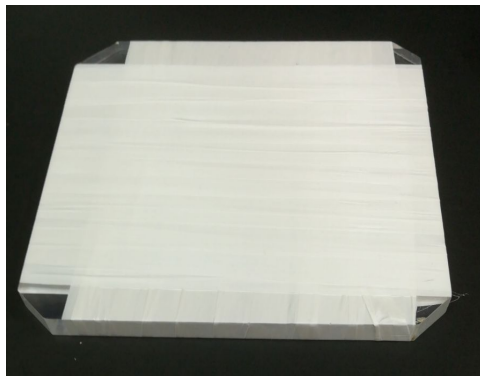
Figure 5.1: Scintillator tile wrapped in teflon tape.

chrotron (SPS) at CERN in October 2018. Tiles A, B, C, D were only briefly exposed to the beam, and their performance qualitatively evaluated online. Only tiles F and G underwent the complete test, since for the final tile design we are considering a scintillator of such dimensions. As expected, among the 10×10 cm^2 tiles, the ones that produced signal with the highest amplitude were C and D, which were wrapped in aluminized mylar. Tile B, coated in titanium oxide paint, was slightly less performing, but its output signal was still acceptable to be used in the detector. Tile A, whose black paint prevented photons from being reflected against the scintillator surface, could collect only a few photons in the SiPM window, and their output signal could not be distinguished from electromagnetic and dark noise. Regarding the scintillator thickness, when comparing output signals between Tile C, that is 8 mm thick, and Tile D, 10 mm, the measured amplitude increase of the latter was not significant. Therefore, the choice between the two options will be mostly driven by the scintillator production availability and cost.
The data collected for Tile F and Tile G is used in this thesis to compare and optimize various algorithms for obtaining the arrival time measurement of events from the tile signal, with the purpose of obtaining the best time resolution possible.
The last tile prototype, named *Tile H*, was assembled in April 2019. Based on the results obtained in the previous test beam, the purpose of this prototype was to evaluate the tile response of a tile with 4 identical SiPM on corners in order to provide a reference for future designs, and to quantify how glueing the SiPM with optical cement can improve the light collection. It was used the same model of SiPM used for Tiles A - F, the Hamamatsu S14160 (Tab. 5.2).

This tile, shown in Fig. 5.2, was assembled in the INFN Bologna Laboratories. In the next paragraph the experimental setup and the methods employed to characterize
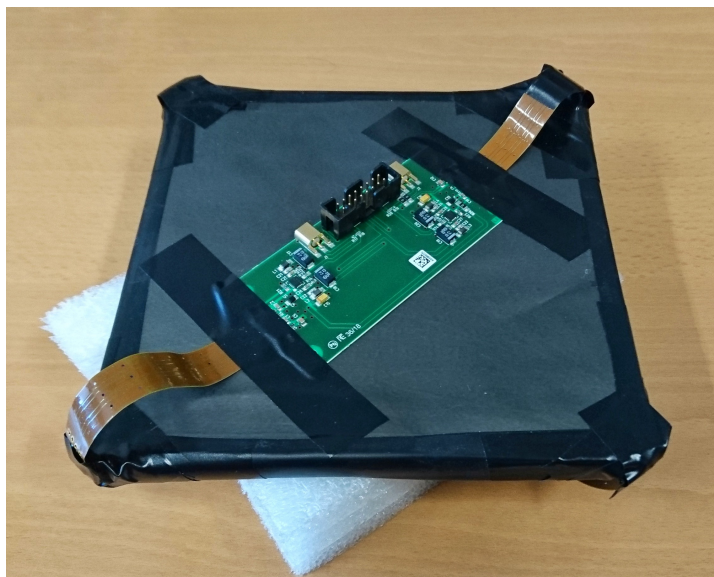
Figure 5.2: Tile H, assembled in the INFN Laboratories of Bologna.

and determine the SiPMs more suitable for mounting on the tile are described.
The scintillator used is the EJ200 like Tile F and G, but coated in several layers of titanium oxide paint. The selected SiPMs were glued to the scintillator using EJ500, an epoxy adhesive that is transparent to the scintillator light and has a refractive index very close to the scintillator material and SiPM window.

Tile name	Size (cm^3)	N of SiPM	SiPM Model	Coating
A	$10 \times 10 \times 0.8$	2	S14160 4050HS	Black paint
B	$10 \times 10 \times 0.8$	2	S14160 4050HS	titanium oxide paint
C	$10 \times 10 \times 0.8$	2	S14160 4050HS	Aluminized mylar
D	$10 \times 10 \times 1$	2	S14160 4050HS	Aluminized mylar
F	$15 \times 15 \times 1$	2 / 2	S14160 4050HS / S13360 6050CS	Teflon
G	$15 \times 15 \times 1$	2 / 2	S13360 3050PE / S13360 3075PE	Teflon
H	$15 \times 15 \times 1$	4	S14160 4050HS	Titanium oxide paint

Table 5.3: A summary of the characteristics of prototype tiles.

5.1.1 SiPM characterization for tile H

Four pairs of SiPM, already connected to the bias and amplifier circuit were available in the laboratories (Fig. 5.3). In order to chose which SiPM to mount on the tile, they were characterized for gain and dark count rate.
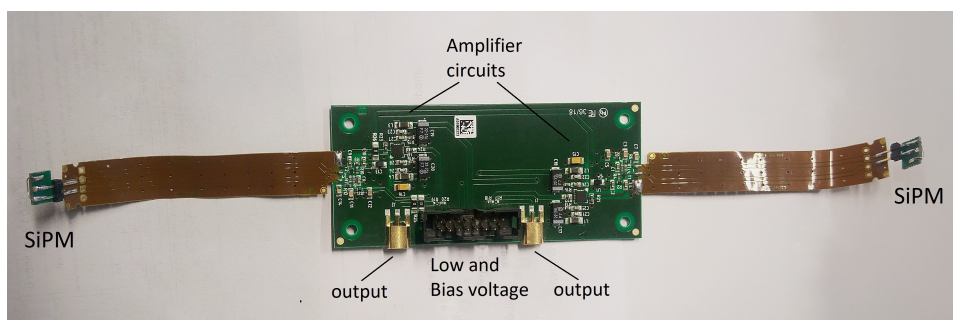

Figure 5.3: SiPMs muounted on the amplifier and bias voltage circuit.

The hardware setup used for the dark characterization is shown in Fig. 5.4. It consists of a light-tight black box containing the SiPM under test with its amplifier board and an oscilloscope located outside. Supply voltage for SiPM and the amplifier circuit, as well as lemo cables enter the box through a small hole sealed with black tape. The used oscilloscope has a highbandwidth (1 GHz) and 10 GS/s.

A digital low pass filter is applied in order to remove electromagnetic noise with a frequency higher than 800 MHz, such as mobile phones networks and Wi-Fi, that is picked up in the cables about 10 cm long, connecting the SiPMs to the amplifier. Unfortunately it was not possible to remove the electromagnetic noise at lower frequencies as the additional filter would have affected the fast component of the signal as well. Due to this remaining noise with an amplitude of about 5 mV, it was preferred to register the peak amplitude of signals instead of performing a charge integration on the whole waveform. Fig. 5.5 show the amplitude distribution, the peak corresponding to the baseline is clearly visible on the left, and the peak corresponding to a single fired SiPM cell on the right. The mean amplitude value for a single cell fired is determined at bias voltages from 40.5 to 43 V, with a step size of 0.5 V. The baseline-subtracted amplitude for a single cell provides a direct measurement of the voltage gain. This method only allows to determine the absolute gain of the SiPM and amplifier together, but it is nevertheless sufficient for the purpose of evaluating the available devices and identifying the best performers.
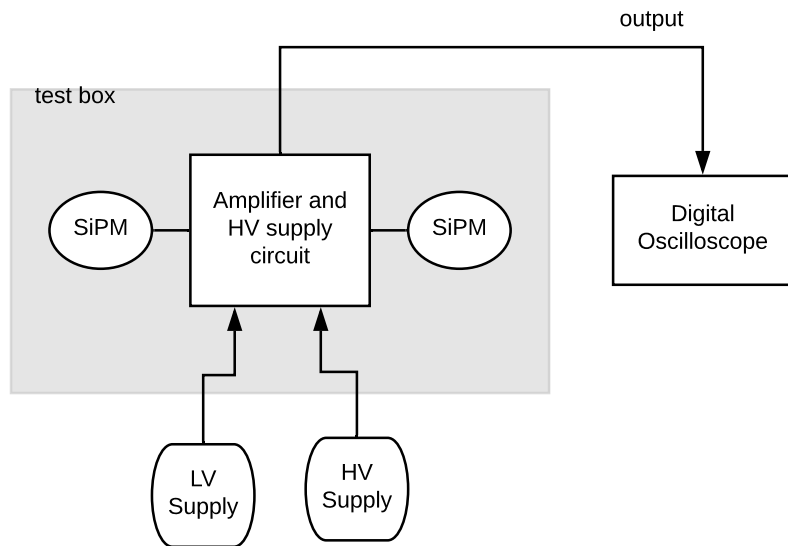
Figure 5.4: Experimental setup scheme for SiPM gain and dark count rate measurements.
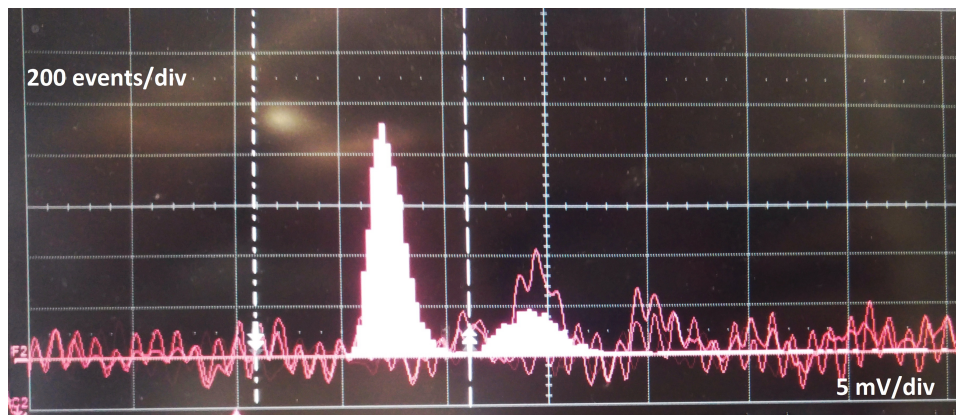

Figure 5.5: Peak amplitude histogram of SiPM pairs amplified output. The peak on the left corresponds to the baseline, while the one on the right is the SiPM output of a single cell fired.

The Dark Count Rate is determined as the ratio of the number of entries in the amplitude histogram in the peak corresponding to a single cell fired and a fixed total number of events. This result is divided by the SiPM area. Again, the DCR is measured

for bias voltage from 40.5 to 43 V and the values fitted with a straight line.
An example of the obtained values fitting is shown in Fig. 5.6, while the overall results are reported in Tab. 5.4. The pairs chosen to be mounted on the prototype tile are number 222 and 225, as their SiPMs have an overall higher gain.
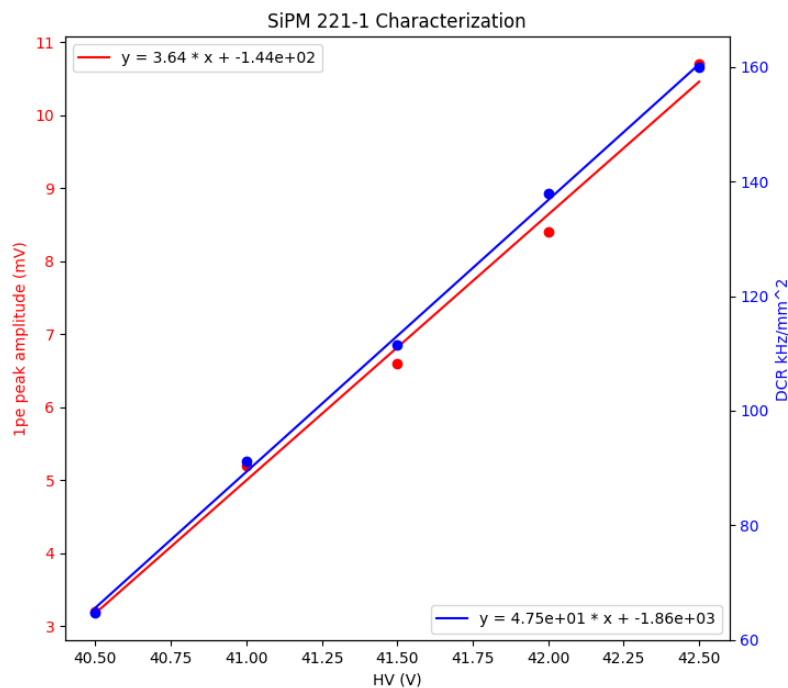

Figure 5.6: Example of SiPM characterization for gain (in red) and dark count rate (blue).

5.2 Test beam experimental setup

5.2.1 2018 CERN T10 test beam

The purpose of the 2018 CERN test was to compare the performance of tiles and SiPMs with different building characteristics. The test has been performed on the T10 beamline, located in the PS complex. The beam delivered to the T10 beamline is obtained from the interaction of the primary 24 GeV protons of the PS accelerator with a fixed target; different targets can be chosen in order to maximize the production of secondary electrons or hadrons. In this case, a secondary beam composed of μ and π was selected, as these

SiPM ID	Gain (mV/V)	DCR (kHz/Vmm^2)
222-1	3.64	47.4
222-2	3.84	59.1
223-1	3.7	43.7
223-2	3.16	112.0
225-1	3.56	76.3
225-2	3.58	50.3
228-1	3.22	32.6
228-2	3.04	63.7

Table 5.4: Gain and Dark Count Rate values of the available SiPM pairs.

are the particles of interest for the muon detector. The momentum of the extracted beam was 6 GeV/c.

The experimental setup on the T10 beamline is presented in Fig. 5.7, 5.8.
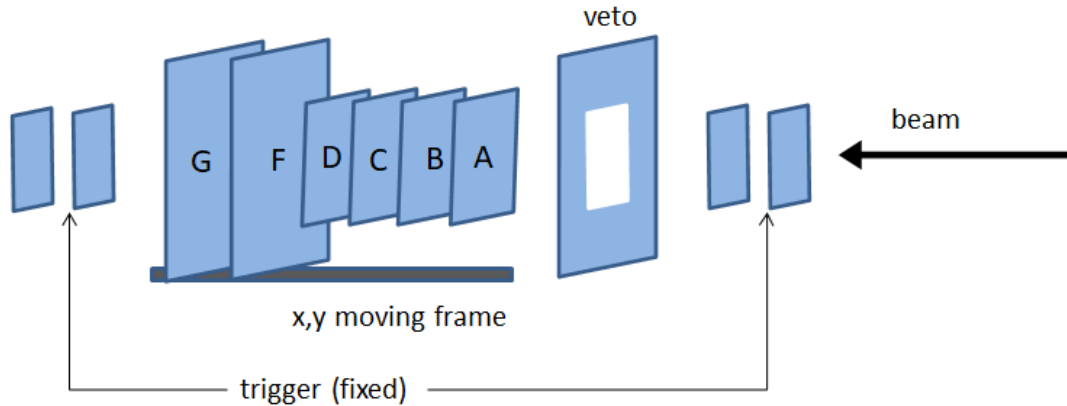

Figure 5.7: Experimental setup scheme at CERN T10 test beam (not in scale).

All tiles under test are aligned normal to the beam, in order to test them simultaneously. The frame they are placed on can be moved so that the beam can pass through various points of the tiles. A schematic of the beam position is shown in fig. 5.9. The trigger consists of the coincidence signal of four small area scintillator tiles (20 ×20 mm^2), two placed before and two after the tiles under test. Finally, a multiple particle veto allows to reject most events containing a second particle. The digitization was carried
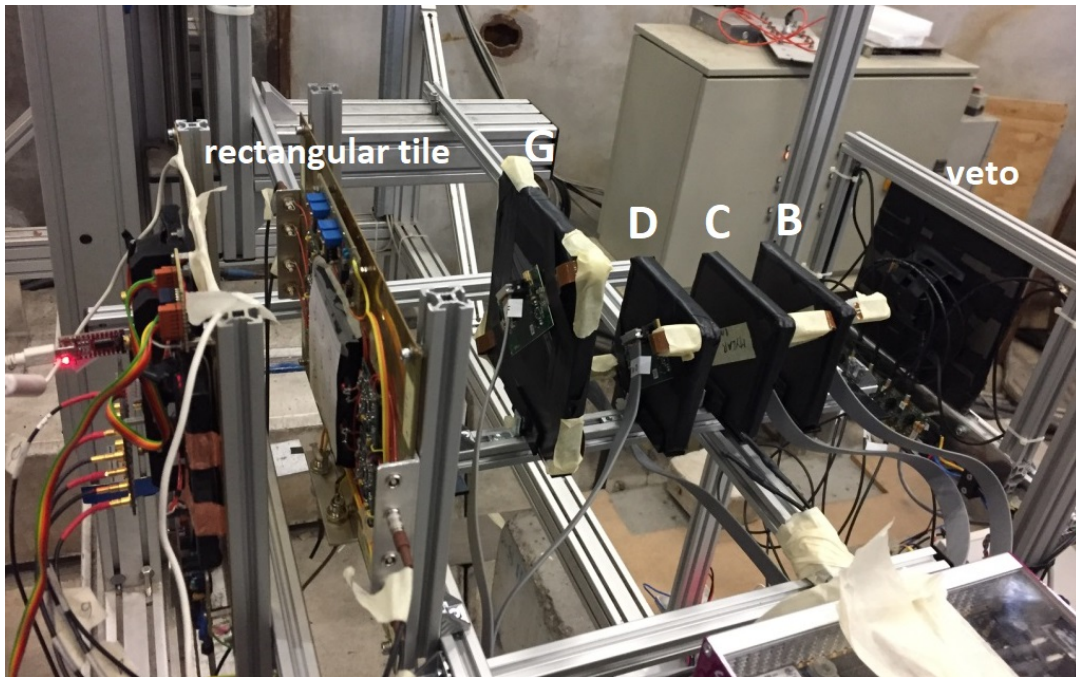
Figure 5.8: Picture of the experimental setup.

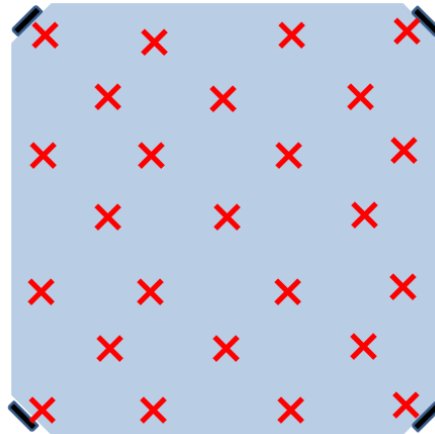out by the SAMPIC Waveform TDC, operated at a 3.2 GHz sampling rate.

Figure 5.9: Scheme of the tiles tested points at cern T10 test beam.

5.2.2   2019 DESY test beam

Tile H was tested at the DESY II Test Beam Facility. The test beams are generated by a double conversion: initially bremsstrahlung photons are generated by a carbon fiber target positioned in the DESY II beam orbit. These photons hit the secondary target generating electron/positron pairs. Depending on the polarity and strength of the magnetic field of the following dipole magnet, the test beam particles reaching the test beam areas are electrons or positrons with a certain momentum.

For this test an electron beam with 5.4 GeV/c energy was selected. Since this test beam slot was shared among multiple groups, only a short measurement campaign with a small setup was possible. Electrons were delivered to the tile at a rate of about 500 Hz, on various points of the tile. Fig. 5.10 shows the points coordinates. The trigger consists of two 20×20 mm^2 scintillator tiles placed behind Tile H, as shown in Fig. 5.11. The digitization is carried out by SAMPIC Waveform TDC, as in the previous test beam.

Figure 5.10: Scheme of beam positions on Tile H. The data collected with the beam passing through the points marked with a green cross are used for algorithm optimization. The points marked in purple are situated near the SiPM that resulted non functioning during tests, and are excluded when computing the tile timing resolution (see next chapter).
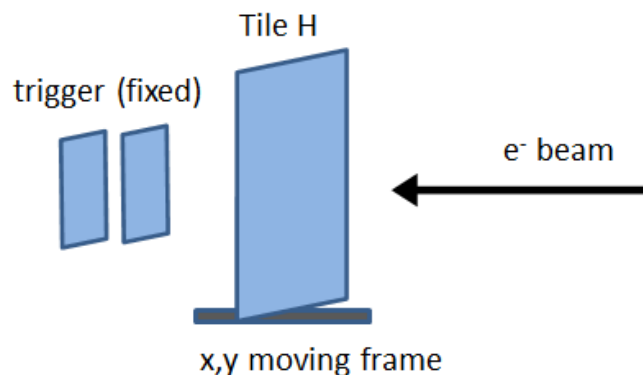
Figure 5.11: Experimental setup scheme at DESY test beam.

5.3   Tile timing resolution

The tile timing resolution is computed as the root mean square of the arrival times distribution. As a large sample of events is collected, this distribution can be approximated to a Gaussian. As the beam crosses the trigger, data acquisition is started and the waveform produced by every SiPM is recorded. The individual signals can be summed to evaluate the tile response as a whole. Since the SiPMs on Tile F and Tile G have different characteristics, their signals are weighted by imposing the peak amplitude to be equal for every SiPMs, on average, when a particle is crossing in the tile center.
From the recorded waveforms, either of the single SiPM or summed, a timestamp of the arrival time of the particle must be extracted. In the next paragraphs a few algorithms explored for this task are described.

5.4   Timing algorithms

5.4.1   Constant Fraction Discriminator (CFD)

The constant fraction method allows to implement accurate time measurement regardless of the pulse height, thus compensating for time walk that affects simpler methods such as using a fixed threshold. The idea is to create a variable threshold that tracks the signal always at a certain fraction of its maximum amplitude. With this technique, time walk due to rise time and amplitude variations is corrected. Fig. 5.12 shows an event signal

and the timestamp determination with a CFD at 20%. The signal peak is determined as the highest amplitude value, while the baseline is determined as the interpolation of the first ten points with a horizontal line. The signal waveform is linearly interpolated. This algorithm is quite effective as it allows to compensate for time walk, and it is simple enough to be implemented in an FPGA in the planned front end electronics of the SHiP experiment if needed.
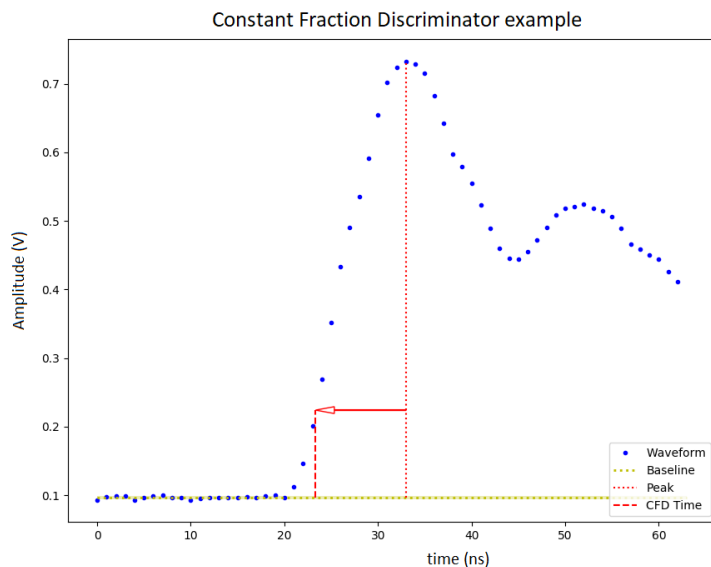

Figure 5.12: Constant Fraction Discriminator on example event. The treshold is set at 20% of the maximum amplitude.

5.4.2   Rising Edge Linear Fit

With this algorithm the event timestamp is determined as the intersection point between the baseline and the rising edge linear fits. Fig. 5.13 show the algorithm implementation on an example signal. By fitting the baseline as well with a straight line with no fixed orientation (as with the CFD algorithm, where the baseline is assumed horizontal) it is possible to take into account the possibility that the SiPM signal is not completely decayed yet due to an earlier event in proximity. For optimal time resolution results, the fitting intervals for baseline and rising edge must be determined, however. In the next paragraph the optimization of this algorithm will be investigated.

This method is more complex to be implemented on an FPGA with respect to the CFD,

but as the expected event rate is not too large, we are able to record the whole waveform, and this algorithm can be easily implemented offline.
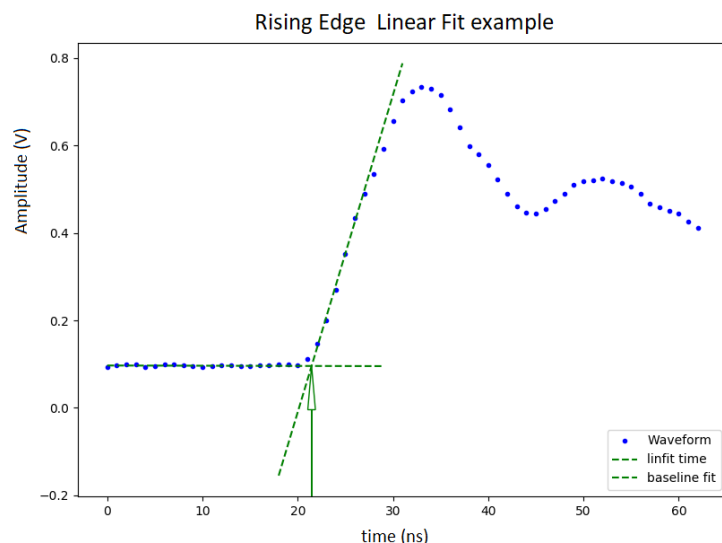

Figure 5.13: Rising Edge Linear Fit on example event. The fitted baseline and rising edge are represented by the green dashed lines. Their interception point, shown by an arrow, points the signal timestamp.

5.4.3 Derivative method

With this method the leading edge time is calculated as the intercept point of the highest derivative point. The signal waveform is differentiated using a smooth noise-robust numerical method [39]. Fig. 5.14 shows this algorithm implementation: the computed derivative is represented by the dashed line on the lower side of the graph, its highest value highlighted with the arrow pointing to its corresponding point on the waveform. In that point the intercept equation is computed and the event arrival time is taken as the intercept intersection point with the baseline. An FPGA implementation of this method exists and is described in [40].
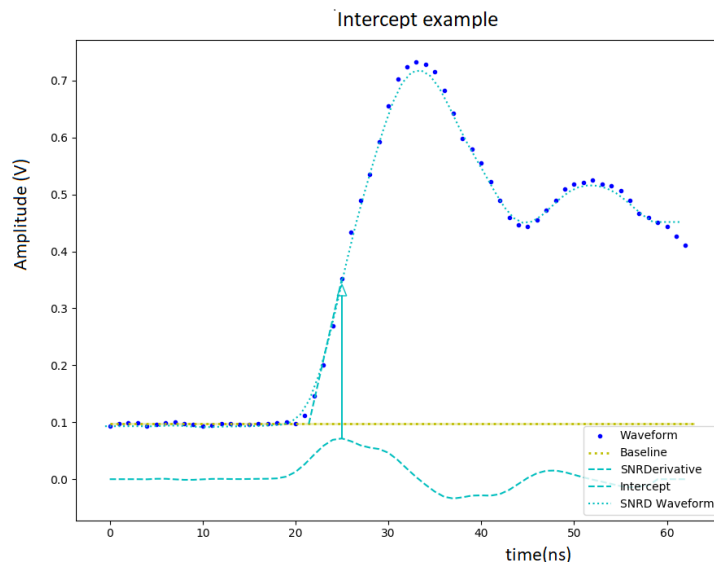
Figure 5.14: Intercept algorithm on example event. The numerically computed derivative is drawn in light blue below the signal. The event timestamp is taken as the intersection point between the baseline and the intercept computed in the point corresponding to the highest derivative value.

5.4.4   Algorithm optimization

Each of the algorithms parameters must be accurately determined in order to maximize the tile timing resolution. In this section the optimization procedure for the CFD and Linear Fit methods are described.

CFD

The time resolution is computed for fraction of leading edge amplitude from 1 to 90%, both for the tile single channels and the analog sum of all of them. Fig. 5.15 shows the time resolution with respect to the fraction assumed for CFD, with the beam passing in the central point of the tile. All beam positions taken on the tiles exhibit a similar behaviour. It is clearly visible that for both Tile F and Tile G the time resolution reach a minimum at a fraction of about 6-8%. This is reasonable as the most reliable information on the particle arrival time is provided by the first photons to reach the SiPM, the ones that travel directly from their originating point to the SiPM windows, with no deviations

or reflections.

Moreover, it is noted that the sum of the signals registered on single channel improves drastically the time resolution of the tile.
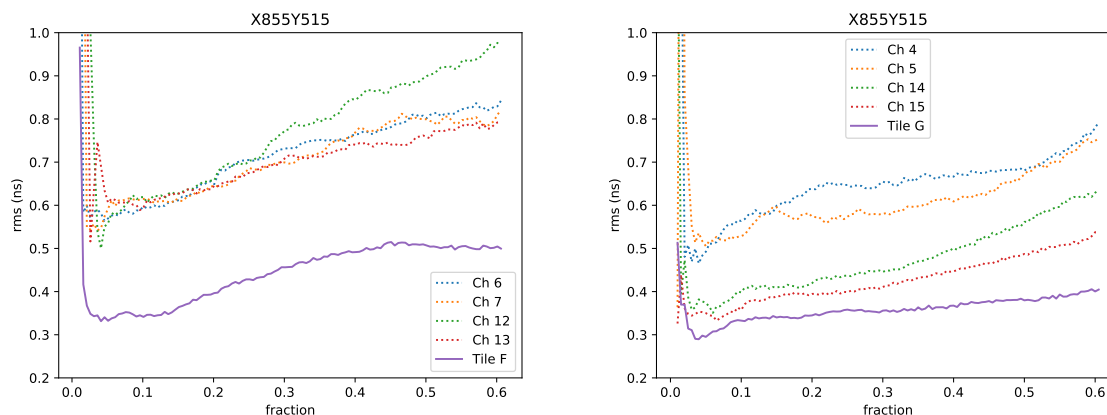

Figure 5.15: Time resolution calculated for particle crossing the central point of the tile, with respect to the fraction used to determine arrival time. On the left, Tile F results, on the right Tile G.

Rising edge linear fit

The starting point is chosen as the 5% of the total amplitude of the rising edge, and the tile timing resolution is computed over an interval going from the 5 to the 95% of the peak amplitude. The baseline is fitted from the beginning of recorded data to 70% of time position of the starting point. However, this is not practical in the real experiment and a different method to evaluate the baseline would have to be developed.

Fig. 5.16 shows the computed time resolution for Tile F and G with respect to the fraction of rising edge taken as major extreme the fit was made on, with the beam passing in the central point of the tile. This method is noticeably more stable over variation of rising edge fit interval, as the time resolution is almost constant over the interval, except for fractions over the 80%. As a reference, an ideal fitting interval is assumed between 5 and 50% of the rising edge. However, with this method the computed tile timing resolution is consistently worse than the one obtained using CFD.
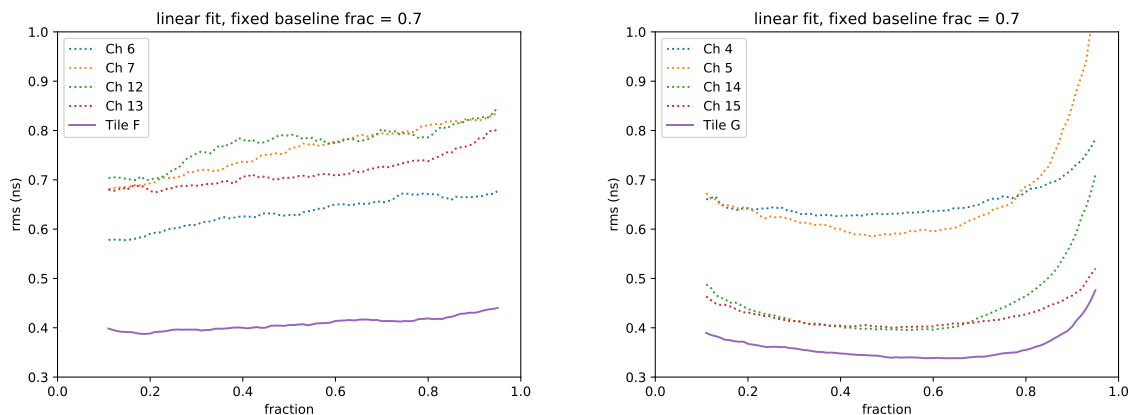
Figure 5.16: Time resolution calculated for particle crossing central point of the tile, with respect to the rising edge fit interval upper limit fraction. On the left, Tile F results, on the right Tile G.

5.4.5   Best timing algorithm

The tiles timing resolution computed with the optimized algorithms are reported in Tab. 5.5, without subtracting the trigger jitter. Results refer to the beam passing through three distinctive points: the tile center, a tile corner and near the middle of the square edge. It is noted that the Intercept algorithm performs consistently worse than the two other methods, its better performance for closely spaced double hit discrimination is not as relevant for this application. The best results for each tile and point are highlighted in grey, except for two cases, the Constant Fraction Discriminator, with threshold set at 6% of the peak amplitude, generates the smallest time resolution. Therefore, for the estimation of the prototypes time resolution performed in the next chapter, the CFD algorithm will be used. The linear fit method continues to be employed as it has already been used by collaborators within SHiP to report results on other prototypes.

Algorithm	Time resolution (ps)					
	center		*corner*		*side*	
	Tile F	Tile G	Tile F	Tile G	Tile F	Tile G
CFD - threshold at 6%	370	346	958	353	480	380
Linear Fit from 5 to 50%	412	336	748	362	598	392
Derivative Method	377	348	1040	497	632	418

Table 5.5: Tiles time resolution with different optimized algorithms. Beam on tile center, edge and corner.

5.5 Trigger Optimization and timing resolution

We optimized the CFD algorithm fraction for the trigger as well. In this case, the rms is computed for the time difference between the trigger plane placed before the tiles and the one placed behind with respect to the beam direction. As we can see in Fig. 5.17, the ideal fraction is slightly higher for the trigger than for the tiles, at a 10% value, producing an rms of 315 ps. This is to be expected, as the trigger signal is produced by a single small SiPM, and for amplitude fractions smaller than 10% the signal is still subjected to baseline fluctuations due to noise.

If we consider the contribution for each trigger to be equal, the time resolution for one trigger plane is:

$$\sigma_{1tr} = \frac{\sigma}{\sqrt{2}} \tag{5.1}$$

When measuring the tile timing resolution, the trigger timestamp is determined as the mean of the two trigger planes, therefore, the trigger time resolution is determined with eq. 5.2, and its value reported in Tab. 6.1.

$$\sigma_{trigger} = \frac{\sqrt{\sigma_{1tr}^2 + \sigma_{1tr}^2}}{2} = \frac{\sigma}{2} \tag{5.2}$$
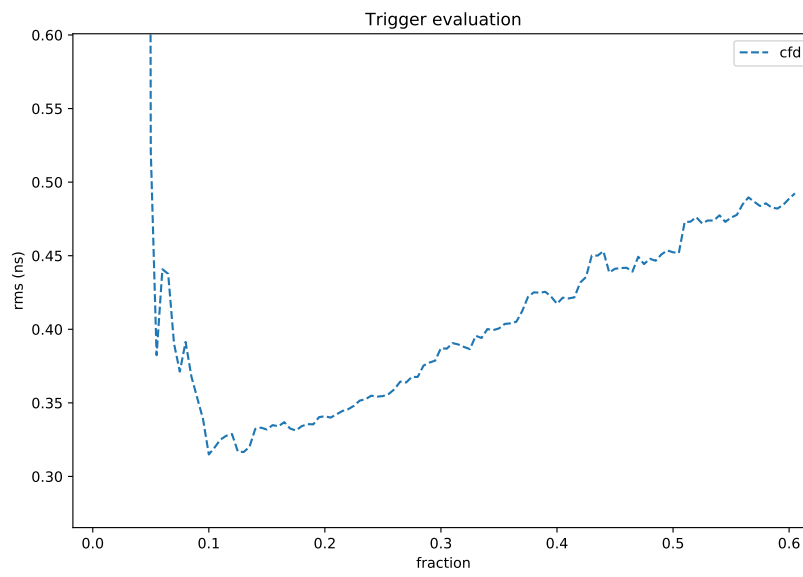
Figure 5.17: Trigger time resolution with respect to the CFD threshold fraction used to extract the events timestamp.

Chapter 6

Experimental measurements and comparison with simulation

6.1   Tiles Timing Resolution

In this section the time data analysis performed for the 15×15 cm^2 tiles and the test beam trigger is reported. Before computing the final tile timing resolution, we verified whether any correlations between the signal peak amplitude and the extracted time existed, in order to apply any necessary correction to this effect.

6.1.1   CERN T10 test beam tiles

Signal amplitude - time correlation

We checked for potential correlations between signal amplitude and the extracted event timestamp. The CFD algorithm is designed to minimize and correct this kind of correlation, but we cannot exclude a priori that there may be some effects not accounted for. In Fig. 6.1 the amplitude-time pairs are reported, and Pearson's linear r coefficient is computed. For both tiles the r coefficient value is < 0.1 and we can assume that no significant correlation is present.
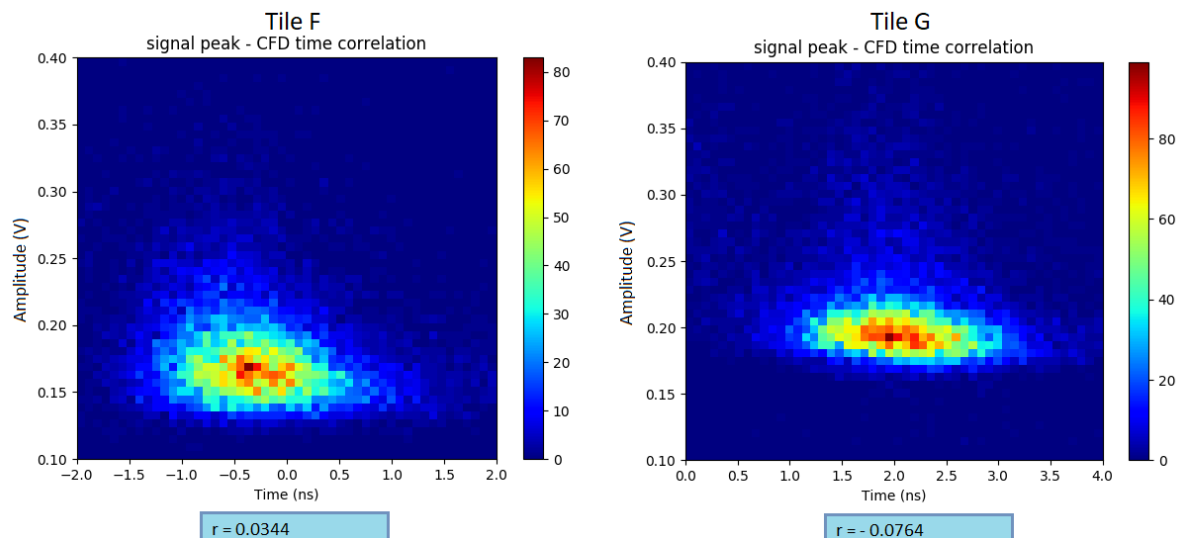
Figure 6.1: Extracted time vs signal peak amplitude for Tile F, on the left, and Tile G, on the right. Pearson r coefficient is reported as well.

Results

Tile F and Tile G time resolution is reported in Tab. 6.1 with the CFD algorithm. The threshold is set at 6% on the amplitude of the tile signal, and at 10% of the trigger signal. Both tiles, after the subtraction of the trigger jitter, do not reach the target time resolution performance of 400 ps, Tile F exceeding it with about 40 ps, and Tile F with 70 ps. In order to obtain a time resolutions comparable with the rectangular tile prototype further adjustments to the tile design are needed.

	σ_t (ps)	$\sigma_t \ominus \sigma_{trigger}$ (ps)
Trigger	158	/
Tile F	466	438
Tile G	495	469

Table 6.1: Tile F and Tile G time resolution.

6.1.2 DESY test beam tile

Tile H, which is equipped with four 4×4 mm^2 S14160 SiPM and covered in white paint, was sent to DESY for testing. Unfortunately during transport to the test beam facility one of the SiPM glued to Tile H was damaged and it was not possible to replace it. Therefore, data reported in this section is to be regarded with a missing output channel. This inevitably causes a worsening of the tile timing resolution, yet the performance turned out to be an improvement compared to the previous tiles and the detection efficiency surpassed 99.7%. Two data acquisition runs were performed, one with the SiPMs bias set at 42 V, and one at 42,5 V.

CFD optimization check

We repeated the optimization process for the CFD algorithms to ascertain that the CFD fraction was suitable. For an easier reading, we report the time resolution of the tile with the beam passing through a few characteristic points: on the tile corner in front of a SiPM, in the tile center, in the middle of the tile side and an inner point about halfway between the SiPM and the tile center. The exact points positions are drawn in green in Fig. 5.10. The point in front of the SiPM is critical as a large number of photons reach the SiPM and the amplifier transistor saturates due to the large SiPM output current. As we can see in Fig. 6.2, the tile timing resolution worsen dramatically for this point (marked with the blue line in the graph) when the CFD fraction is set between 30 and 40 % of the peak amplitude. The point on the scintillator side instead would consistently be the one with the computed worse time resolution, as it is the farthest point from all SiPMs. For all points the output of the SiPMs was summed.
The CFD algorithm provides the best time resolution with a threshold set around 6% of the signal amplitude, similar to the other tiles. This is sufficiently low that the effects of the amplifier saturation are not relevant.
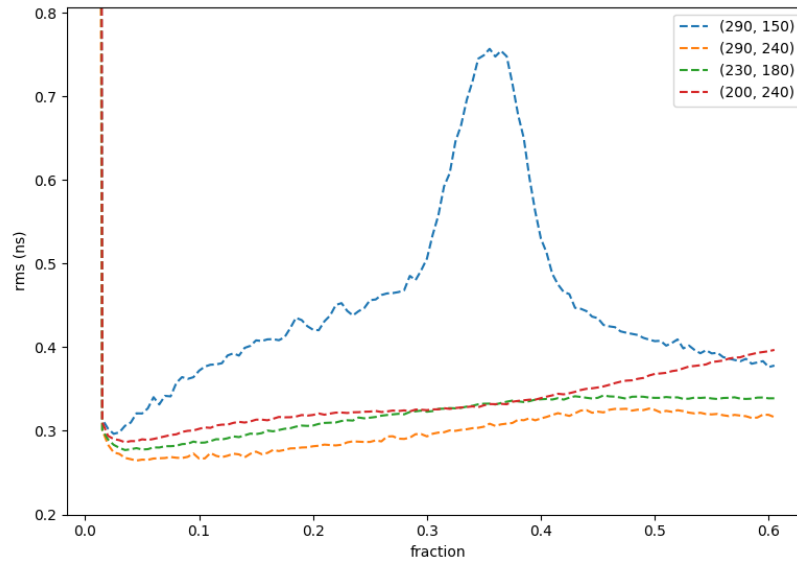
Figure 6.2: Time resolution with respect to the peak amplitude fraction used to determine the event timestamp, with the beam passing in four different points. The blue line marks the run taken with the beam passing in front of a SiPM, and we can see the effects of the amplifier saturation.

Signal amplitude - Time correlation

Again we verify if a correlation between the signal amplitude and the extracted timestamp exists. Fig. 6.3 shows the amplitude distribution with respect to time extracted for the two runs at different high voltage. Similarly to Tiles F and G, we can affirm that no linear correlation exists between the two distributions, as expected.
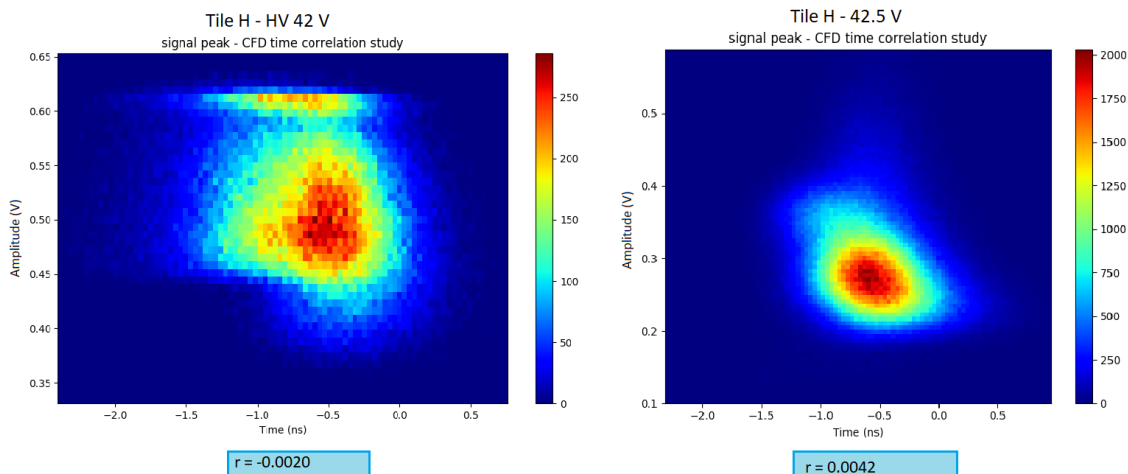
Figure 6.3: Extracted time vs signal peak amplitude for Tile H, with HV = 42 V on the
left, and HV = 42.5 on the right. Pearson r coefficient is reported as well.

Time resolution

Figure 6.4 shows the delay between the trigger signal and the time extracted with the
CFD algorithm, with a treshold at 6%, for the beam positions shown in Fig. 5.10.

Tile H time resolution results are reported here, with the CFD method with a thresh-
old at 6% in two cases:

1. considering the data taken with the beam passing through all points;

2. excluding points in the sector near the non-functional SiPM - in Fig. 5.10 these
   points are marked in purple.

Results are reported in Tab. 6.2 for both runs. It is noted that the time resolutions is
clearly better for the run with HV 42.5, at 42 V the SiPM bias voltage is not sufficient.
Nevertheless, at the higher bias voltage, Tile H reaches the set goal of a time resolution
less than 400 ps even with a non-functioning SiPM.

By removing the points near the non-functional SiPM we obtain an improvement in
the tile resolution. However, this result is still an underestimation of the likely result
with all four functioning SiPMs, as every SiPM, even if placed far from the photons
originating points, still provides a positive contribution to the time resolution of the tile.
This effect can be seen in a simplified situation, where we consider the two functioning
SiPM, here named "Ch 2" and "Ch 3", placed on opposite corners of Tile H. We compute
the tile timing resolution with the beam passing through the points on the tile diagonal,
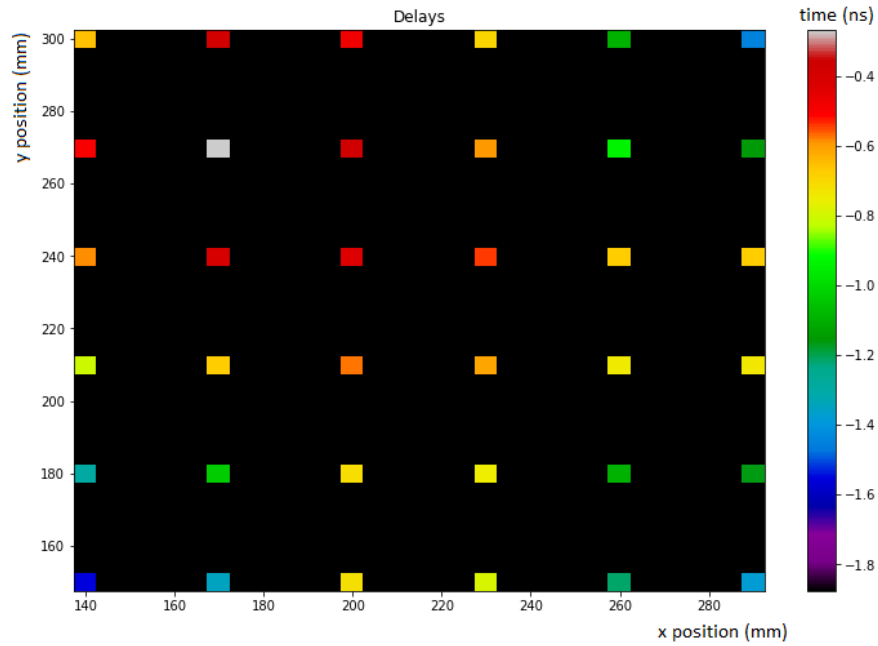
Figure 6.4: Delay between trigger signal and event time extracted with CFD algorithm.

	Bias 42 V	Bias 42.5 V
σ_t *Trigger*	133	124
σ_t *Tile H* *(all points)*	499	399
σ_t *Tile H* *(excluded sector)*	473	368
σ_t *Tile H* $\ominus$ σ_t *trigger* *(all points)*	481	379
σ_t *Tile H* $\ominus$ σ_t *trigger* *(excluded sector)*	454	346

Table 6.2: Time resolution of Tile H. Two runs were taken at different bias voltage, the results reported are computed considering the data acquired with the beam passing through all positions and excluding the points near the broken SiPM.

considering only the output signal of Ch 2 SiPM, and the summed signals of Ch 2 and Ch 3. The resulting time resolution is reported in Fig. 6.5 with respect to the beam distance from Ch 2 SiPM. As we can see, the time resolution largely improves in the

points close to Ch 2 SiPM thanks to the contribution of Ch 3 signal. In the same manner, even excluding the points near the broken SiPM for computing the time resolution, its contribution in farther points would have improved the results nevertheless.
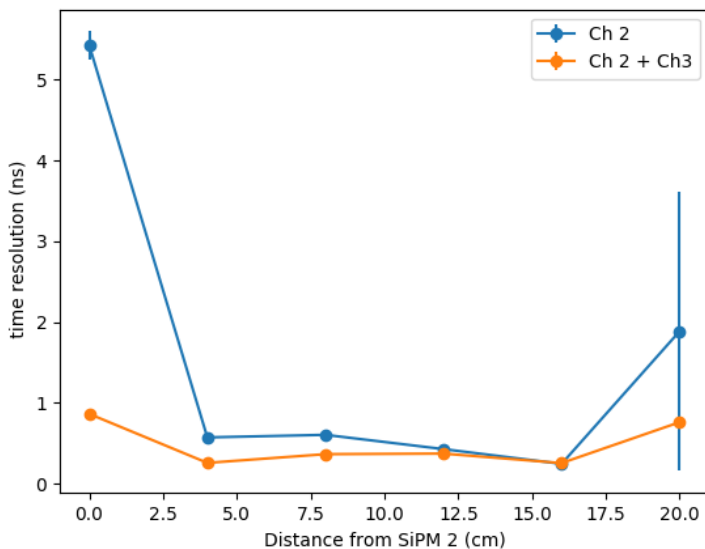

Figure 6.5: tile timing resolution computed by using the output signal of one SiPM (blue line), and the sum of the former and its symmetrical one, as a function of the distance from the first SiPM.

6.2 Tile Simulation

A simulation of the tiles based on the Fluka package [41] was developed in order to provide a useful tool for further studies on the tiles design. In fact, by developing a simulation of the actual tile design that is able to reproduce correctly the experimental results, we can investigate further on the tile geometry, for example studying how the tile resolution varies when the SiPM are placed in different positions, or inserted in a slot inside the scintillator instead of being glued on the corners.

The simulation reproduces all the physics processes involved in our tests. Muons are simulated impinging perpendicularly on the scintillator, either in a narrow beam or uniformly distributed on the tile area. The energy loss of the muon is simulated according to the trajectory of the particle inside the scintillator. Photons are produced isotropically

by the scintillating material. The geometry and physical properties of the detector are reproduced in detail, based on th design of Tile H: the material properties of the scintillator, the external coating and the glue are taken into account as well as their optical behavior. The parameters used in the simulation were taken from technical specifications from producers and dedicated measurements.

Fig. 6.6 shows a detail of the simulated tile configuration in the point in the SiPM mounting point. The scintillator (depicted in red in the figure) is wrapped in aluminized mylar (in gray). A thin (50μm) air layer is present between the mylar foil and the scintillator. The SiPM active surface (face of the black volume) is behind its epoxy window (orange), which is glued to the tile with optical cement (thin cyan line).
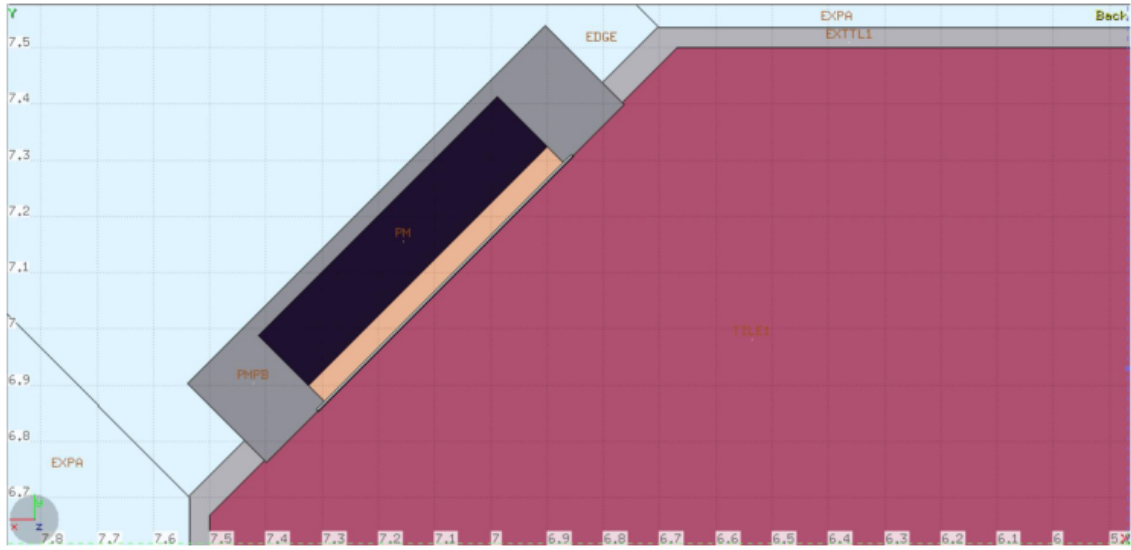

Figure 6.6: Details of the simulated tile corner.

The SiPM output is calculated based on the photons reaching the SiPM window with an empirical response function. For each photoelectron produced an output signal is computed, and summed on all photoelectrons in order to produce the output signal waveform. The function used is:

$$f(t) = \begin{cases} 0, & \text{if } t < 0 \\ A \cdot (t/\tau_{rise}), & \text{if } 0 < t < \tau_{rise} \\ A \cdot e^{(t/\tau_f)}, & \text{if } \tau_{rise} < t < \tau_{rise} + \tau_f \\ A \cdot e^{(t/\tau_s - 1)}, & \text{if } t > \tau_{rise} + \tau_f \end{cases} \tag{6.1}$$

Where A is an amplitude parameter randomly generated following a Gaussian probability density function with $\mu = 5\ mV$ and $\sigma = 2\ mV$. τ_{rise} is the SiPM signal rise time, while τ_f and τ_s are two parameters describing the SiPM signal exponential decay (See Ch. 5.2.1). A small amount of white noise is added as well. Then, the amplifier response is added, both for a quasi-ideal, noiseless amplifier, and for the real amplifier used in the test beam, which suffered from some RF noise pick-up. The latter model includes small amplitude RF modulations, and clipping due to transistor saturation. A finite impulse response filter is then applied to model the amplifier frequency response (-3dB at 1 GHz). Finally, the generated waveform is quantized as it would by the SAMPIC ADC, with the addition of appropriate quantization error.

6.2.1 Simulated timing resolution and comparison with DESY tile

The tile was simulated with muons uniformly distributed on the whole tile area. This simulation reproduces the actual operation conditions of the SHiP experiment. Figure 6.7 shows the simulated delay between the particle hit and the time extracted with the same CFD algorithm used for real data.

Table 6.3 reports the simulated tile timing resolution with and without the addition of electronic noise to the SiPMs signal, compared with the measured time resolution of Tile H.

	σ_t(ps)
Simulated Tile (clean)	163
Simulated Tile (noisy)	207
Tile H (all points)	379

Table 6.3: Simulated tile timing resolution with and without the addition of electronic noise the SiPM signal.

When comparing the simulated tile with prototype H it is clear that the simulation needs to be further tuned, as its reported time resolution is significantly better than the measured one. For example, it has to be noted that the simulation assumes perfect mechanical properties, and the reflectively of the wrapping may be overestimated.
Tile H broken SiPM will be replaced for a new test beam that will be held at the
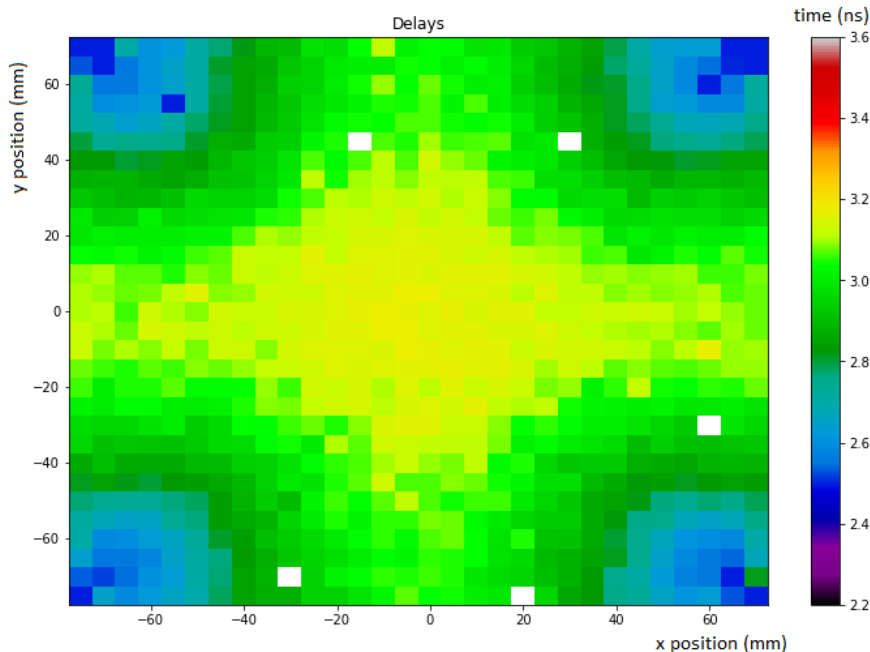
Figure 6.7: Delay between simulated particle hit and time extracted with the CFD algorithm.

Beam Test Facility of Frascati INFN Laboratories, where a new amplification circuit and scintillator type will be tested as well.

6.3 Tile 10×10 cm^2 with slots

Tile C was modified to assemble a new prototype, designed to explore an alternative way for the SiPM placement that was not considered during the previous test beam: to place the SiPM in a thin slot milled in the scintillator bulk, instead of placing it on the external surface. This configuration can be beneficial: the tile assembly is more straightforward, as the SiPM can be positioned and the slot filled with optical cement. In order to glue the SiPM on the scintillator side, instead, a supporting structure must be used to keep the SiPM in place while the glue cures. Moreover, by placing the SiPM in a slot, we are not limited to the scintillator outer edge, but we can evaluate various geometries that potentially can make the tile timing response more uniform.

The first goal is to prove that placing the SiPM in a slot does not worsen the tile timing resolution when the slots are situated in the corner. Tile C scintillator size is $10 \times 10 \times 0.8$

cm^3 and is coated in titanium oxide paint. Two slots have been milled at a 3 mm distance from the tile corner, parallel to the beveled surface, and symmetric with respect to the tile diagonal. The slot is 6 mm deep and with an area of 5×2 mm^2. In order to make a direct performance comparison between the two SiPM mounting options, two 3×3 mm^2 Hamamatsu S13360 were employed: one placed in the slot and one glued on a corner. The SiPM response was evaluated using cosmic muons in the Bologna INFN laboratories.

6.3.1   Experimental Setup

In order to avoid undesirable effects from amplifier saturation, for this test the modified Tile C was connected to an older custom board developed for SiPM readout [42]. This board includes the analog front-end for eight channels and all the acquisition chain, from the digitizer to the data recording on a computer. The front-end and the coupling to the SiPM can be tailored to the specific application. The system allows the control of the biasing voltage and the monitoring of the gain of the SiPM, so that it is possible to compensate temperature variations. Fig. 6.8 shows the Tile connected to the board for testing with cosmic rays. The tile under test was sandwiched between two tiles of similar size used as trigger, also read out by the same board.

Figure 6.8: Tile I connected to the readout and control board.

The front end electronics of this setup differs from the one used for the previous tiles: this board is equipped with a slow shaper that is based on a operational amplifier integrator. Therefore, the output signal of this circuit is the integrated charge produced by the SiPM, and no time information is available. This front end, however, offers superior linearity and amplitude resolution.

6.3.2   Comparison between slot and glued corner

In Fig. 6.9 the integrated charge distribution is reported for both SiPMs. As we can see the response of the SiPM placed into the slot is equal with the one glued to the corner within the uncertainty. The SiPMs can be calibrated from their own dark noise as shown below, to ensure that the number of detected photons is indeed the same in both cases.
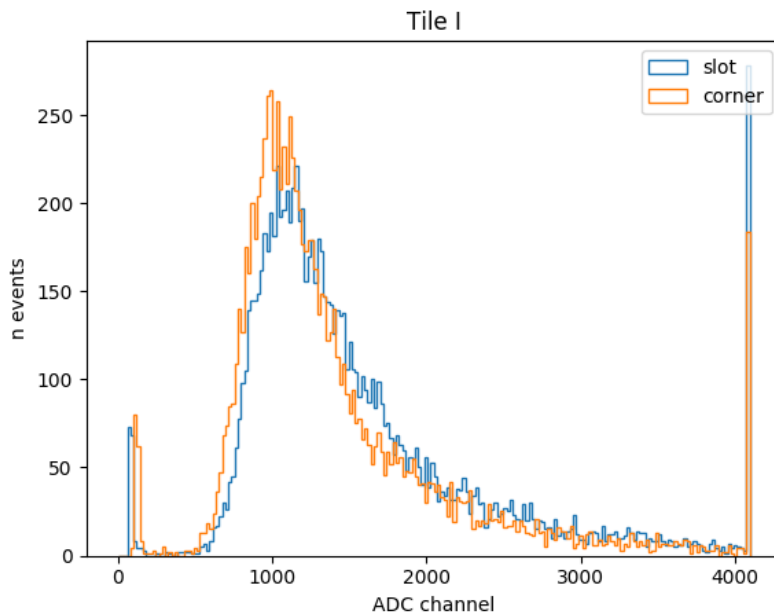

Figure 6.9: Integrated charge distribution of detected cosmic rays.

Light yield

To obtain an estimation of the light yield of the scintillator, we determined the mean number of photons, computed as:

$$n_{ph} = \frac{Q_{cosmics}}{Q_{1pe}} \tag{6.2}$$

where $Q_{cosmics}$ the peak charge measured by the tile during the cosmic rays acquisition and Q_{1pe} is the charge produced when a single SiPM cells fires, obtained from an acquisition run with the SiPM decoupled from the scintillator and light-insulated. The charge spectrum measured with cosmic rays is fitted with a Landau distribution (Fig. 6.10), for both SiPM mounting options. The charge most probable value, baseline subtracted, is reported in Tab. 6.4.
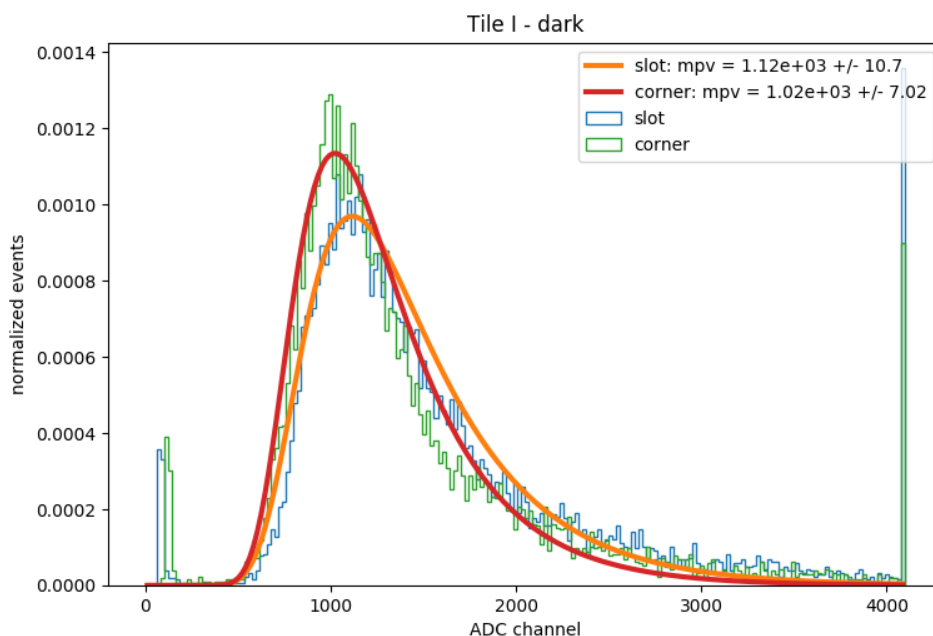

Figure 6.10: Integrated charge distribution fitted with a Landau distribution.

The single cell charge is computed by fitting the dark noise charge spectrum with the sum of two Gaussian distributions, as shown in Fig. 6.11: one representing the baseline and the other the peak corresponding to one cell.

Tab. 6.4 reports the mean number of detected photons according to (6.2). As noted when observing the integrated charge distribution, the performance of the SiPM in the slot is equal to the corner one within errors: both SiPMs are able to detect about 50 photons per particle passing through the scintillator (this includes a $\sim$5% contribution from SiPM crosstalk).
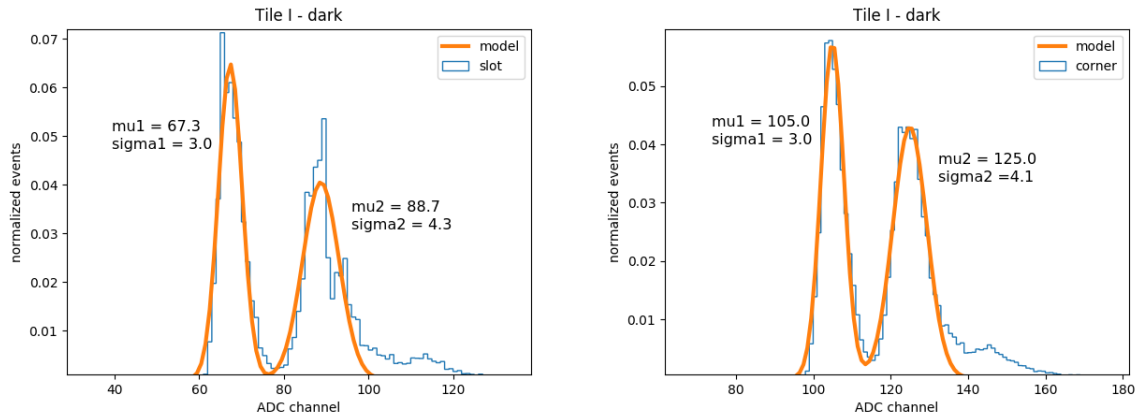
Figure 6.11: Dark integrated charge for the SiPM in the slot (left) and on the corner (right). The charge produced by a single photoelectron is clearly distinguishable from the baseline, represented by the peak on the left side. The distribution is fitted with the sum of two gaussians.

	cosmics charge (a.u.)	1pe charge (a.u.)	number of detected photons
slot	1048.1 ± 11.9	21.4 ± 5.1	49.0 ± 11.7
corner	917.0 ± 8.7	20.0 ± 5.1	45.9 ± 11.7

Table 6.4: Mean number of detected photons.

6.4   New baseline design

With the results obtained in this chapter we defined an improved tile design, to be tested at the Beam Test Facility in Frascati INFN Laboratories in early 2020. This design consists in a $15 \times 15 \times 1$ cm tile, made of Ejen EJ200 scintillator, since we demonstrated that it is possible to reach a time resolution of 400 ps on a tile of such size. The scintillator will be coated in white paint plus an external black paint coating for light tightness, as, while slightly less perfoming, it is easier to employ than alumnized mylar wrapping for a large number tiles.

The SiPMs will have an area of 6×6 mm^2, and will be placed in a slot on the tile corner. Alternative slot placement positions will be evaluated but at the moment the corner is assumed as the baseline design option. The tile will be equipped with an improved readout electronics with less noise and integrated analog sum as well.

If, as we expect, this prototype is able to reach and surpass the target tile resolution, this tile design will probably be used as final design for the detector, except for minor adjustments.

Conclusions

SHiP (Search for Hidden Particles) is a new general purpose fixed target experiment proposed at the CERN SPS accelerator looking for new particles with very weakly couplings and masses in the GeV region in the intensity frontier, thus complementing the energy-frontier physics program of LHC.

The Muon Detector is the most downstream SHiP subdetector, whose aim is to identify muons produced in the decay of hidden particles and to reject background events that mimic signal vertexes. For this purpose, a very high time resolution of the detector is necessary. The Detector technology is based on plastic scintillator tiles directly read out by SiPMs. In order to achieve an overall time resolution of $\sim$ 200 ps of the detector, necessary to efficiently reject background tracks that mimic signal events, the timing resolution of the tile unit must be better than 400 ps. For this reason, the tiles design must be optimized to achieve the best possible resolution, respecting at the same time the budget constrains.

Two possible tile geometries were proposed, a rectangular tile and a square one, with an area of about 200 cm^2. The rectangular tile, read out by six SiPM, was demonstrated to be able to reach the target time resolution in earlier studies, but it is not cost optimized. In this thesis I reported the studies carried out to define the square tile characteristics in order to obtain a comparable result with the rectangular one. I demonstrated that it is indeed possible to obtain a target time resolution on a square tile of such size with a four SiPM readout, thanks to the corner placement which improves uniformity. I identified the best suited for this application is a coating of titanium oxide paint, as it is sufficiently performing and of easy employment for large production scales. Moreover, I tested various ways of mounting the SiPM to the scintillator, and I concluded that while both glueing the SiPM to the scintillator corner and placing it in a slot milled in the scintillator bulk produce equivalent results in terms of light collection, the second option is preferable as it is mechanically easier to build. An improved prototype with the characteristics defined with this thesis studies, candidate to being the new reference design, will be tested in the near future at the Frascati INFN Laboratories.

Finally, an investigation of possible algorithm to extract timing information from the tile

output was carried out. I found that the most effective algorithm is the constant fraction discriminator, since it gives the smallest spread in the arrival time distributions. The constant fraction discriminator algorithm will be used preferentially in further studies.

I plan to further improve the results obtained in this studies, by using SiPM with a larger area and improved photon detection efficiency. I will also explore alternative algorithms that make use of the full output waveform information in order to reach a timing resolution better than 300 ps. This would allow the Muon Detector to provide a complementary measurement to the dedicated Timing Detector.

Bibliography

[1]   M. Fukugita and T. Yanagida. "Baryogenesis Without Grand Unification". In: *Phys. Lett.* B174 (1986), pp. 45–47. DOI: 10.1016/0370-2693(86)91126-3.

[2]   SHiP Collaboration. "A facility to search for hidden particles at the CERN SPS: the SHiP physics case". In: *Reports on Progress in Physics* 79.12, 124201 (Dec. 2016), p. 124201. DOI: 10.1088/0034-4885/79/12/124201. arXiv: 1504.04855 [hep-ph].

[3]   M. Passera, W. J. Marciano, and A. Sirlin. "The muon g-2 and the bounds on the Higgs boson mass". In: 78.1, 013009 (July 2008), p. 013009. DOI: 10.1103/PhysRevD.78.013009. arXiv: 0804.1142 [hep-ph].

[4]   Gopolang Mohlabeng. "Revisiting the dark photon explanation of the muon anomalous magnetic moment". In: *Physical Review D* 99.11 (June 2019). ISSN: 2470-0029. DOI: 10.1103/physrevd.99.115001. URL: http://dx.doi.org/10.1103/PhysRevD.99.115001.

[5]   Pasquale D. Serpico. "Astrophysical models for the origin of the positron "excess"". In: *Astroparticle Physics* 39 (Dec. 2012), pp. 2–11. DOI: 10.1016/j.astropartphys.2011.08.007. arXiv: 1108.4827 [astro-ph.HE].

[6]   Mauro Raggi and Venelin Kozhuharov. "Results and perspectives in dark photon physics". In: *Riv. Nuovo Cim.* 38.10 (2015), pp. 449–505. DOI: 10.1393/ncr/i2015-10117-9.

[7]   A. Buonaura. "Study of nu-tau properties with the SHiP experiment". Presented 2017. URL: https://cds.cern.ch/record/2268663.

[8]   T. Asaka, S. Blanchet, and M. Shaposhnikov. "The νMSM, dark matter and neutrino masses [rapid communication]". In: *Physics Letters B* 631.4 (Dec. 2005), pp. 151–156. DOI: 10.1016/j.physletb.2005.09.070. arXiv: hep-ph/0503065 [astro-ph].

[9] T. Asaka and M. Shaposhnikov. "The νMSM, dark matter and baryon asymmetry of the universe [rapid communication]". In: *Physics Letters B* 620.1-2 (July 2005), pp. 17–26. DOI: 10.1016/j.physletb.2005.06.020. arXiv: hep-ph/0505013 [hep-ph].

[10] Nir Polonsky. "Supersymmetry Structure and Phenomena". In: *arXiv e-prints*, hep-ph/0108236 (Aug. 2001), hep–ph/0108236. arXiv: hep-ph/0108236 [hep-ph].

[11] SHiP Collaboration. "A facility to Search for Hidden Particles (SHiP) at the CERN SPS". In: *arXiv e-prints*, arXiv:1504.04956 (Apr. 2015), arXiv:1504.04956. arXiv: 1504.04956 [physics.ins-det].

[12] SHiP Collaboration. *SHiP Experiment - Progress Report*. Tech. rep. CERN-SPSC-2019-010. SPSC-SR-248. Geneva: CERN, Jan. 2019. URL: https://cds.cern.ch/record/2654870.

[13] K. Kershaw et al. "Design Development for the Beam Dump Facility Target Complex at CERN". In: *Journal of Instrumentation* 13.10 (Oct. 2018), P10011. DOI: 10.1088/1748-0221/13/10/P10011. arXiv: 1806.05920 [physics.ins-det].

[14] SHiP Collaboration. *Addendum to Technical Proposal: A Facility to Search for Hidden Particles (SHiP) at the CERN SPS*. Tech. rep. CERN-SPSC-2015-040. SPSC-P-350-ADD-2. Geneva: CERN, Oct. 2015. URL: https://cds.cern.ch/record/2060742.

[15] W. M. Bonivento. "Studies for the electro-magnetic calorimeter SplitCal for the SHiP experiment at CERN with shower direction reconstruction capability". In: *Journal of Instrumentation* 13.02 (Feb. 2018), pp. C02041–C02041. DOI: 10.1088/1748-0221/13/02/c02041. URL: https://doi.org/10.1088%5C%2F1748-0221%5C%2F13%5C%2F02%5C%2Fc02041.

[16] N. Tosi. "The downstream Muon detector of the SHiP experiment". In: *Nuclear Instruments and Methods in Physics Research Section A: Accelerators, Spectrometers, Detectors and Associated Equipment* 936 (2019), pp. 263–265. DOI: https://doi.org/10.1016/j.nima.2018.09.105.

[17] W. Baldini et al. "Measurement of parameters of scintillating bars with wavelength-shifting fibres and silicon photomultiplier readout for the SHiP Muon Detector". In: *Journal of Instrumentation* 12.3 (Mar. 2017), P03005. DOI: 10.1088/1748-0221/12/03/P03005. arXiv: 1612.01125 [physics.ins-det].

[18] S. Gòmez et al. "MUSIC: An 8 channel readout ASIC for SiPM arrays". In: Apr. 2016, 98990G. DOI: 10.1117/12.2231095.

[19] E. Delagnes et al. "The SAMPIC Waveform and Time to Digital Converter". In: *2014 IEEE Nuclear Science Symposium and Medical Imaging Conference (2014 NSS/MIC), and 21st Symposium on Room-Temperature Semiconductor X-Ray and Gamma-Ray Detectors*. Sce Electronique. Seattle, United States, Nov. 2014. URL: `http://hal.in2p3.fr/in2p3-01082061`.

[20] W.R. Leo. *Techniques for Nuclear and Particle Physics: a how-to approach, 2nd revised edition*. Berlin, Germany: Springer-Verlag, 1994.

[21] D. S. McGregor. "Materials for Gamma-Ray Spectrometers: Inorganic Scintillators". In: *Annual Review of Materials Research* 48 (2018), pp. 245–277. DOI: `https://doi.org/10.1146/annurev-matsci-070616-124247`.

[22] S. N. Ahmed. *Physics and engineering of radiation detection*. San Diego, CA, USA: Academic Press, 2007.

[23] L. Lakowicz. *Principle of Fluorescence Spectroscopy*. Berlin, Germany: Springer-Verlag, 2006.

[24] G.F. Knoll. *Radiation detection and measurement, 4th edition*. New York, NY, USA: John Wiley & Sons Inc, 2010.

[25] M. Grodzicka-Kobyla et al. "Silicon photomultipliers in gamma spectroscopy with scintillators". In: *Nuclear Inst. and Methods in Physics Research, A* 926 (2019), pp. 129–147. DOI: `https://doi.org/10.1016/j.nima.2018.10.065`.

[26] Fondazione Bruno Kessler. "Optimization of SiPM technology". In: (2013). URL: `https://srs.fbk.eu/optimization-sipm-technology`.

[27] SenseL. *An introduction to the Silicon Photomultiplier - Technical Note*. 2017. URL: `https://www.sensl.com/downloads/ds/TN%5C%20-%5C%20Intro%5C%20to%5C%20SPM%5C%20Tech.pdf`.

[28] C. Piemonte and A. Gola. "Overview on the main parameters and technology of modern Silicon Photomultipliers". In: *Nuclear Inst. and Methods in Physics Research, A* 926 (2019), pp. 2–15. DOI: `https://doi.org/10.1016/j.nima.2018.11.119`.

[29] SenseL. *C-Series Low Noise, Blue-Sensitive Silicon Photomultipliers Datasheet*. 2018. URL: `https://sensl.com/downloads/ds/DS-MicroCseries.pdf`.

[30] Hamamatsu. *MPPC S13360 Series Datasheet*. 2019. URL: `https://www.hamamatsu.com/resources/pdf/ssd/s13360_series_kapd1052e.pdf`.

[31] S. Sze. *Physics of Semiconductor Devices, 2nd ed.* New York, USA: Wiley, 1981.

[32] P. Eckert et al. "Characterisation Studies of Silicon Photomultipliers". In: (2010). DOI: `arXiv:1003.6071v2[physics.ins-det]`.

[33] S. Seifert et al. "A high bandwidth preamplifier for SiPM-based TOF PET scintillation detectors". In: Nov. 2008, pp. 1616–1619. DOI: `10.1109/NSSMIC.2008.4775107`.

[34] F. Corsi et al. "Modelling a silicon photomultiplier (SiPM) as a signal source for optimum front-end design". In: *Nuclear Instruments and Methods in Physics Research Section A: Accelerators, Spectrometers, Detectors and Associated Equipment* 572 (Mar. 2007), pp. 416–418. DOI: `10.1016/j.nima.2006.10.219`.

[35] Eljen Technology. *GENERAL PURPOSE EJ-200, EJ-204, EJ-208, EJ-212*. 2016. URL: `https://eljentechnology.com/products/plastic-scintillators/ej-200-ej-204-ej-208-ej-212`.

[36] Hamamatsu. *MPPC S14160/S141601 Series Datasheet*. 2019. URL: `https://www.hamamatsu.com/resources/pdf/ssd/s14160_s14161_series_kapd1064e.pdf/`.

[37] S. Scheu, H. Kaspar, and P. Robmann. "Studies on wrapping materials and light collection geometries in plastic scintillators". In: *Nuclear Instruments and Methods in Physics Research Section A: Accelerators, Spectrometers, Detectors and Associated Equipment* 567.1 (2006). Proceedings of the 4th International Conference on New Developments in Photodetection, pp. 345–349. ISSN: 0168-9002. DOI: `https://doi.org/10.1016/j.nima.2006.05.153`. URL: `http://www.sciencedirect.com/science/article/pii/S0168900206009879`.

[38] A. Taheri and R. G. Peyvandi. "The impact of wrapping method and reflector type on the performance of rod plastic scintillators". In: *Measurement* 97 (2017), pp. 100–110. ISSN: 0263-2241. DOI: `https://doi.org/10.1016/j.measurement.2016.10.051`. URL: `http://www.sciencedirect.com/science/article/pii/S0263224116306121`.

[39] P. Holoborodko. *Smooth noise-robust differentiators*. 2013. URL: `http://www.holoborodko.com/pavel/numerical-methods/numerical-derivative/smooth-low-noise-differentiators/`.

[40] N. Tosi. "Upgraded back-end electronics for the CMS Fast Beam Conditions Monitor". In: *Nuclear Instruments and Methods in Physics Research Section A: Accelerators, Spectrometers, Detectors and Associated Equipment* 936 (2019). Frontier Detectors for Frontier Physics: 14th Pisa Meeting on Advanced Detectors, pp. 396–398. ISSN: 0168-9002. DOI: `https://doi.org/10.1016/j.nima.2018.08.106`. URL: `http://www.sciencedirect.com/science/article/pii/S0168900218310647`.

[41] G. Battistoni et al. "The FLUKA code: description and benchmarking". In: *AIP Conference Proceedings* 896.1 (2007), pp. 31–49. DOI: 10.1063/1.2720455. eprint: https://aip.scitation.org/doi/pdf/10.1063/1.2720455. URL: https://aip.scitation.org/doi/abs/10.1063/1.2720455.

[42] G. Balbi et al. "A versatile readout and control system for Silicon photomultipliers". In: *2011 IEEE Nuclear Science Symposium Conference Record*. Oct. 2011, pp. 918–923. DOI: 10.1109/NSSMIC.2011.6154571.

Acknowledgements